

Aerodynamic Performance Study on a Ducted Propeller System for Propulsion and Control & Stability Applications

Vikesh N. Harinarain

Technische Universiteit Delft



AERODYNAMIC PERFORMANCE STUDY ON A DUCTED PROPELLER SYSTEM FOR PROPULSION AND CONTROL & STABILITY APPLICATIONS

by

Vikesh N. Harinarain

in partial fulfillment of the requirements for the degree of

Master of Science
in Aerospace Engineering

at the Delft University of Technology,
to be defended publicly on Tuesday May 9, 2017 at 1:00 PM.

Student number: 4052544

Thesis registration nr: 125#17#MT#FPP

Supervisor:

Thesis committee:

dr. ir. R. Vos

Prof. dr. ir L. L. M. Veldhuis

dr. ir. R. Vos

dr. ir. W. A. Timmer

ir. N. van Arnhem

TU Delft

TU Delft

TU Delft

TU Delft

TU Delft

An electronic version of this thesis is available at <http://repository.tudelft.nl/>.

PREFACE

This thesis contains the research that I have done as a last step in obtaining my Master's degree in Aerospace Engineering at the Delft University of Technology. Therefore it concludes years of studying, which will be followed by a new phase of life.

Being the largest project I have worked on thus far, the work has definitely been challenging and an opportunity to develop several skills in engineering, research and life in general. Having been through several ups and downs, both in and outside of my research, looking back at it, I can finally say that I have enjoyed the ride and I am grateful for the learning experiences.

First and foremost, I would like to thank my parents and little sister for their great and unconditional support during all of my years of studying. Secondly, I would like to thank all of my fellow student friends who have motivated and supported me during all years of studying. Also, I would also like to thank prof. Leo Veldhuis and Roelof Vos for giving me the opportunity to work on this topic and provide me with guidance throughout the work. Furthermore, I would like to thank Nick van den Dungen for our cooperation in ducted propeller implementation in aircraft. Last but certainly not least, a special thanks goes out to my other supervisor, Nando van Arnhem, who guided me a lot with my work, providing new ideas and insights, at times when I was lost and confused.

*Vikesh N. Harinarain
Delft, May 2013*

ABSTRACT

The Delft University Unconventional Concept (DUUC) is an innovative short take-off medium range aircraft design that utilizes a system of two ducted propellers, mounted on the aft part of the fuselage. The first design of this system consists of two axisymmetric ducts, each containing a propeller mounted to a centerbody that is attached to the duct by a strut. Furthermore each ducted propeller contains two horizontal and two vertical control surfaces and the ducted propellers are mounted to the fuselage by two external struts. Besides the function of propulsion, the ducted propeller system also replaces the horizontal and vertical tail for control and stability. The aerodynamic characteristics of this system are investigated by the construction of an aerodynamic performance model, consisting of a combination of low order analytical and numerical methods. This model aims on predicting the aerodynamic coefficients, which are significant for control and stability over a range of operational conditions, incidence angles and thrust settings. These include lift, side force, drag and control surface effectiveness. The numerical part of the model is first validated against existing experimental data from literature, after which the complete model is held against data from a low speed wind tunnel test on a small scale model of the system. Finally, a sensitivity analysis aims on finding the effect of the most important design parameters on the thrust to power ratio of both the propeller and the total system. The numerical model is successfully validated in its capability of predicting trends in propeller and total system thrust over a range of operational conditions. The analytical model is capable of predicting the lift and side force performance of the system to a reasonable degree in the unstalled regime. Drag is significantly underestimated by the analytical model, possibly due to unknown flow separation and interference effects, which require higher order methods. Stall angle and maximum lift can not be modeled accurately by the low order performance model. Finally, the sensitivity analysis shows that advance ratio is the most critical operational condition whereas duct shape and duct aspect ratio are most affecting the total system thrust to power ratio.

CONTENTS

Abstract	v
Nomenclature	ix
List of Figures	xi
List of Tables	xvii
1 Introduction	1
1.1 Research objective and research questions	2
2 Modeling	5
2.1 System build up	5
2.1.1 Component velocities	8
2.1.2 Component inflow angles	10
2.2 Lift and drag	11
2.2.1 Duct	12
2.2.2 Centerbody	15
2.2.3 Propeller	16
2.2.4 Internal strut	19
2.2.5 External strut	21
2.2.6 Control surfaces	23
2.2.7 Interference drag	25
2.3 Side force model	26
2.4 Net thrust	27
2.5 Control and stability coefficients	27
2.6 Numerical model	27
2.7 Analysis method	28
3 Validation	29
3.1 Numerical model validation	29
3.1.1 Operating conditions and geometry	29
3.1.2 Results and comparison	32
3.1.3 Error analysis	32
3.2 Analytical model validation	35
3.2.1 Experimental set up and test conditions DUUC wind tunnel test	35
3.2.2 Results and comparison	40
4 Design studies	59
4.1 Definition of variables and methodology	59
4.1.1 Reynolds number	59
4.1.2 Advance ratio	60
4.1.3 Tip clearance	60
4.1.4 Propeller longitudinal position	60
4.1.5 Aspect ratio	61
4.1.6 Camber	61
4.1.7 Thickness to chord ratio	61

4.2	Sensitivity analysis	62
4.2.1	Reynolds number	62
4.2.2	Advance ratio	64
4.2.3	Tip clearance.	66
4.2.4	Propeller longitudinal position.	68
4.2.5	Aspect ratio	70
4.2.6	Camber	72
4.2.7	Thickness to chord ratio	74
5	Conclusion & Recommendations	77
5.1	Conclusion	77
5.2	Recommendations	78
A	Appendix A	79
B	Appendix B	83
B.1	Reynolds number	83
B.2	Advance ratio	85
B.3	Tip clearance	88
B.4	Propeller longitudinal position	90
B.4.1	Aspect ratio	94
B.5	Camber	96
B.6	Thickness to chord ratio	98
	Bibliography	101

NOMENCLATURE

Variables

α	=	angle of attack [rad]
β	=	sideslip angle [rad]
c	=	chord length [m]
b	=	span [m]
D	=	diameter [m]
l	=	length [m]
A	=	cross-sectional area [m ²]
S	=	planform area [m ²]
S_{duct}	=	$D_{\text{duct}} \cdot c_{\text{duct}}$ [m ²]
S_{prop}	=	$(\pi/4) D_{\text{prop}}^2$ [m ²]
AR_{duct}	=	$D_{\text{duct}}/c_{\text{duct}}$ [-]
T	=	thrust [N]
L	=	lift [N]
D	=	drag [N]
F_Y	=	side force [N]
F_x	=	axial force [N]
C_L	=	$L/(1/2 \rho V_{\infty}^2 S_{\text{duct}})$ [-]
C_Y	=	$F_Y/(1/2 \rho V_{\infty}^2 S_{\text{duct}})$ [-]
C_D	=	$D/(1/2 \rho V_{\infty}^2 S_{\text{duct}})$ [-]
T_c	=	$T/(1/2 \rho V_{\infty}^2 S_{\text{duct}})$ [-]
T'_c	=	$T/(1/2 \rho V_{\infty}^2 S_{\text{prop}})$ [-]
n	=	revolutions per second [1/s]
c_T	=	$T/(\rho n^2 D_{\text{prop}}^4)$ [-]
c_P	=	$P/(\rho n^3 D_{\text{prop}}^5)$ [-]
J	=	$V/(n D_{\text{prop}})$ [-]
η	=	$c_T/c_P J$ [-]

Subscripts

duct	=	duct
cb	=	centerbody
prop	=	propeller
propcb	=	combined propeller and centerbody
intstrut	=	internal strut
extstrut	=	external strut
vane	=	control vanes
e	=	elevator
r	=	rudder
interf	=	interference
interf	=	total

Acronyms

DUUC	=	Delft University Unconventional Concept
OEI	=	one engine inoperative

LIST OF FIGURES

1.1	Schematic lay-out of the DUUC aircraft design	2
2.1	Isometric view of the DUUC ducted fan system	5
2.2	Side view of the DUUC ducted fan system	5
2.3	Schematic front view of the ducted propeller system	6
2.4	Schematic side view of the ducted propeller system	6
2.5	Schematic top view of the ducted propeller system	7
2.6	Schematic outline of the system components with their inflow velocities and inflow angles	7
2.7	Schematic outline of the velocity field of the ducted propeller system in power off conditions	8
2.8	Schematic outline of velocity field of a propeller according to the actuator disk theory	9
2.9	Schematic outline of the system component with their inflow velocities and inflow angles	10
2.10	Schematic outline of the system component with their lift contributions	11
2.11	Schematic outline of the system component with their drag contributions	12
2.12	Schematic outline of the system component with their lift and drag contributions	13
2.13	Schematic of the drag force on the centerbody	15
2.14	Schematic of the drag force on the propeller in power off conditions	16
2.15	Graph of the propeller thrust versus angle of attack for ducted propeller	17
2.16	Propeller thrust in power on conditions	18
2.17	Propeller normal force in power on conditions	18
2.18	Internal strut lift	20
2.19	Internal strut drag	20
2.20	External strut lift	21
2.21	External strut drag	22
2.22	Elevator lift	23
2.23	Elevator drag	23
3.1	Schematics of test model Grunwald & Goodson, all dimensions in inches	30
3.2	Schematics of test model by Grunwald & Goodson, all dimensions in inches	30
3.3	Input geometry for DFDC validation	30
3.4	Propeller blade geometric characteristics from Grunwald and Goodson	31
3.5	Duct pressure distribution from DFDC and XFOIL	32
3.6	Variation of lift and thrust with angle of attack for several advance ratios	34
3.7	Geometric view of the DUUC model mounted in the test section	37
3.8	Front view of the DUUC model mounted in the test section	37
3.9	Schematic front view of the DUUC ducted propeller scale model in the test section	38
3.10	Schematic side view of the DUUC ducted propeller scale model in the test section	38
3.11	Schematic top view of the DUUC ducted propeller scale model in the test section	39
3.12	Static installed thrust, model vs experiment	40
3.13	Lift vs elevator deflections at RPM = 6000, model vs experiment	40
3.14	Static side force vs rudder deflections at RPM = 9000, model vs experiment	40
3.15	Installed thrust vs elevator deflections at RPM = 6000, model vs experiment	41
3.16	Installed thrust vs rudder deflections at RPM = 9000, model vs experiment	41
3.17	Static side force vs rudder deflections at RPM = 6000, model vs experiment	42
3.18	Static side force vs rudder deflections at RPM = 9000, model vs experiment	42
3.19	Installed thrust vs rudder deflections at RPM = 6000, model vs experiment	42
3.20	Installed thrust vs rudder deflections at RPM = 9000, model vs experiment	42
3.21	Static lift force vs elevator deflections at various rudder deflections, RPM = 6000	43
3.22	Static side force vs rudder deflections at RPM = 9000, model vs experiment	43
3.23	Installed thrust vs elevator deflections at various rudder deflections, RPM = 6000	43

3.24	Installed thrust vs rudder deflections at RPM = 9000, model vs experiment	43
3.25	Static lift force vs elevator deflections at various rudder deflections, RPM = 6000	44
3.26	Static side force vs rudder deflections at RPM = 9000, model vs experiment	44
3.27	Installed thrust vs elevator deflections at various rudder deflections, RPM = 6000	44
3.28	Installed thrust vs rudder deflections at RPM = 9000, model vs experiment	44
3.29	Lift curve propeller off condition, analytical vs experimental	45
3.30	Drag polar propeller off condition, analytical vs experimental	45
3.31	Lift curve at $J = 0.42$, analytical vs experimental	45
3.32	Lift curve at $J = 0.28$, analytical vs experimental	45
3.33	Lift curve at $J = 0.56$, analytical vs experimental	46
3.34	Analytical lift curve, $J = 0.42$	46
3.35	Analytical lift curve, $J = 0.28$	46
3.36	Lift versus elevator deflections at $\alpha = 0$, $J = 0.83$	47
3.37	Analytical lift curve, $J = 0.56$	47
3.38	Elevator effectiveness for $\delta_e = 10^\circ$, model vs experiment, $J = 0.42$	47
3.39	Elevator effectiveness for $\delta_e = -10^\circ$, model vs experiment, $J = 0.42$, analytical vs experiment	47
3.40	Elevator effectiveness for $\delta_e = 10^\circ$, model vs experiment, $J = 0.28$	48
3.41	Elevator effectiveness for $\delta_e = -10^\circ$, model vs experiment, $J = 0.28$	48
3.42	Elevator effectiveness for $\delta_e = 10^\circ$, model vs experiment, $J = 0.28$	48
3.43	Elevator effectiveness for $\delta_e = -10^\circ$, model vs experiment, $J = 0.28$	48
3.44	Axial force curve at $J = 0.42$, analytical vs experimental	49
3.45	Axial force curve at $J = 0.28$, analytical vs experimental	49
3.46	Analytical axial force curve, $J = 0.42$	49
3.47	Analytical axial force curve, $J = 0.28$	49
3.48	Lift curve with control surface deflections at $J = 0.42$, analytical vs experimental	50
3.49	Axial force with control surface deflections, $J = 0.42$, analytical vs experiment	50
3.50	Comparison of lift curve and side force curve at $J = 0.42$	50
3.51	Comparison of lift curve and side force curve at $J = 0.28$	50
3.52	Comparison of lift curve and side force curve at $J = 0.42$	51
3.53	Comparison of lift curve and side force curve at $J = 0.28$	51
3.54	Comparison of lift curve and side force curve at $J = 0.28$	51
3.55	Comparison of lift curve and side force curve at $J = 0.28$	51
3.56	Static installed thrust, model vs experiment	52
3.57	Side force curve including elevator deflection at $J = 0.42$	52
3.58	Side force curve including elevator deflection at $J = 0.28$	52
3.59	Side force curve including elevator deflection at $J = 0.28$	53
3.60	Side force curve including elevator deflection at $J = 0.28$	53
3.61	Comparison of axial force curves at $J = 0.42$	53
3.62	Comparison of axial force curves at $J = 0.28$	53
3.63	Side force curve including elevator deflection at $J = 0.42$	54
3.64	Side force curve including elevator deflection at $J = 0.28$	54
3.65	Side force curve including elevator deflection at $J = 0.28$	54
3.66	Side force curve including elevator deflection at $J = 0.28$	54
3.67	Axial force curve including elevator deflection at $J = 0.42$	55
3.68	Axial force curve including elevator deflection at $J = 0.28$	55
3.69	Axial force curve including elevator deflection at $J = 0.28$	55
3.70	Axial force curve including elevator deflection at $J = 0.28$	55
3.71	Lift vs elevator deflection for various rudder deflections at $J = 0.42$	56
3.72	Lift vs elevator deflection for various rudder deflections at $J = 0.28$	56
3.73	Lift vs elevator deflection for various rudder deflections at $J = 0.28$	56
3.74	Lift vs elevator deflection for various rudder deflections at $J = 0.28$	56
3.75	Side force vs rudder deflection for various elevator deflections at $J = 0.42$	57
3.76	Side force vs rudder deflection for various elevator deflections at $J = 0.28$	57
3.77	Side force vs rudder deflection for various elevator deflections at $J = 0.28$	57
3.78	Side force vs rudder deflection for various elevator deflections at $J = 0.28$	57

4.1	Efficiency vs Reynolds number	62
4.2	Thrust coefficient C_T vs Reynolds number	62
4.3	Power coefficient vs Reynolds number	62
4.4	Thrust coefficient T_c vs Reynolds number	62
4.5	Pressure distribution around the duct for various Reynolds numbers	63
4.6	Pressure distribution around the centerbody for various Reynolds numbers	63
4.7	Efficiency vs advance ratio	64
4.8	Thrust coefficient C_T vs advance ratio	64
4.9	Power coefficient vs advance ratio	64
4.10	Thrust coefficient T_c vs advance ratio	64
4.11	Pressure distribution around the duct for several advance ratios	65
4.12	Pressure distribution around the centerbody for several advance ratios	65
4.13	Efficiency vs tip clearance	66
4.14	Thrust coefficient C_T vs tip clearance	66
4.15	Power coefficient C_P vs tip clearance	66
4.16	Thrust coefficient T_c vs tip clearance	66
4.17	Pressure distribution around the duct for variable tip clearance	67
4.18	Pressure distribution around the centerbody for variable tip clearance	67
4.19	Efficiency vs propeller position	68
4.20	Thrust coefficient C_T vs propeller position	68
4.21	Power coefficient C_P vs propeller position	68
4.22	Thrust coefficient T_c vs propeller position	68
4.23	Pressure distribution around the duct for variable propeller position	69
4.24	Pressure distribution around the centerbody for variable propeller position	69
4.25	Efficiency vs aspect ratio	70
4.26	Thrust coefficient C_T vs aspect ratio	70
4.27	Power coefficient C_P vs aspect ratio	70
4.28	Thrust coefficient T_c vs aspect ratio	70
4.29	Pressure distribution around the duct for variable aspect ratio	71
4.30	Pressure distribution around the centerbody for variable aspect ratio	71
4.31	Efficiency vs camber	72
4.32	Thrust coefficient C_T vs camber	72
4.33	Power coefficient C_P vs camber	72
4.34	Thrust coefficient T_c vs camber	72
4.35	Pressure distribution around the duct for variable camber	73
4.36	Pressure distribution around the centerbody for variable camber	73
4.37	Efficiency vs thickness	74
4.38	Thrust coefficient C_T vs thickness	74
4.39	Power coefficient C_P vs thickness	74
4.40	Thrust coefficient T_c vs thickness	74
4.41	Pressure distribution around the duct for variable duct airfoil thickness	75
4.42	Pressure distribution around the centerbody for variable duct airfoil thickness	75
A.1	Thrust reduced lift curves from experimental data	80
A.2	k factor vs thrust coefficient	81
B.1	Pressure vectors around the duct, $Re = 109,340$	83
B.2	Pressure vectors around the duct, $Re = 550,000$	83
B.3	Pressure vectors around the duct, $Re = 1,639,300$	83
B.4	Pressure vectors around the duct, $Re = 4,465,800$	83
B.5	Pressure vectors around the centerbody, $Re = 109,340$	84
B.6	Pressure vectors around the centerbody, $Re = 550,000$	84
B.7	Pressure vectors around the centerbody, $Re = 1,639,300$	84
B.8	Pressure vectors around the centerbody, $Re = 4,465,800$	84
B.9	Pressure vectors of the propeller, $Re = 109,340$	84
B.10	Pressure vectors of the propeller, $Re = 550,000$	84

B.11 Pressure vectors of the propeller, $Re = 1,639,300$	84
B.12 Pressure vectors of the propeller, $Re = 4,465,800$	84
B.13 Pressure vectors around the duct, $J = 0$	85
B.14 Pressure vectors around the duct, $J = 0.2$	85
B.15 Pressure vectors around the duct, $J = 0.4$	85
B.16 Pressure vectors around the duct, $J = 0.6$	85
B.17 Pressure vectors around the duct, $J = 0.8$	85
B.18 Pressure vectors around the duct, $J = 1.0$	85
B.19 Pressure vectors around the duct, $J = 1.2$	85
B.20 Pressure vectors around the duct, $J = 1.4$	85
B.21 Pressure vectors around the centerbody, $J = 0$	86
B.22 Pressure vectors around the centerbody, $J = 0.2$	86
B.23 Pressure vectors around the centerbody, $J = 0.4$	86
B.24 Pressure vectors around the centerbody, $J = 0.6$	86
B.25 Pressure vectors around the centerbody, $J = 0.8$	86
B.26 Pressure vectors around the centerbody, $J = 1.0$	86
B.27 Pressure vectors around the centerbody, $J = 1.2$	86
B.28 Pressure vectors around the centerbody, $J = 1.4$	86
B.29 Pressure vectors of the propeller, $J = 0$	87
B.30 Pressure vectors of the propeller, $J = 0.2$	87
B.31 Pressure vectors of the propeller, $J = 0.4$	87
B.32 Pressure vectors of the propeller, $J = 0.6$	87
B.33 Pressure vectors of the propeller, $J = 0.8$	87
B.34 Pressure vectors of the propeller, $J = 1.0$	87
B.35 Pressure vectors of the propeller, $J = 1.2$	87
B.36 Pressure vectors of the propeller, $J = 1.4$	87
B.37 Pressure vectors around the duct, $tc = 0\%$	88
B.38 Pressure vectors around the duct, $tc = 1\%$	88
B.39 Pressure vectors around the duct, $tc = 2\%$	88
B.40 Pressure vectors around the duct, $tc = 3\%$	88
B.41 Pressure vectors around the duct, $tc = 4\%$	88
B.42 Pressure vectors around the duct, $tc = 5\%$	88
B.43 Pressure vectors around the centerbody, $tc = 0\%$	89
B.44 Pressure vectors around the centerbody, $tc = 1\%$	89
B.45 Pressure vectors around the centerbody, $tc = 2\%$	89
B.46 Pressure vectors around the centerbody, $tc = 3\%$	89
B.47 Pressure vectors around the centerbody, $tc = 4\%$	89
B.48 Pressure vectors around the centerbody, $tc = 5\%$	89
B.49 Pressure vectors of the propeller, $tc = 0\%$	89
B.50 Pressure vectors of the propeller, $tc = 1\%$	89
B.51 Pressure vectors of the propeller, $tc = 2\%$	89
B.52 Pressure vectors of the propeller, $tc = 3\%$	89
B.53 Pressure vectors of the propeller, $tc = 4\%$	89
B.54 Pressure vectors of the propeller, $tc = 5\%$	89
B.55 Pressure vectors around the duct, $(x/c)_{\text{prop}} = 0$	91
B.56 Pressure vectors around the duct, $(x/c)_{\text{prop}} = 0.05$	91
B.57 Pressure vectors around the duct, $(x/c)_{\text{prop}} = 0.1$	91
B.58 Pressure vectors around the duct, $(x/c)_{\text{prop}} = 0.14$	91
B.59 Pressure vectors around the duct, $(x/c)_{\text{prop}} = 0.2$	91
B.60 Pressure vectors around the duct, $(x/c)_{\text{prop}} = 0.24$	91
B.61 Pressure vectors around the duct, $(x/c)_{\text{prop}} = 0.3$	91
B.62 Pressure vectors around the duct, $(x/c)_{\text{prop}} = 0.35$	91
B.63 Pressure vectors around the duct, $(x/c)_{\text{prop}} = 0.4$	91
B.64 Pressure vectors around the duct, $(x/c)_{\text{prop}} = 0.6$	91
B.65 Pressure vectors around the duct, $(x/c)_{\text{prop}} = 0.8$	91
B.66 Pressure vectors around the duct, $(x/c)_{\text{prop}} = 1.0$	91

B.67 Pressure vectors around the centerbody, $(x/c)_{\text{prop}} = 0$	92
B.68 Pressure vectors around the centerbody, $(x/c)_{\text{prop}} = 0.05$	92
B.69 Pressure vectors around the centerbody, $(x/c)_{\text{prop}} = 0.1$	92
B.70 Pressure vectors around the centerbody, $(x/c)_{\text{prop}} = 0.14$	92
B.71 Pressure vectors around the centerbody, $(x/c)_{\text{prop}} = 0.2$	92
B.72 Pressure vectors around the centerbody, $(x/c)_{\text{prop}} = 0.24$	92
B.73 Pressure vectors around the centerbody, $(x/c)_{\text{prop}} = 0.3$	92
B.74 Pressure vectors around the centerbody, $(x/c)_{\text{prop}} = 0.35$	92
B.75 Pressure vectors around the centerbody, $(x/c)_{\text{prop}} = 0.4$	92
B.76 Pressure vectors around the centerbody, $(x/c)_{\text{prop}} = 0.6$	92
B.77 Pressure vectors around the centerbody, $(x/c)_{\text{prop}} = 0.8$	92
B.78 Pressure vectors around the centerbody, $(x/c)_{\text{prop}} = 1.0$	92
B.79 Pressure vectors of the propeller, $(x/c)_{\text{prop}} = 0$	93
B.80 Pressure vectors of the propeller, $(x/c)_{\text{prop}} = 0.05$	93
B.81 Pressure vectors of the propeller, $(x/c)_{\text{prop}} = 0.1$	93
B.82 Pressure vectors of the propeller, $(x/c)_{\text{prop}} = 0.14$	93
B.83 Pressure vectors of the propeller, $(x/c)_{\text{prop}} = 0.2$	93
B.84 Pressure vectors of the propeller, $(x/c)_{\text{prop}} = 0.24$	93
B.85 Pressure vectors of the propeller, $(x/c)_{\text{prop}} = 0.3$	93
B.86 Pressure vectors of the propeller, $(x/c)_{\text{prop}} = 0.35$	93
B.87 Pressure vectors of the propeller, $(x/c)_{\text{prop}} = 0.4$	93
B.88 Pressure vectors of the propeller, $(x/c)_{\text{prop}} = 0.6$	93
B.89 Pressure vectors of the propeller, $(x/c)_{\text{prop}} = 0.8$	93
B.90 Pressure vectors of the propeller, $(x/c)_{\text{prop}} = 1$	93
B.91 Pressure vectors around the duct, $AR_{\text{duct}} = 0.5$	94
B.92 Pressure vectors around the duct, $AR_{\text{duct}} = 1$	94
B.93 Pressure vectors around the duct, $AR_{\text{duct}} = 1.45$	94
B.94 Pressure vectors around the duct, $AR_{\text{duct}} = 2$	94
B.95 Pressure vectors around the duct, $AR_{\text{duct}} = 3$	94
B.96 Pressure vectors around the centerbody, $AR_{\text{duct}} = 0.5$	95
B.97 Pressure vectors around the centerbody, $AR_{\text{duct}} = 1$	95
B.98 Pressure vectors around the centerbody, $AR_{\text{duct}} = 1.45$	95
B.99 Pressure vectors around the centerbody, $AR_{\text{duct}} = 2$	95
B.100 Pressure vectors around the centerbody, $AR_{\text{duct}} = 3$	95
B.101 Pressure vectors of the propeller, $AR_{\text{duct}} = 0.5$	95
B.102 Pressure vectors of the propeller, $AR_{\text{duct}} = 1$	95
B.103 Pressure vectors of the propeller, $AR_{\text{duct}} = 1.45$	95
B.104 Pressure vectors of the propeller, $AR_{\text{duct}} = 2$	95
B.105 Pressure vectors of the propeller, $AR_{\text{duct}} = 3$	95
B.106 Pressure vectors around the duct for NACA0012	96
B.107 Pressure vectors around the duct for NACA2412	96
B.108 Pressure vectors around the duct for NACA4412	96
B.109 Pressure vectors around the duct for NACA6412	96
B.110 Pressure vectors around the duct for NACA6412	96
B.111 Pressure vectors around the centerbody for NACA0012	97
B.112 Pressure vectors around the centerbody for NACA2412	97
B.113 Pressure vectors around the centerbody for NACA4412	97
B.114 Pressure vectors around the centerbody for NACA6412	97
B.115 Pressure vectors around the centerbody for NACA8412	97
B.116 Pressure vectors of the propeller for NACA0012	97
B.117 Pressure vectors of the propeller for NACA2412	97
B.118 Pressure vectors of the propeller for NACA4412	97
B.119 Pressure vectors of the propeller for NACA6412	97
B.120 Pressure vectors of the propeller for NACA8412	97
B.121 Pressure vectors around the duct for NACA006	98
B.122 Pressure vectors around the duct for NACA0012	98

B.123	Pressure vectors around the duct for NACA0018	98
B.124	Pressure vectors around the duct for NACA0024	98
B.125	Pressure vectors around the centerbody for NACA006	98
B.126	Pressure vectors around the centerbody for NACA0012	98
B.127	Pressure vectors around the centerbody for NACA0018	98
B.128	Pressure vectors around the centerbody for NACA0024	98
B.129	Pressure vectors of the propeller for NACA006	99
B.130	Pressure vectors of the propeller for NACA0012	99
B.131	Pressure vectors of the propeller for NACA0018	99
B.132	Pressure vectors of the propeller for NACA0024	99

LIST OF TABLES

3.1	Experimental vs numerical results	32
3.2	Experimental vs numerical results	33
3.3	Spanwise propeller inflow velocity from DFDC	33
3.4	Numerical results XROTOR	33
3.5	Experimental vs numerical results DFDC	34
3.6	Extrapolated values of $\frac{X}{T_0}$	35

1

INTRODUCTION

Ducted propellers have been subject of investigations for decades. Their widespread applications in both aircraft and marine ships make them interesting for aerodynamic analyses. The earliest investigations on the aerodynamics of ducted propellers date back to the late 1950s and 1960s, among which is the work of Mort and Gamse (1957) [1], who were one of the first to carry out a wind tunnel experiment on ducted propellers, and the wind tunnel test by Grunwald and Goodson (1962) [2], who studied the aerodynamics of ducted propellers in greater detail compared to most other researchers. Both of these experiments included angles of attack in their measurements. Kriebel (1964) [3] was one of the first to construct a theoretical model for the stability derivatives of a ducted propeller, but only validated them in static and axial inflow conditions. Other experiments, among which is the work of Black and Wainauski (1968) [4], focused solely on the effect of detailed design parameters on the axial performance of ducted fans. More recent investigations of such kind include Yilmaz and Erdem (2013) [5], who particularly investigated the effect of duct shape, Ahn and Lee (2004) [6], Abrego and Bulaga (2002) [7], Bi, Kimmel and Haas (2009) [8] and Anderson, Lehmkuehler, Ho, Wong and Hendrick (2013) [9]. Many of these investigations have been for small scale purposes only, such as Unmanned Aerial Vehicle (UAV) applications. These include among others the works of Graf and Ng (2008) [10] and Otsuka and Yoshida (2015) [11]. Finally, new theoretical models have been made more recently in Bontempo, Cardone, Manna and Vorraro (2013) [12] and CFD models have been made by Gaggero, Rizzo, Tani and Viviani (2012) [13].

The duct around the propeller is a means to increase the efficiency of the propeller at either the low or high end of the subsonic speed range in several ways. The benefits of a duct are highest in static conditions and become less strong as the speed increases. It reduces tip losses of the propeller, especially in static and low speed conditions, by eliminating reversed flow at the tips, hereby increasing the effective disk area. Furthermore, the duct increases the slipstream diameter, which contracts in case of an open propeller, this way increasing the thrust to power ratio as well. Finally, the duct also increases the thrust by generating a thrust force of its own. Contrary to the benefits in low speed conditions, the duct may decrease the efficiency compared to open propellers at high speeds. Besides increasing the efficiency, ducting a propeller has more benefits, among which are noise reduction in multiple ways and propeller shielding for safety. [14]

Considering the duct separately, it can be considered a circular wing, also known as a ring wing, consisting of an airfoil profile. Throughout the past decades, multiple researchers have attempted to construct models for the aerodynamic performance of ring wings. One of the first experiments in this field was done by Fletcher [15], who performed a wind tunnel test on five ring wings of different aspect ratios. The first analytical model for ring wings was proposed by Ribner [16], who used a lifting line theory. Weissinger [17] improved this model by using a lifting-surface theory. Next to the analytical models and Fletcher's experiment, other wind tunnel tests have been executed, including more recent experiments by Traub [18] and Maqsood and Go [19]. The last also constructed an analytical model based on previous experiments and their own test results.

Ducted propellers have been used in many different applications throughout the years, including autogyros, compound helicopters, seaplanes, short take-off aircraft (STOL), vertical take-off aircraft (VTOL) and airships. The majority of these applications has been for propulsion only. Few cases of ducted propellers, in which the duct was used to contribute to lift generation are known, usually for wing mounted ducted propellers. Steering applications of the duct are mainly seen in hovercraft and some UAV applications. Finally, using the duct as a means for stability and control have been very rare in aeronautics, with only a few cases

known of experimental projects which have never been worked out to real applications. Among these is the Mississippi XAZ-1 Marvelette from the Mississippi State University, an experimental aircraft from the 1960s.

The Delft University Unconventional Concept (DUUC) is a recent innovative aircraft design that uses ducted propellers in an unconventional way. The aircraft is a short take-off medium range aircraft, similar to the ATR-72 or F-50 propeller aircraft. The DUUC utilizes a system of two ducted propellers, mounted aft on the fuselage. This way, it replaces both the conventional wing mounted jet engines or open propellers and horizontal and vertical tail simultaneously. The ducted propeller system is thus utilized for both propulsive requirements and control and stability purposes. The ducted propeller system of the DUUC distinguishes from most conventional ducted propellers mainly by the inclusion of control surfaces, which are mounted to the hub at the trailing edge of the duct. They are used similarly to elevators and rudders in conventional aircraft tails. A schematic lay-out of a first conceptual design of the aircraft is shown in Fig. 1.1.

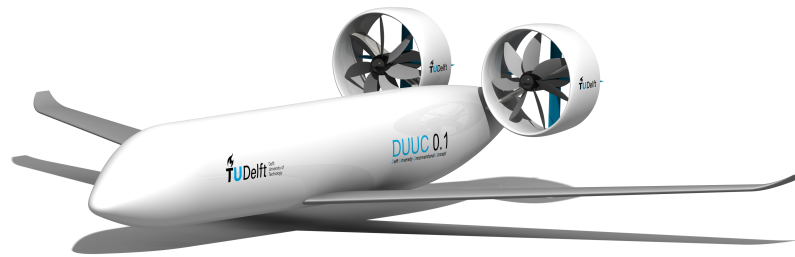


Figure 1.1: Schematic lay-out of the DUUC aircraft design

Considering past experiments on ducted propellers, configurations with exit vanes have been subject to research as well. Most applications of vanes in propellers have been for swirl recovery purposes only. However, vanes for thrust vectoring and control forces have been applied as well. Mort and Gamse included a vertical vane in their ducted propeller design. Furthermore, several UAV applications, such as the models by Mason and Berrier (1988) [20], Londenberg (2003) [21] and Sung and Hwang (2004) [22] have also included vanes for control force generation. However, models and experiments have been limited to certain conditions, such as static conditions and separate deflections of vanes for either yaw or pitch only. Most research has also focused on isolated ducted propellers and not on systems of two or more ducted propellers. The research on the DUUC ducted propeller system is particularly innovative in this area, since research is done on the aerodynamic performance of a system of two ducted propellers, particularly for propulsion, control and stability, over a range of several operational conditions and settings, such as simultaneous deflections of horizontal and vertical exit vanes and one engine inoperative (OEI) conditions.

1.1. RESEARCH OBJECTIVE AND RESEARCH QUESTIONS

In order to integrate the system of ducted propellers into the overall aircraft design of the DUUC, an aerodynamic performance study is critical. Knowledge on the effect of geometric design variables and operating conditions on the aerodynamic performance, significant for control and stability, is critical herein.

The research objective can therefore be specified as:

Develop a model for the aerodynamic performance of a ducted propeller system as a function of its geometric design over a range of operating conditions and inflow angles

From the research objective the following research question is deduced:

How does the geometry of a ducted propeller system affect its aerodynamic performance for propulsion, control and stability over a range of velocities, thrust settings and inflow angles?

The corresponding sub research questions are the following:

- *What is the aerodynamic performance of a ring wing in terms of lift, side force, drag and stall angle and how does it change with geometry?*
- *What is the effect of thrust on the lift, side force, drag and stall angle of a ducted propeller?*
- *What is the effect of ducted propeller geometry on total system thrust to power ratio and propeller thrust to power ratio over a range of velocities and thrust settings?*
- *What is the effect of control surface deflections on the lift, side force, drag and stall angle of a ducted propeller?*
- *What is the drag of a ducted propeller in case of engine out conditions and propeller feathering position?*
- *How can the aerodynamic coefficients for lift curve slope, side force curve slope, maximum lift, maximum side force and control surface derivatives be modeled as a function of ducted propeller geometry, operating conditions and thrust settings?*

The following sections deal with the research done on the DUUC ducted propeller system. In Ch. 2 the model that was constructed for the aerodynamic performance is outlined, which consists of an analytical and numerical part. In Ch. 3 this model is validated against existing experiments from literature and a wind tunnel test on a scale model of the DUUC ducted propeller system. Ch. 4 deals with the influence of the ducted fan geometry on its propeller efficiency and total efficiency. Finally, in Ch. 5 conclusions are drawn with respect to the aerodynamics of the system.

2

MODELING

This chapter discusses the aerodynamic performance model of the ducted propeller system of the DUUC aircraft. This model consists of an analytical and numerical part, which cooperate in order to estimate the lift, side force, thrust and drag of the system under various operating conditions and thrust settings.

2.1. SYSTEM BUILD UP

The ducted propeller system that is part of the DUUC aircraft consists of two ducted propellers, each consisting of a duct, which contains a propeller including centerbody that is attached to the duct by a strut. The ducted propellers also contain an external struts, which are used to attach the ducted propeller to the fuselage. Furthermore, the design includes control surfaces, which provide both longitudinal, directional and lateral control forces. In Fig 2.1 and 2.2 an isometric and side view of the first conceptual design of the DUUC ducted propeller system is shown.

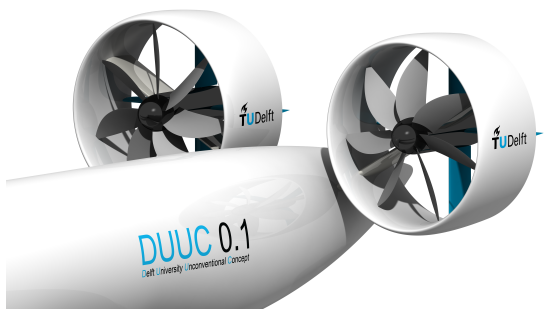


Figure 2.1: Isometric view of the DUUC ducted fan system

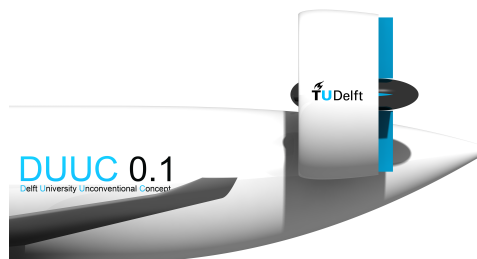


Figure 2.2: Side view of the DUUC ducted fan system

Schematics of the system, including all its dimensions and inflow angles are shown in Fig. 2.4, 2.5 and 2.3.

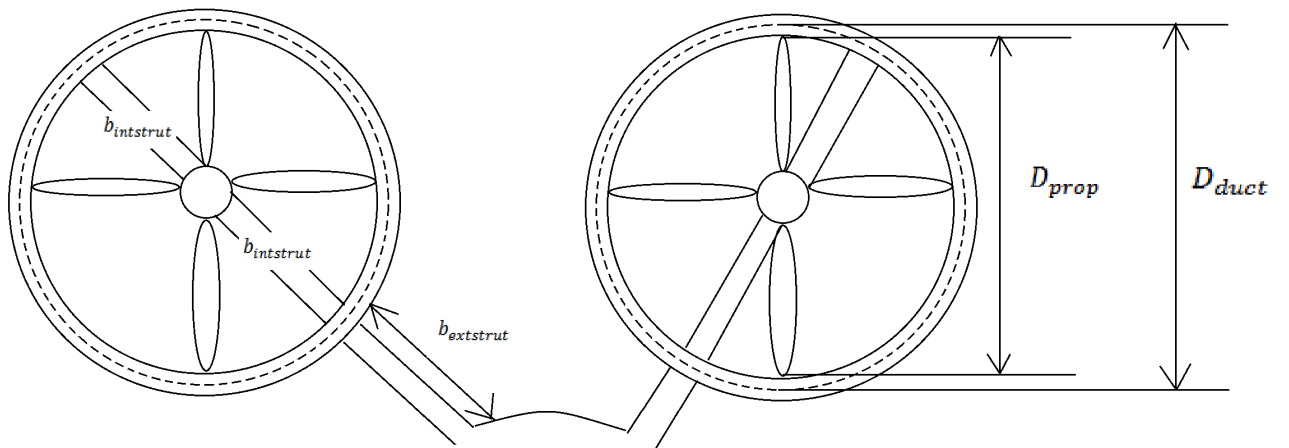


Figure 2.3: Schematic front view of the ducted propeller system

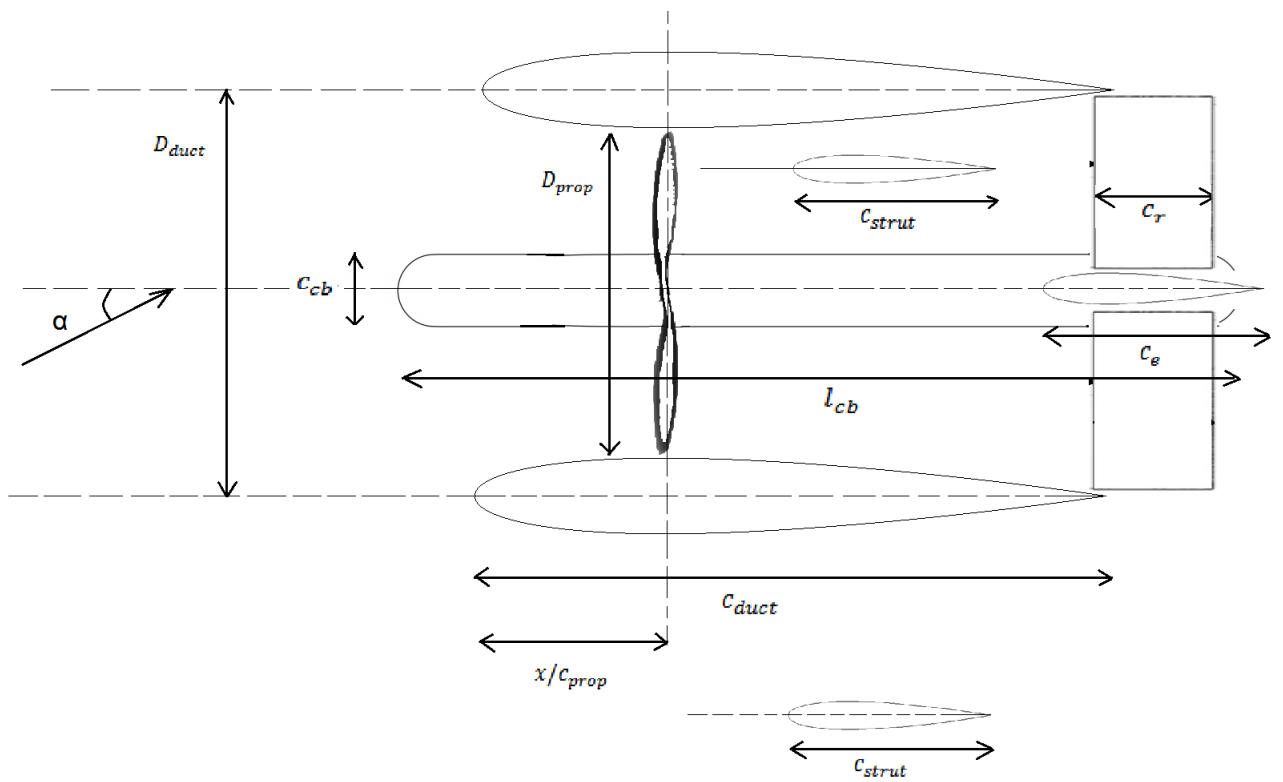


Figure 2.4: Schematic side view of the ducted propeller system

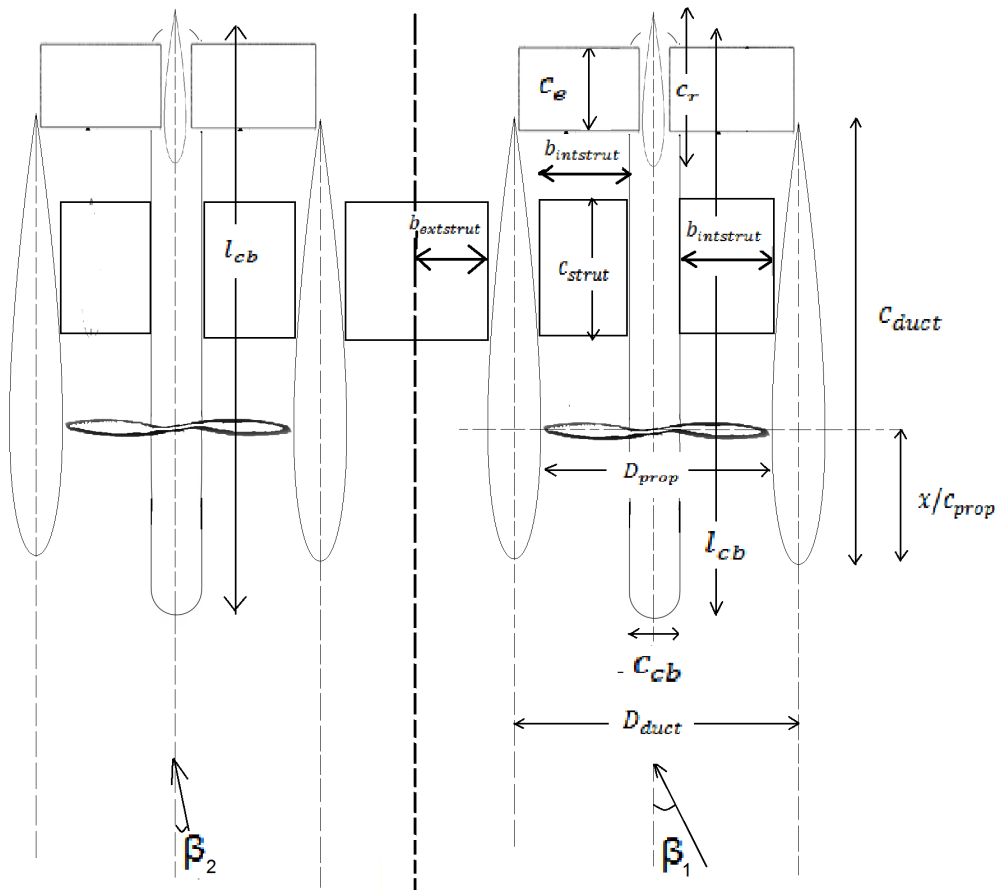


Figure 2.5: Schematic top view of the ducted propeller system

Considering the components of the complete system separately, the system can be divided into a duct, a centerbody, a propeller, an internal strut, an external strut and control surfaces. They all have different inflow velocities and inflow angles. This is shown schematically in Fig. 2.6.

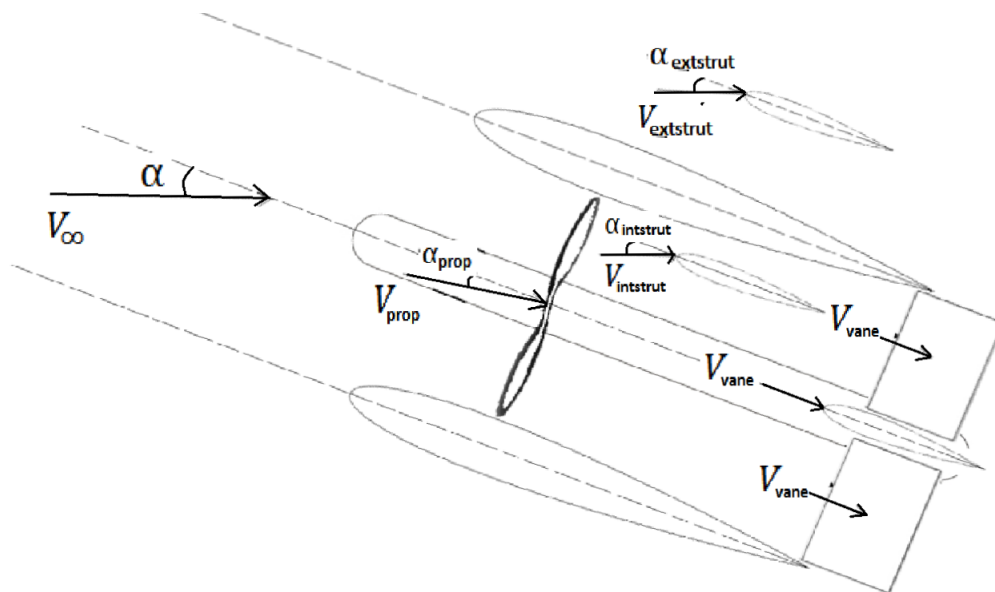


Figure 2.6: Schematic outline of the system components with their inflow velocities and inflow angles

2.1.1. COMPONENT VELOCITIES

Considering the velocities of the separate components, they are dependent on both the geometry and the power settings of the propeller. Therefore, the component velocities are different in power on and power off settings.

POWER OFF

In power off conditions, the ducted propeller is considered to be an axisymmetric duct, containing a centerbody with a propeller in feathering position. The feathering propeller and internal strut are assumed not to disturb the flow and influence the cross sectional area significantly. Furthermore, the influence on the velocity field by the curvature of the duct is neglected and it is assumed that the velocity field remains constant over angles of incidence. The velocities at different stations can then be determined by the continuity equation for incompressible flows, given by:

$$V_n A_n = \text{constant} \quad (2.1)$$

in which V_n and A_n are the velocity and cross-sectional area at an arbitrary station n in the ducted propeller, respectively. The cross sectional area of the ducted propeller is approximated as the cross sectional area of the duct minus the cross sectional area of the centerbody:

$$A = A_{\text{duct}} - A_{\text{cb}} = \frac{\pi}{4} D_{\text{duct}}^2 - \frac{\pi}{4} D_{\text{cb}}^2 \quad (2.2)$$

The cross sectional area of the duct is dependent on the inner diameter of the duct which varies in longitudinal direction and is dependent on the section airfoil. The cross sectional area of the centerbody is dependent on its diameter and may also vary in longitudinal direction. This is schematically illustrated in Fig. 2.7.

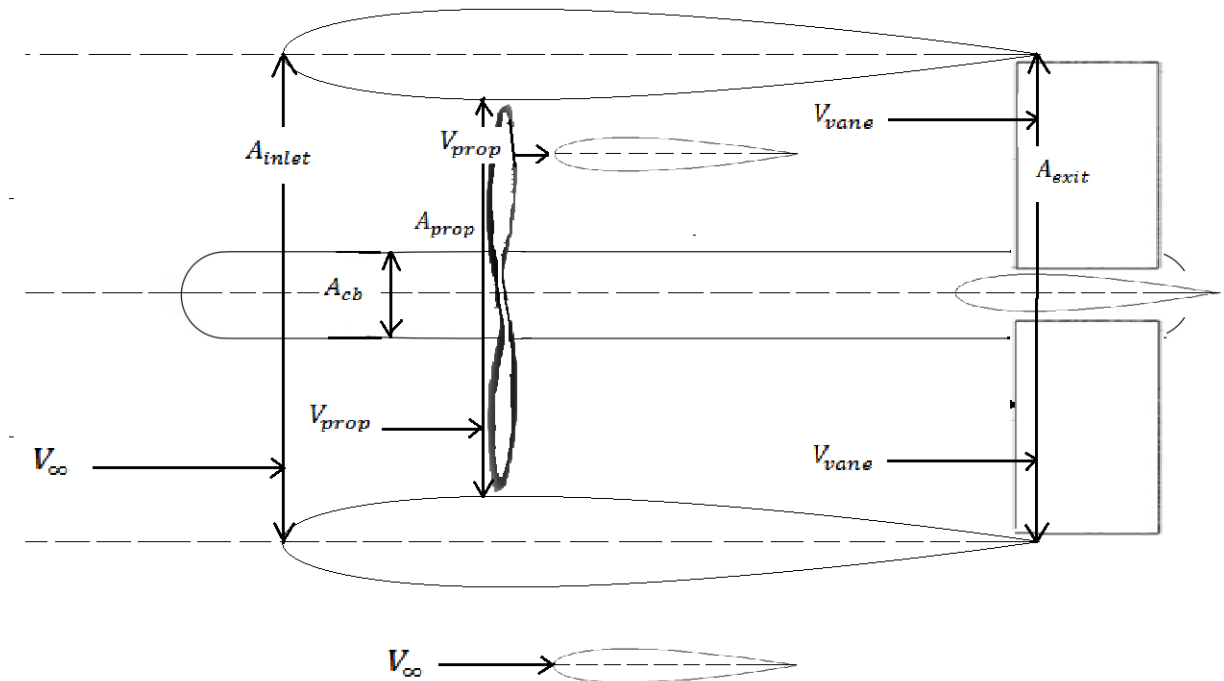


Figure 2.7: Schematic outline of the velocity field of the ducted propeller system in power off conditions

Hence, with Eq. 2.2 all component velocities can be determined based on the known freestream velocity V_∞ , freestream area A_∞ and ducted propeller geometry. Thus, in power off conditions, the velocities of the components can be modeled as follows:

- Duct: V_∞ , freestream velocity
- Centerbody: V_∞ , same as duct
- Propeller: V_{prop} , equal to the freestream velocity plus an induced velocity by the duct, determined by the continuity equation
- Internal strut: V_{prop} , since the internal strut is located directly downstream of the propeller
- External strut: V_∞ , since it is located outside of the duct
- Control surfaces: V_{vane} , determined by the continuity equation as well

POWER ON

In power on conditions, the component velocities are not determined by the continuity equation but are derived from the propeller velocity field of the actuator disk model [23].

The actuator disk theory [23] assumes that along the flow field of a propeller, there is no discontinuity in velocity, but a sudden pressure jump across the disk occurs. There is no swirling motion imparted to the flow downstream of the propeller and a uniform distribution of thrust along the propeller disk is assumed. Furthermore, no frictional drag of the propeller blades is taken into account. With this model, the flow field can roughly be divided into three stations; one upstream of the propeller, one just downstream of the propeller and one in the ultimate wake, far downstream of the propeller. This is shown in Fig. 2.8 from [23].

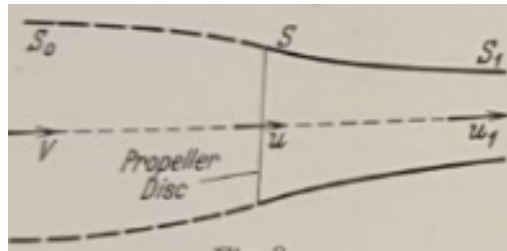


Figure 2.8: Schematic outline of velocity field of a propeller according to the actuator disk theory

From this theory, the following equation can be derived for the velocity in the ultimate wake:

$$u_1 = \sqrt{\frac{2 T_{\text{prop}}}{\rho S_{\text{prop}}} + V_{\text{prop}}^2} \quad (2.3)$$

in this equation T_{prop} is the propeller thrust.

The velocity just downstream of the propeller disk is equal to the average of the propeller inflow velocity and the ultimate wake velocity, hence:

$$u = \frac{1}{2}(V_{\text{prop}} + u_1) \quad (2.4)$$

In power on conditions the component velocities change in the following way:

- Duct: u , this is taken as an average velocity
- Centerbody: u , this is taken as an average velocity
- Propeller: V_{prop} , unchanged with respect to power off condition
- Internal strut: u , since it is located just downstream of the propeller
- External strut: V_∞ , unchanged with respect to power off condition
- Control surfaces: u_1 , since they are located far downstream of the propeller

This is schematically shown in Fig. 2.9.

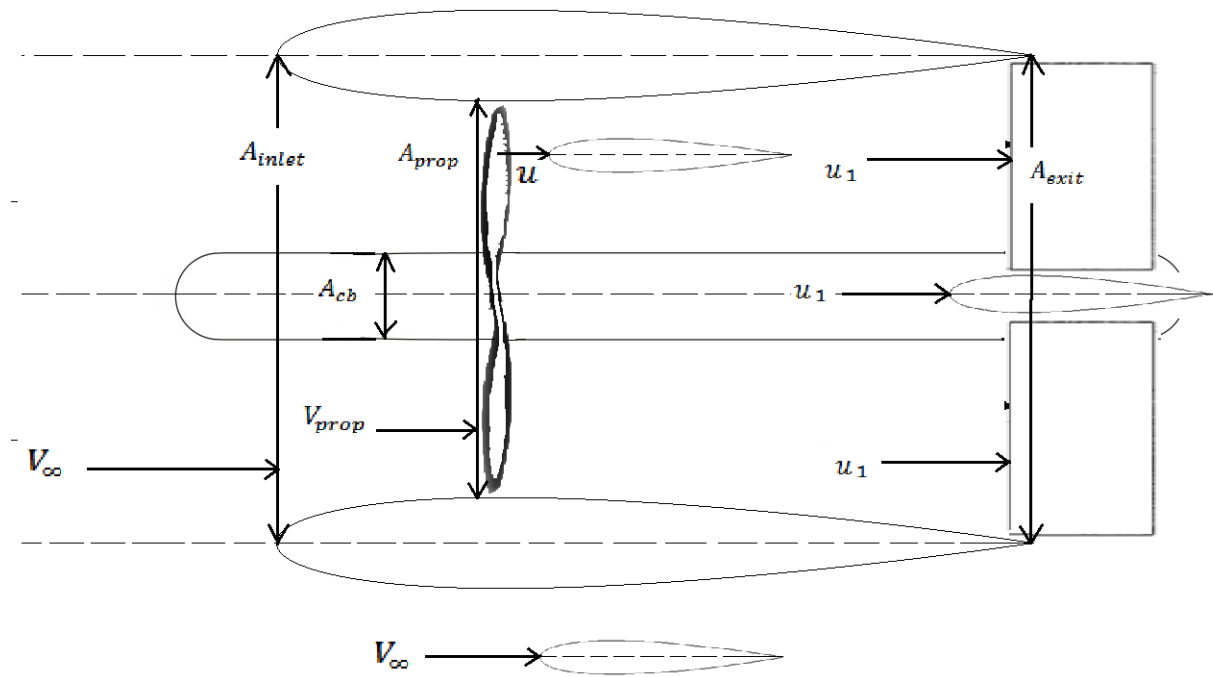


Figure 2.9: Schematic outline of the system component with their inflow velocities and inflow angles

The numerical model, which is described in section 2.6 can also determine the velocities at different stages of the ducted propeller in power on and power off conditions.

2.1.2. COMPONENT INFLOW ANGLES

Similar to the inflow velocities, the inflow angles of the different components depend on the geometry and power settings of the propeller as well. Therefore, they also differ in power on and power off conditions.

POWER OFF

The duct, in power off conditions, is not influenced by any other geometry upstream of it. Therefore, the freestream angle of attack is used for the duct. The same angle of attack is used for the centerbody, since the centerbody leading edge is also not influenced upstream of it. Considering the propeller, the flow may not be completely straightened before it reaches the propeller, depending on where the propeller is located inside the duct. The flow streamlines follow the duct profile closely around the duct, such that the inflow orientation of the flow is approximately constant over the range of angle of attack in the upper and lower part of the duct. Going inward to the middle and to the sides in the middle of the duct, the flow becomes more inclined. Therefore the resultant effective angle of attack is assumed to be smaller than the freestream angle of attack. It is difficult to predict the resultant effective angle of attack that the propeller sees as a function of the duct airfoil profile, but it is assumed that its value lies between zero and the freestream value. Therefore, the propeller angle of attack is assumed to be:

$$0 < \alpha_{prop} < \alpha \quad (2.5)$$

In power off conditions, the same angle of attack is assumed for the internal strut.

The external strut has an inflow angle which is influenced by the fuselage and the duct's outer surface. It is therefore also difficult to model this angle accurately and it is assumed that this angle also lies between zero and the freestream value. Finally, it is assumed that the flow has completely straightened at the duct exit under influence of the duct surface, such that the control surfaces do not experience an angle of attack. Thus, the following angles of incidence are assumed for the system components in power off conditions:

- Duct: α , the freestream angle of attack
- Centerbody: α , the freestream angle of attack

- Propeller: $0 < \alpha_{\text{prop}} < \alpha$
- Internal strut: $0 < \alpha_{\text{intstrut}} < \alpha$
- External strut: $0 < \alpha_{\text{extstrut}} < \alpha$
- Control surfaces: $\alpha_{\text{vane}} = 0$

POWER ON

In power on conditions, the duct, centerbody and external strut flow are not affected. Neglecting the swirl in the slipstream, it is furthermore assumed that the downward and upward components of the swirl approximately cancel out, similar to the sideward components of the swirl, such that the inflow of the control surfaces can still be modeled as axial flow. Thus, only the internal strut's inflow angle changes. This angle depends on the propeller inflow angle and the propeller induced downwash. This is illustrated by the following equation:

$$\alpha_{\text{intstrut}} = \left(1 - \frac{d\epsilon_{\text{slip}}}{d\alpha_{\text{prop}}}\right) \alpha_{\text{prop}} \quad (2.6)$$

Ignoring the swirling motion of the flow in the slipstream and the straightening effect of the duct, an estimation of the propeller induced downwash can be taken from John de Young [24]. The downwash effect is then given by the following equation:

$$\frac{d\epsilon_{\text{slip}}}{d\alpha_{\text{prop}}} = \frac{T_c}{4 + \frac{8}{7}T_c} + \frac{(C_{N_{\text{prop}}})_{T_c=0}(1 + 1.3T_c)^{\frac{1}{2}}}{4 + 2T_c} \quad (2.7)$$

where $C_{N_{\text{prop}}}$ is the additional propeller normal force under angles of incidence.

2.2. LIFT AND DRAG

The lift and drag of the total system is composed of the sum of the lift and drag contributions of all components. These lift and drag contributions depend on the aerodynamic properties of the components and their inflow velocities and inflow angles, which were outlined in the previous section. A schematic view of the ducted fan system, with its component lift and drag contributions is shown in Fig. 2.10 and 2.11.

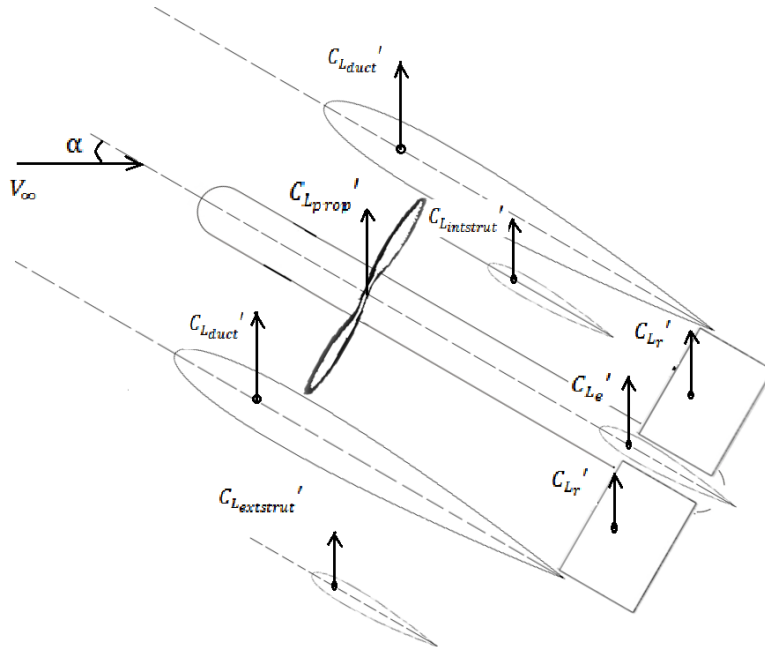


Figure 2.10: Schematic outline of the system component with their lift contributions

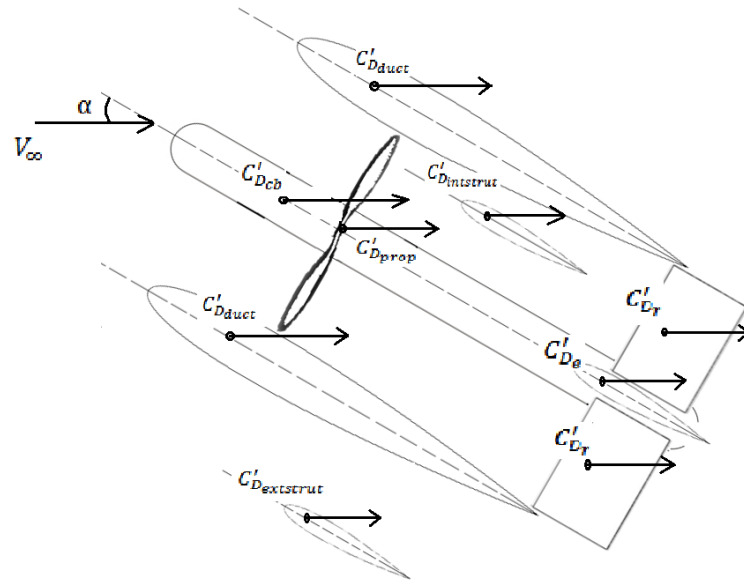


Figure 2.11: Schematic outline of the system component with their drag contributions

The lift and drag of all components are taken normal to and parallel to the freestream velocity, respectively. Also, the lift and drag of all components are normalized with respect to the projected area of the duct to obtain the coefficients of the total system. These coefficients are denoted with a prime. The total lift and drag consist of the sum of the lift and drag of the components, respectively. The drag includes an additional component due to interference effects between several components. This way, the total system's lift and drag coefficient can be expressed as:

$$C_{L_{total}} = C'_{L_{duct}} + C'_{L_{cb}} + C'_{L_{prop}} + C'_{L_{intstrut}} + C'_{L_{extstrut}} + C'_{L_{vanes}} \quad (2.8)$$

$$C_{D_{total}} = C'_{D_{duct}} + C'_{D_{cb}} + C'_{D_{prop}} + C'_{D_{intstrut}} + C'_{D_{extstrut}} + C'_{D_{vanes}} + C'_{D_{interf}} \quad (2.9)$$

2.2.1. DUCT

Throughout the past decades, multiple researchers have attempted to construct models for ring wings, based on aerodynamic theory and experiments. It should be noted that all experiments done have been in the Reynolds number range of $Re = 700,000 - 2,500,000$ based on the ring wing's chord. Comparing the different analytical models to the different experimental data, it can be concluded that Weissinger's model is the best approximation for the lift of ring wings, both in the low and high aspect ratio range, having the best correspondence to both old and new experimental data. The lift and drag of the duct are schematically shown in Fig. 2.12 from [17].

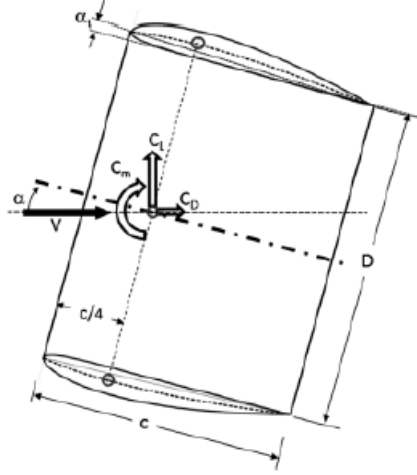


Figure 2.12: Schematic outline of the system component with their lift and drag contributions

The equation that is used for the lift curve slope of the duct only in power off conditions is Weissinger's lift model [17] and given by the following equation:

$$C_{L\alpha, \text{duct}} = \frac{\pi}{2} \zeta_W c_{l\alpha} \quad (2.10)$$

in which ζ_W is given by the following equation:

$$\zeta_W = \frac{1}{1 + \lambda(\pi/2) + \lambda \arctan(1.2\lambda)} \quad (2.11)$$

and λ is given by:

$$\lambda = \frac{1}{AR} \quad (2.12)$$

Furthermore, $c_{l\alpha}$ is the lift curve slope of the duct airfoil.

Equation 2.10 can thus be used to approximate the lift in the linear part of the lift curve of the duct only, hence before the onset of stall. The lift coefficient in this region is determined by:

$$C_{L_{\text{duct}}} = C_{L\alpha, \text{duct}} \cdot \alpha \quad (2.13)$$

in which α is the angle of attack of the freestream flow with respect to the duct's centerline.

Having a model for the lift of the duct in power off conditions, the propeller effect on the lift must be added for power on conditions. Defining a factor k_{prop} , which relates the lift curve slope of the duct only/propeller off condition to the lift curve slope of the duct only/propeller on condition, the following equation is obtained:

$$C_{L\alpha, \text{duct, on}} = (1 + k_{\text{prop}}) C_{L\alpha, \text{duct}} \quad (2.14)$$

This factor k_{prop} is a function of the propeller and centerbody thrust coefficient $T_{c_{\text{propcb}}}$ and is given by:

$$k = 0.2 \cdot \sqrt{T_{c_{\text{propcb}}}} \quad (2.15)$$

The method by which this factor is determined can be found in Appendix A.

Integrating this approximation into the analytical lift model, the lift of the duct under influence of the propeller can be modeled by:

$$C_{L_{\text{duct, on}}} = C_{L\alpha, \text{duct, on}} \cdot \alpha \quad (2.16)$$

The drag of the duct can be modeled as consisting of a zero lift drag component and a lift induced drag under angles of attack. The zero lift drag coefficient can be determined based on a friction coefficient, wetted area and corrections factors. The zero lift drag for a conventional wing can be determined from Sadraey [25] by the following equation:

$$C_{D_0} = C_f f_{tc} f_M \frac{S_{\text{wet}}}{S} \left(\frac{c_{d_{\min}}}{0.004} \right)^{0.4} \quad (2.17)$$

in which C_f is the skin friction coefficient for hydraulically flat plates, based on the Prandtl relationship given by:

$$C_f = \begin{cases} \frac{0.455}{[\log_{10}(Re)]^{2.58}}, & \text{if flow is turbulent} \\ \frac{1.327}{\sqrt{Re}}, & \text{if flow is laminar} \end{cases} \quad (2.18)$$

Flow above Reynolds numbers of 200,000 may assumed to be fully turbulent, so depending on the operating conditions of the ducted propeller system, either one of the friction coefficients is used.

The Reynolds number is normally based on the mean aerodynamic chord of a wing and the freestream velocity. For the duct, it is given as:

$$Re_{\text{duct}} = \frac{\rho V_{\text{duct}} c_{\text{duct}}}{\mu} \quad (2.19)$$

For the ring wing duct, the chord is constant but the velocity field is not the same as that on a regular wing because of the difference in geometry between a ring wing and a planar wing. On top of that, in power on conditions, the presence of the propeller changes the velocity as well. However, since the velocity of the duct is assumed to be the freestream velocity in power off conditions, it is also used for determining the Reynolds number in power off conditions. The velocity u is used for the Reynolds number in power on conditions.

The factor f_{tc} is dependent on the thickness ratio of the duct airfoil and is given by:

$$f_{tc} = 1 + 2.7 \left(\frac{t}{c} \right)_{\max} + 100 \left(\frac{t}{c} \right)_{\max}^4 \quad (2.20)$$

The factor f_M is a Mach correction given by:

$$f_M = 1 - 0.08 M^{1.45} \quad (2.21)$$

For a conventional wing, the wetted area can be estimated by twice the exposed area and the assumption that the wing is a thin box with a thickness, equal to half of the airfoil thickness. This yields the equation:

$$S_{\text{wet}} = 2 \left[1 + 0.5 \left(\frac{t}{c} \right)_{\max} \right] b c \quad (2.22)$$

For a ring wing, the same assumption can be made of it being a thin box with a thickness equal to half the airfoil thickness. The wetted area of the duct then becomes the following:

$$S_{\text{wet,duct}} = 2 \pi D_{\text{duct}} c_{\text{duct}} + 2 \pi D_{\text{duct}} \cdot 0.5 \left(\frac{t}{c} \right)_{\max} c_{\text{duct}} \quad (2.23)$$

Finally $c_{d_{\min}}$ is the minimum drag coefficient of the airfoil section of the duct.

Similar to lift, the induced drag of a ring wing has been subject of research for decades as well. Several researches have shown that the induced drag of ring wings is lower than that of planar wings of the same aspect ratio. The model for induced drag is similar to that of planar wings:

$$C_{D_i} = \frac{C_L^2}{\pi A R e} = \frac{C_L^2}{2\pi A R} \quad (2.24)$$

Hence the Oswald factor e is equal to 2 for a ring wing.

Having set up a model for the lift and drag of the duct, the duct lift and drag coefficients of the total system become:

$$C'_{L_{\text{duct}}} = C'_{L_{\text{duct}}} \left(\frac{V_{\text{duct}}}{V_{\infty}} \right)^2 \quad (2.25)$$

$$C'_{D_{\text{duct}}} = (C'_{D_{0,\text{duct}}} + C'_{D_{i,\text{duct}}}) \left(\frac{V_{\text{duct}}}{V_{\infty}} \right)^2 \quad (2.26)$$

where V_{duct} is given by V_{∞} or u for power off and power on conditions, respectively.

2.2.2. CENTERBODY

The centerbody of a ducted propeller has a cylindrical shape with a spherical spinner at the leading edge and optionally also a spherical part at the trailing edge. It is assumed that the centerbody does not generate lift under angles of attack, both in power on and in power off conditions. Therefore the centerbody only contributes to the drag, which consists of a zero lift drag component only. Fig. 2.13 illustrates this.

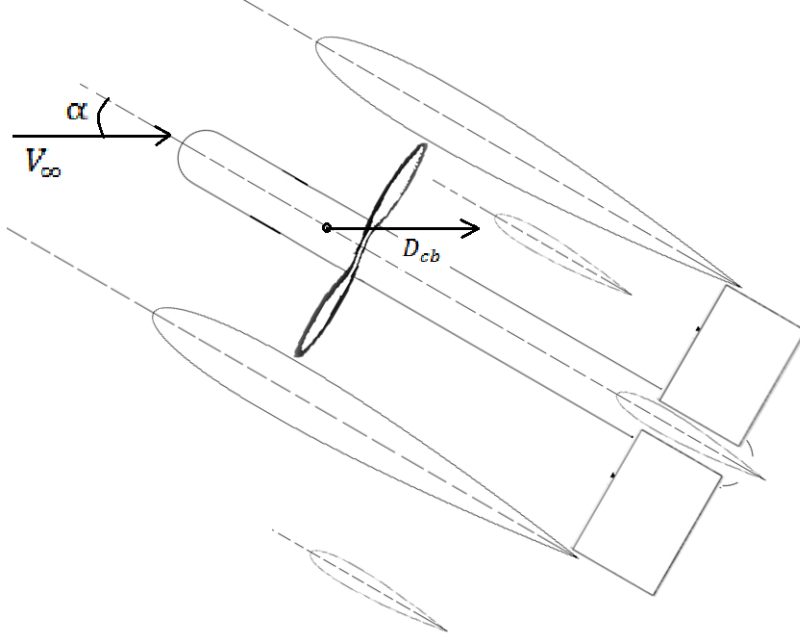


Figure 2.13: Schematic of the drag force on the centerbody

For the centerbody the zero lift drag model of a fuselage is taken from [25], since the centerbody has a similar shape. This drag model is given by:

$$C_{D_0,cb} = C_f f_{ld} f_M \frac{S_{wet,cb}}{S_{duct}} \quad (2.27)$$

Here, C_f is the same friction coefficient, as given in equation 2.18. f_{ld} is a factor, which depends on the length to diameter ratio, given by:

$$f_{ld} = 1 + \frac{60}{(l/d)^3} + 0.0025 \frac{l}{d} \quad (2.28)$$

The Mach number factor f_M is the same as given in Equation 2.21.

In power off conditions and power on conditions, the Reynolds number and Mach number are both determined, based on the freestream velocity V_∞ and propeller velocity u , respectively.

The wetted area of the centerbody is approximated by:

$$S_{wet,cb} = \pi D_{cb} f_1 l_{cb} + (1 - f_1) l_{cb} f_2 \pi D_{cb} \quad (2.29)$$

in which f_1 is the fraction of the length of the straight part of the centerbody to the total length, thus the part that does not include the spinner. f_2 is the factor used to calculate the average circumference of the spinner. It is assumed that the centerbody generates no lift under angles of attack, hence its drag only consists of the zero lift drag.

Therefore:

$$C_{D_{cb}} = C_{D_0,cb} \quad (2.30)$$

Since it is assumed that the velocity of the centerbody does not change in direction in different conditions, the centerbody drag coefficient of the total system is:

$$C'_{D_{cb}} = C_{D_{cb}} \left(\frac{V_{cb}}{V_{\infty}} \right)^2 \quad (2.31)$$

where V_{cb} is given by V_{∞} or u in power off or power on settings, respectively.

2.2.3. PROPELLER

The propeller consists of a number of blades, consisting of one or more airfoil profiles over their span. These blades are attached to the centerbody and are rotating in power on conditions. In power off conditions, they are placed in feathering position, in which their orientation is parallel to the airfoil, in order to minimize drag.

POWER OFF

In power off conditions, the propeller does not add significantly to the lift of the system, but has a significant contribution to the drag of the system. This is illustrated in Fig. 2.14.

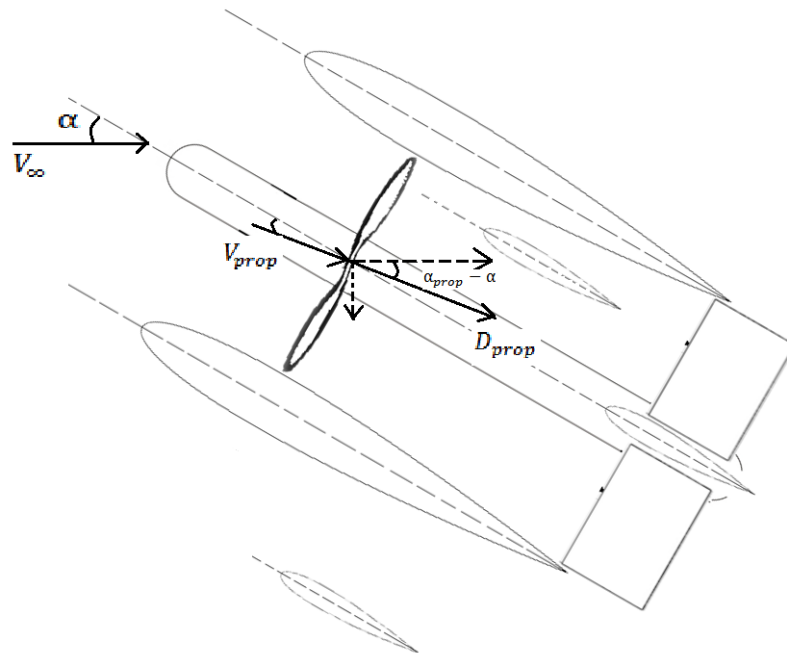


Figure 2.14: Schematic of the drag force on the propeller in power off conditions

It can be seen that the propeller experiences a drag force parallel to its inflow velocity V_{prop} .

In engine out conditions, when the propeller is in its feathering position, the drag of the propeller can be estimated by the friction drag of the propeller blades. Propeller blades consist of a varying collection of airfoil sections along their span. For simplification purposes, the propeller blades can be considered flat plates with a chord length equal to the average blade chord and being placed exactly in the streamwise direction of the flow in the feather condition. The drag of one propeller blade is then simply given by:

$$C_{D_{0,blade}} = C_f \quad (2.32)$$

which is the skin friction coefficient for a flat plate.

Hence the total drag coefficient of the propeller in power off conditions consists of these drag contributions by all blades:

$$C_{D_{prop,off}} = n \cdot C_{D_{0,blade}} \quad (2.33)$$

where n is the number of propeller blades.

Converting this to the propeller's lift and drag coefficients of the total system in power off conditions, the following equations are obtained:

$$C'_{D_{\text{prop,off}}} = C_{D_{\text{prop,off}}} \cdot \cos(\alpha_{\text{prop}} - \alpha) \cdot n \cdot \frac{S_{\text{wetblade}}}{S_{\text{duct}}} \left(\frac{V_{\text{prop}}}{V_{\infty}} \right)^2 \quad (2.34)$$

$$C'_{L_{\text{prop,off}}} = C_{D_{\text{prop,off}}} \cdot \sin(\alpha_{\text{prop}} - \alpha) \cdot \frac{S_{\text{wetblade}}}{S_{\text{duct}}} \left(\frac{V_{\text{prop}}}{V_{\infty}} \right)^2 \quad (2.35)$$

where V_{prop} is the propeller velocity.

POWER ON

In power on conditions, the propeller has a significant contribution to the lift but no significant contribution to the drag. The first contribution to the lift of the system is due to the combined propeller and centerbody thrust, which is assumed to remain constant under angles of attack. This is shown in Fig. 2.16. It was shown in [2] that the combined propeller and centerbody thrust remain approximately constant under angles of attack. The plot from [2] illustrating this effect is shown in Fig. 2.15.

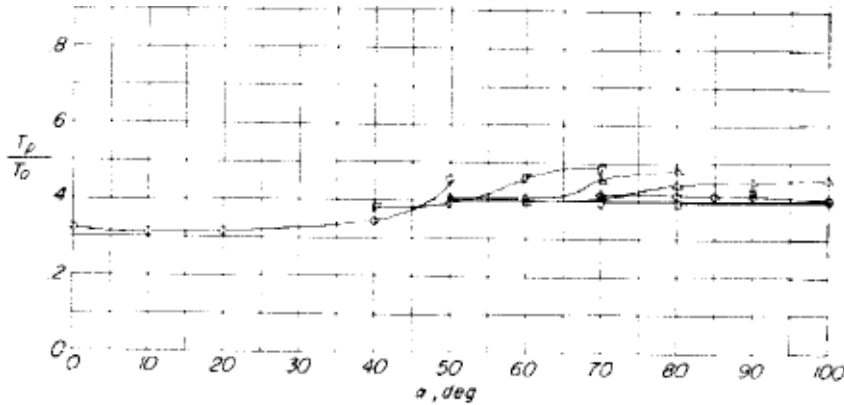


Figure 2.15: Graph of the propeller thrust versus angle of attack for ducted propeller

The second contribution to the lift, also contributing to the drag of the system, is the propeller normal force under angles of attack. The contributions to the lift and drag by the propeller normal force are illustrated in Fig. 2.17.

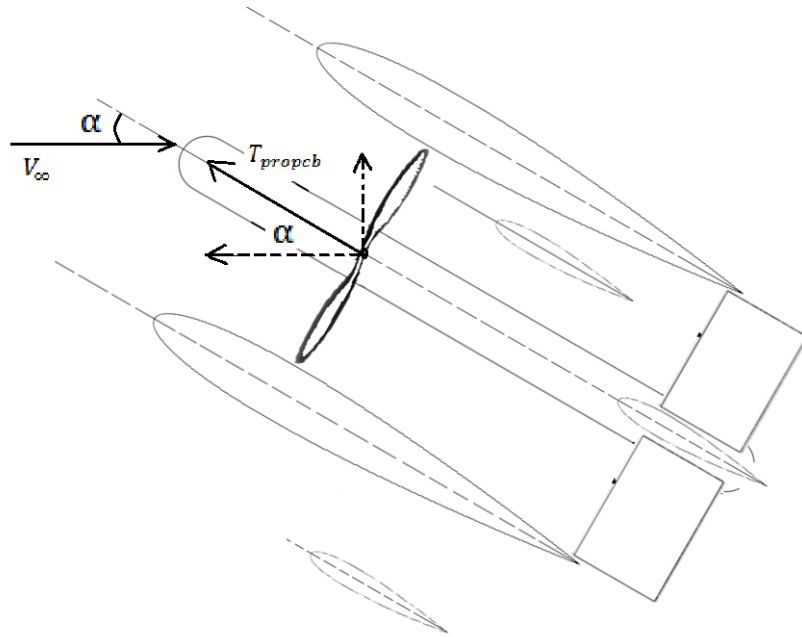


Figure 2.16: Propeller thrust in power on conditions

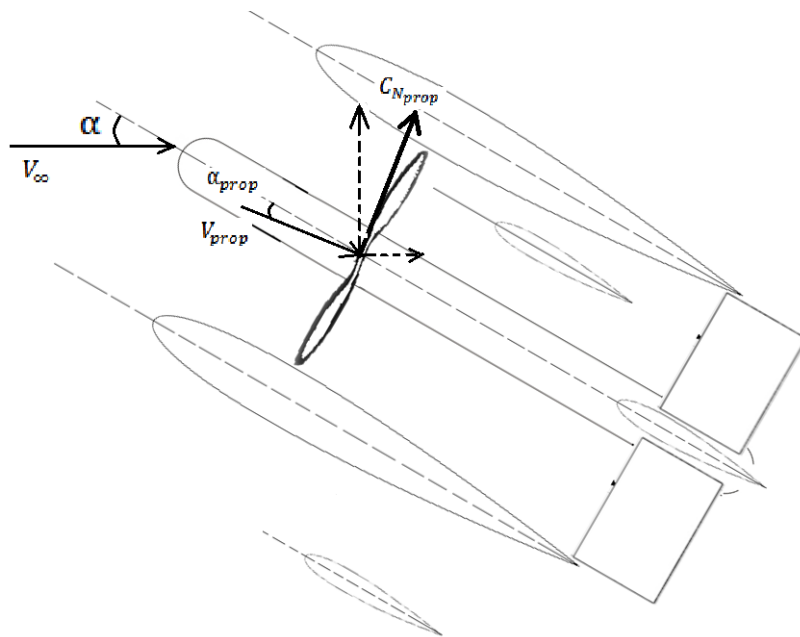


Figure 2.17: Propeller normal force in power on conditions

The first contribution of the propeller to the lift of the total system is thus due to the propeller and centerbody thrust and is equal to its vertical component:

$$C'_{L_{prop,on,1}} = T_{c_{propcb}} \cdot \sin(\alpha) \quad (2.36)$$

It is assumed that the drag of the propeller is very low compared to its thrust in power on conditions, such that it can be neglected.

The second contribution is due to the propeller normal force $C_{N_{prop}}$, that is generated by the propeller under its angle of attack α_{prop} . The model for the normal force of the propeller under an incidence angle is given by the following equation, from de Young:

$$C_{N_{\alpha_{\text{prop}}}} = \frac{4.25\sigma_e}{1+2\sigma_e} \sin(\beta+8) \left(1 + \frac{3T'_c}{8(1+\frac{2}{3}T'_c)^{\frac{1}{2}}} \right) \quad (2.37)$$

Here $C_{N_{\alpha_{\text{prop}}}}$ is the derivative of the propeller normal force with respect to its angle of attack. The propeller normal force is defined as:

$$C_{N_{\text{prop}}} = \frac{N_{\text{prop}}}{\frac{1}{2} \rho V_{\text{prop}}^2 S_{\text{prop}}} \quad (2.38)$$

where S_{prop} is given by:

$$S_{\text{prop}} = \pi R_{\text{prop}}^2 \quad (2.39)$$

Furthermore σ_e is the effective solidity of the propeller, given by:

$$\sigma_e = \frac{\bar{b}'}{b'_{0.75}} \sigma \quad (2.40)$$

Here, $\frac{\bar{b}'}{b'_{0.75}}$ is the ratio of the average blade chord to the threequarter radius blade chord and \bar{b}' is the average blade chord, which can be approximated by:

$$\bar{b}' = 0.16 \left(\frac{5}{4} b'_{0.25} + 2b'_{0.50} + 2b'_{0.75} + b'_{0.95} \right) \quad (2.41)$$

The propeller solidity is given by:

$$\sigma = \frac{4B}{3\pi} \frac{b'_{0.75}}{D} \quad (2.42)$$

in which B is the number of blades and D is the propeller diameter.

Furthermore, β is the blade angle at 0.75R plus 5 degrees. Finally T'_c is given by:

$$T'_c = \frac{T}{\frac{1}{2} \rho V_{\text{prop}}^2 S_{\text{prop}}} \quad (2.43)$$

The normal force of the propeller is then:

$$C_N = C_{N_{\alpha_{\text{prop}}}} \cdot \alpha_{\text{prop}} \quad (2.44)$$

This normal force contributes to the total system's lift and drag as follows:

$$C'_{L_{\text{prop,on},2}} = C_{N_{\text{prop}}} \cos(\alpha - \alpha_{\text{prop}}) \frac{S_{\text{prop}}}{S_{\text{duct}}} \left(\frac{V_{\text{prop}}}{V_{\infty}} \right)^2 \quad (2.45)$$

The drag contribution to the system is given by:

$$C'_{D_{\text{prop,on}}} = C_{N_{\text{prop}}} \sin(\alpha - \alpha_{\text{prop}}) \frac{S_{\text{prop}}}{S_{\text{duct}}} \left(\frac{V_{\text{prop}}}{V_{\infty}} \right)^2 \quad (2.46)$$

The total lift contribution of the propeller to the system in power on conditions is thus:

$$C'_{L_{\text{prop,on}}} = C'_{L_{\text{prop,on},1}} + C'_{L_{\text{prop,on},2}} \quad (2.47)$$

2.2.4. INTERNAL STRUT

Directly downstream of the propeller is the internal strut, which is used to attach the centerbody to the duct. The internal strut contributes to both the lift and the drag. This is illustrated in Fig. 2.18 and 2.19.

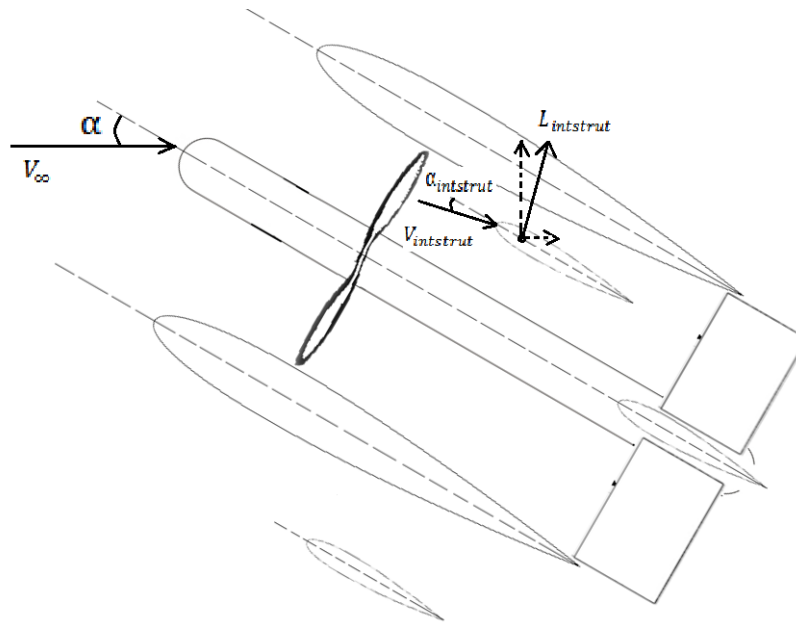


Figure 2.18: Internal strut lift

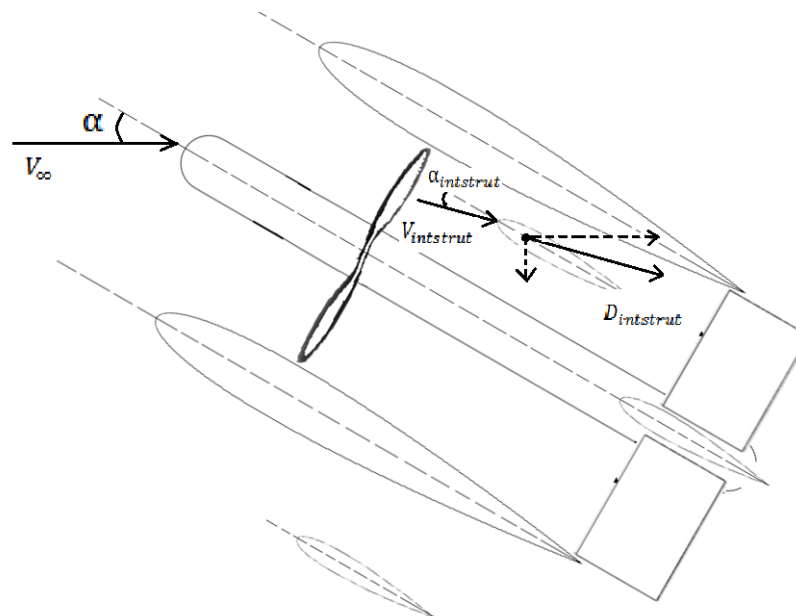


Figure 2.19: Internal strut drag

Both the internal and the external part of the strut are clamped on both sides of their spans, such that they can be modeled as infinite wings constructed from a particular airfoil section, mounted under an angle in lateral direction. Therefore, the lift curve slope of this part of the strut is assumed to be the ideal 2D slope 2π :

$$C_{L_{\alpha, strut}} = c_{l_{\alpha}} = 2\pi \quad (2.48)$$

The lift coefficient of the internal strut is then modeled by the following equation:

$$C_{L_{intstrut}} = C_{L_{\alpha, strut}} \cdot \alpha_{intstrut} \cdot \cos(\theta_{strut}) \quad (2.49)$$

θ_{strut} is the lateral angle under which the internal and external strut are mounted.

As can be derived from Fig. 2.18, the lift and drag components of the internal strut in the total system are obtained from the internal strut's lift coefficient as:

$$C'_{L_{\text{instrut},1}} = C_{L_{\text{instrut}}} \cdot \cos(\alpha - \alpha_{\text{instrut}}) \cdot \frac{S_{\text{instrut}}}{S_{\text{duct}}} \left(\frac{V_{\text{instrut}}}{V_{\infty}} \right)^2 \quad (2.50)$$

$$C'_{D_{\text{instrut},2}} = C_{L_{\text{instrut}}} \cdot \sin(\alpha - \alpha_{\text{instrut}}) \cdot \frac{S_{\text{instrut}}}{S_{\text{duct}}} \left(\frac{V_{\text{instrut}}}{V_{\infty}} \right)^2 \quad (2.51)$$

The internal strut, because it is acting as an infinite wing, has the drag coefficient of its airfoil and no induced drag:

$$C_{D_{\text{instrut}}} = c_d \quad (2.52)$$

From Fig. 2.19, the lift and drag contributions of the internal strut's drag can be derived as:

$$C'_{D_{\text{instrut},1}} = C_{D_{\text{instrut}}} \cdot \cos(\alpha - \alpha_{\text{instrut}}) \cdot \frac{S_{\text{instrut}}}{S_{\text{duct}}} \left(\frac{V_{\text{instrut}}}{V_{\infty}} \right)^2 \quad (2.53)$$

$$C'_{L_{\text{instrut},2}} = C_{D_{\text{instrut}}} \cdot \sin(\alpha - \alpha_{\text{instrut}}) \cdot \frac{S_{\text{instrut}}}{S_{\text{duct}}} \left(\frac{V_{\text{instrut}}}{V_{\infty}} \right)^2 \quad (2.54)$$

where V_{instrut} is equal to V_{prop} or u in power off or power on conditions, respectively.

Finally, the total lift and drag contributions of the internal strut to the system then become:

$$C'_{L_{\text{instrut}}} = C'_{L_{\text{instrut},1}} + C'_{L_{\text{instrut},2}} \quad (2.55)$$

$$C'_{D_{\text{instrut}}} = C'_{D_{\text{instrut},1}} + C'_{D_{\text{instrut},2}} \quad (2.56)$$

2.2.5. EXTERNAL STRUT

The external part of the strut also contributes to the lift and drag of the system. This is illustrated in 2.20 and 2.21.

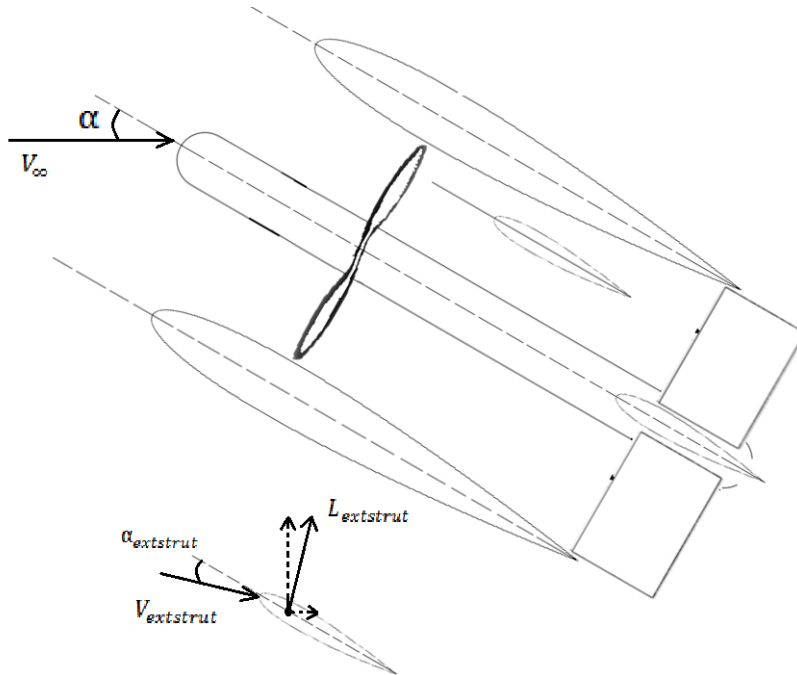


Figure 2.20: External strut lift

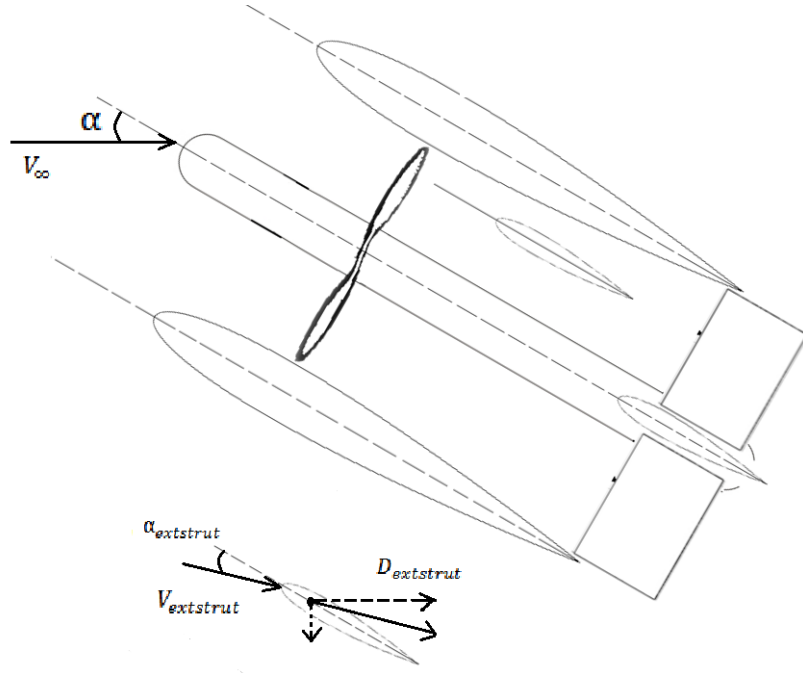


Figure 2.21: External strut drag

The external part of the strut acts in the same way as the internal part, being clamped to the duct on one side and to the fuselage on the other side, hence acting as an infinite wing. Hence, the lift curve slope of the external strut is also equal to:

$$C_{L\alpha, \text{extstrut}} = c_{l\alpha} = 2\pi \quad (2.57)$$

The lift coefficient of the external strut is then:

$$C_{L\text{extstrut}} = C_{L\alpha, \text{extstrut}} \cdot \alpha_{\text{extstrut}} \quad (2.58)$$

From this, the lift and drag contributions can be derived as follows:

$$C'_{L\text{extstrut},1} = C_{L\text{extstrut}} \cdot \cos(\alpha - \alpha_{\text{extstrut}}) \cdot \frac{S_{\text{extstrut}}}{S_{\text{duct}}} \left(\frac{V_{\text{extstrut}}}{V_{\infty}} \right)^2 \quad (2.59)$$

$$C'_{D\text{extstrut},2} = C_{L\text{extstrut}} \cdot \sin(\alpha - \alpha_{\text{extstrut}}) \cdot \frac{S_{\text{extstrut}}}{S_{\text{duct}}} \left(\frac{V_{\text{extstrut}}}{V_{\infty}} \right)^2 \quad (2.60)$$

The external strut also has the same model for the zero lift drag as the internal strut, yielding:

$$C_{D, \text{extstrut}} = c_d \quad (2.61)$$

From Fig. 2.21, the contribution to the total lift and drag can be derived as:

$$C'_{D\text{extstrut},1} = C_{D\text{extstrut}} \cdot \cos(\alpha - \alpha_{\text{extstrut}}) \cdot \frac{S_{\text{extstrut}}}{S_{\text{duct}}} \left(\frac{V_{\text{extstrut}}}{V_{\infty}} \right)^2 \quad (2.62)$$

$$C'_{L\text{extstrut},2} = C_{D\text{extstrut}} \cdot \sin(\alpha - \alpha_{\text{extstrut}}) \cdot \frac{S_{\text{extstrut}}}{S_{\text{duct}}} \left(\frac{V_{\text{extstrut}}}{V_{\infty}} \right)^2 \quad (2.63)$$

Finally, the total lift and drag contributions of the external strut to the system then become:

$$C'_{L\text{extstrut}} = C'_{L\text{extstrut},1} + C'_{L\text{extstrut},2} \quad (2.64)$$

$$C'_{D\text{extstrut}} = C'_{D\text{extstrut},1} + C'_{D\text{extstrut},2} \quad (2.65)$$

2.2.6. CONTROL SURFACES

Finally, the contribution of the control surfaces to the lift and drag of the system is illustrated in Fig. 2.22 and 2.23. Both the vertical and horizontal control surfaces are also called exit vanes. However, only the horizontal control surfaces, also called elevators, contribute to the lift when deflected, whereas the vertical control surfaces, also called rudders, contribute to the side force when deflected.

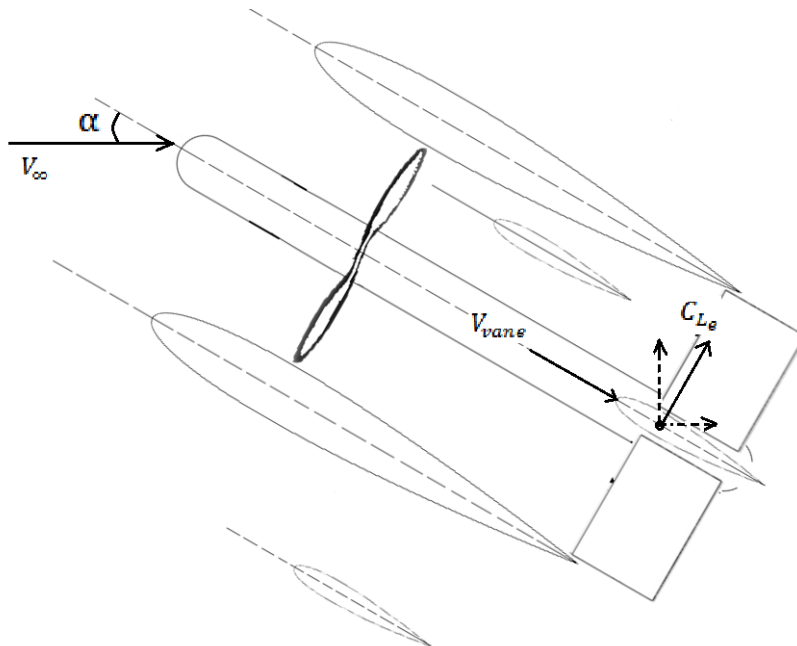


Figure 2.22: Elevator lift

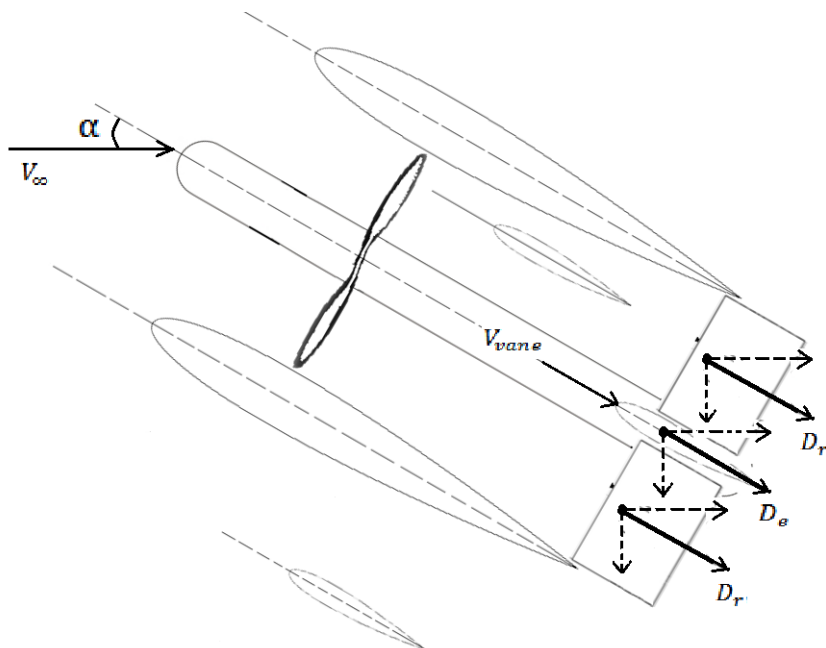


Figure 2.23: Elevator drag

ELEVATORS

The elevators are critical in providing lift for control and stability of the aircraft. Considering one separate elevator, it can be modeled as a small 3D wing, since the largest part of its chord length lies outside of the

duct. Furthermore, there is also a very small gap between the tips of the control surfaces and the inside of the duct, making it not suitable to model it as an infinite wing. The elevator effectiveness is therefore modeled by the following equation [26]:

$$C_{L\delta_e} = \frac{2\pi k AR_e}{2 + \sqrt{\frac{AR_e^2 (1-M_e^2)}{k^2} \cdot [1 + \frac{\tan^2(\Lambda_{0.5e})}{1-M_e^2}] + 4}} \quad (2.66)$$

in which AR_e is the aspect ratio of the elevator defined as:

$$AR_e = \frac{b_e^2}{S_e} \quad (2.67)$$

Furthermore, the sweep angle at the mean aerodynamic chord position $\Lambda_{0.5c}$ can also be expressed in terms of the leading edge sweep, aspect ratio and taper ratio as follows:

$$\tan(\Lambda_{0.5c}) = \tan(\Lambda_{LE}) - \frac{1}{AR} \cdot \frac{1-\lambda}{1+\lambda} \quad (2.68)$$

Finally, the factor k is dependent on aspect ratio and can be calculated by the following equations:

$$k = \begin{cases} 1 + \frac{(1.87-0.000233\Lambda_{LE})AR}{100}, & \text{if } AR \leq 4 \\ 1 + \frac{(8.2-2.3\Lambda_{LE})-(0.22-0.153\Lambda_{LE})AR}{100}, & \text{if } AR > 4 \end{cases} \quad (2.69)$$

The lift coefficient of one elevator then becomes:

$$C_{L_e} = C_{L\delta_e} \cdot \delta_e \quad (2.70)$$

From this lift coefficient, the lift and drag contributions to the complete system can be derived as:

$$C'_{L_{e1}} = C_{L_e} \cdot \cos(\alpha) \cdot n_e \frac{S_e}{S_{duct}} \left(\frac{V_{vane}}{V_\infty} \right)^2 \quad (2.71)$$

$$C'_{D_{e2}} = C_{L_e} \cdot \sin(\alpha) \cdot n_e \frac{S_e}{S_{duct}} \left(\frac{V_{vane}}{V_\infty} \right)^2 \quad (2.72)$$

where n_e is the number of elevators and V_{vane} is approximated by the continuity equation or u_1 in power off or power on conditions, respectively.

The elevator has the zero lift drag coefficient:

$$C_{D_{0,e}} = C_f f_{tc_e} f_{M_{vane}} n_e \frac{S_{wet,e}}{S_{duct}} \left(\frac{C_{d_{min}}}{0.004} \right)^{0.4} \quad (2.73)$$

The induced drag of the elevators is given by:

$$C_{D_{i,e}} = \frac{C_{L_e}^2}{\pi AR_e e} \quad (2.74)$$

so the total drag of one elevator is given by:

$$C_{D_e} = C_{D_{0,e}} + C_{D_{i,e}} \quad (2.75)$$

The lift and drag contributions to the system due to the drag of the elevators then become:

$$C'_{D_{e1}} = C_{D_e} \cdot \cos(\alpha) \cdot n_e \frac{S_e}{S_{duct}} \left(\frac{V_{vane}}{V_\infty} \right)^2 \quad (2.76)$$

$$C'_{L_{e2}} = C_{D_e} \cdot \sin(\alpha) \cdot n_e \frac{S_e}{S_{duct}} \left(\frac{V_{vane}}{V_\infty} \right)^2 \quad (2.77)$$

Finally, the total lift and drag contributions of the elevators to the system then become:

$$C'_{L_e} = C'_{L_{e1}} + C'_{L_{e2}} \quad (2.78)$$

$$C'_{D_e} = C'_{D_{e1}} + C'_{D_{e2}} \quad (2.79)$$

RUDDERS

The rudders, when not deflected, have a drag, consisting of a zero lift drag component only, which is modeled the same as that for the elevators:

$$C_{D_r} = C_{D_{0,r}} = C_f f_{t c_r} f_{M_{vane}} \frac{n_r S_{wet,r}}{S_{duct}} \left(\frac{C_{d_{min}}}{0.004} \right)^{0.4} \quad (2.80)$$

The lift and drag contributions of the rudder to the total system then become:

$$C'_{D_r} = C_{D_r} \cdot \cos(\alpha) \cdot n_r \frac{S_r}{S_{duct}} \left(\frac{V_{vane}}{V_\infty} \right)^2 \quad (2.81)$$

$$C'_{L_r} = C_{D_r} \cdot \sin(\alpha) \cdot n_r \frac{S_r}{S_{duct}} \left(\frac{V_{vane}}{V_\infty} \right)^2 \quad (2.82)$$

where n_r is the number of rudders.

2.2.7. INTERFERENCE DRAG

Besides the drag contribution of the components separately, another contribution to the system drag comes from the interference effects of components that are attached to each other or close to each other. The junctions in the ducted propeller system may be divided into the attachment of the propeller blades, the internal strut and the control surfaces to the centerbody. Also, the attachment of the internal and external strut to the duct yields interference effects. Finally, the interference effects between the propeller blades and the duct and the control surfaces and the duct contribute to the total drag as well.

PROPELLER

The propeller thus contributes to the interference drag by its attachment to the centerbody and its interference with the duct. The contribution to the total system is assumed to be negligible in power on conditions, since this drag component is assumed very small compared to the propeller thrust. However, in power off conditions it may have a significant contribution to the total drag.

From Hoerner [27] the junction of a strut with a plane wall is independent of the strut's span and can be normalized with respect to the strut's chord length, as:

$$C_{D_c} = \frac{\Delta D}{\frac{1}{2} \rho V^2} = 0.8(t/c)^3 - 0.0003 \quad (2.83)$$

The attachment of a propeller blade with the centerbody can be considered as a strut/plane wall junction. Neglecting the difference in flow direction at the junction, the interference drag in terms of the complete system is given by:

$$C_{D_{bladescb}} = (0.8(t/c)_{root,blade}^3 - 0.0003) \cdot n_{blades} \frac{c_{root,blade}^2}{S_{duct}} \left(\frac{V_{prop}}{V_\infty} \right)^2 \quad (2.84)$$

The propeller blades are not attached to the duct, since there is a small tip clearance between the tip of the propeller blades and the duct. Still, according to Hoerner, this can be modeled in the same way. Since the chord length of the blade tip is very small in comparison to the duct chord length, the interference effects between the blade tip and the duct can be modeled as that of a strut and a plane wall. Again neglecting the difference in flow direction, the interference drag is then given by:

$$C_{D_{bladescb}} = (0.8(t/c)_{tip,blade}^3 - 0.0003) \cdot n_{blades} \frac{c_{tip,blade}^2}{S_{duct}} \left(\frac{V_{prop}}{V_\infty} \right)^2 \quad (2.85)$$

INTERNAL STRUT AND EXTERNAL STRUT

The interference drag by the internal strut results from its junctions with the centerbody and the duct's inner surface. For the attachment of the internal strut with the centerbody, Hoerner's model for a strut/plane wall junction is used again, since the centerbody is straight in the chordwise direction of the strut. Therefore, neglecting the change in direction of the flow at the junction, the interference drag of the strut-centerbody junction is modeled by:

$$C_{D_{\text{strutcb}}} = (0.8(t/c)_{\text{strut}}^3 - 0.0003) \cdot \frac{n_{\text{strutcb}} c_{\text{intstrut}}^2}{S_{\text{duct}}} \left(\frac{V_{\text{intstrut}}}{V_{\infty}} \right)^2 \quad (2.86)$$

where n_{strutcb} is the number of strut/centerbody junctions.

The model for so called T-junctions, where two struts of the same chord length are joined together are given by Hoerner as:

$$C_{D_t} = \frac{\Delta D}{qt^2} = 17(t/c)^2 - 0.05 \quad (2.87)$$

Although the duct has a longer chord length than the strut, this model is used for the junction of the strut with the duct, since the duct has a curvature in the chordwise direction of the strut:

$$C_{D_{\text{strutduct}}} = (17(t/c)_{\text{strut}}^2 - 0.05) \cdot \frac{n_{\text{strutduct}} t_{\text{strut}}^2}{S_{\text{duct}}} \left(\frac{V_{\text{intstrut}}}{V_{\infty}} \right)^2 \quad (2.88)$$

where n_{strutcb} is the number of strut/duct junctions.

Similar to the internal strut, the external strut also contributes to the drag by interference drag due to the junctions with the fuselage and the duct's outer surface. For the junction of the external strut with the duct's outer surface, Eq. 2.88 can be used as well. The attachment of the strut to the fuselage can be considered the joint of a strut to a plane wall, since the fuselage is straight in the chordwise direction of the strut. Therefore the interference drag of the strut-fuselage junction is:

$$C_{D_{\text{strutfuselage}}} = (0.8(t/c)_{\text{strut}}^3 - 0.0003) \cdot \frac{c_{\text{strut}}^2}{S_{\text{duct}}} \left(\frac{V_{\text{extstrut}}}{V_{\infty}} \right)^2 \quad (2.89)$$

CONTROL SURFACES

The control surfaces have attachments to the centerbody, similar to the attachments of the internal strut and propeller blades, that can be modeled by:

$$C_{D_{\text{ecb}}} = (0.8(t/c)_e^3 - 0.0003) \cdot \frac{n_e c_e^2}{S_{\text{duct}}} \left(\frac{V_{\text{vane}}}{V_{\infty}} \right)^2 \quad (2.90)$$

and

$$C_{D_{\text{rcb}}} = (0.8(t/c)_r^3 - 0.0003) \cdot \frac{n_r c_r^2}{S_{\text{duct}}} \left(\frac{V_{\text{vane}}}{V_{\infty}} \right)^2 \quad (2.91)$$

for the elevators and rudders, respectively.

Finally, the interference effects with the duct's inner surface can be modeled in the same way, since the chord length of the control surfaces lies mostly outside of the duct, which makes the interfering part of the chord length very small compared to the duct chord. These drag contributions can thus be modeled by:

$$C_{D_{\text{educt}}} = (0.8(t/c)_e^3 - 0.0003) \cdot \frac{n_e c_e^2}{S_{\text{duct}}} \left(\frac{V_{\text{vane}}}{V_{\infty}} \right)^2 \quad (2.92)$$

and

$$C_{D_{\text{rduct}}} = (0.8(t/c)_r^3 - 0.0003) \cdot \frac{n_r c_r^2}{S_{\text{duct}}} \left(\frac{V_{\text{vane}}}{V_{\infty}} \right)^2 \quad (2.93)$$

for the elevators and rudders, respectively.

2.3. SIDE FORCE MODEL

The side force model of the ducted propeller system is very similar to the lift model, with some minor differences. This is because the ducted propellers are mostly axisymmetric. The lift model of the duct only in power on and power off conditions is similar to the lift models, with the only difference in the angle of incidence used. The effective sideslip angle β_{eff} is not the same as the freestream sideslip angle β , since the ducted propellers are subject to a sidewash effect. Also, the additional propeller side force under sideslip angles is the same as the propeller normal force under angles of attack. The lift contribution of the internal and

external strut is neglected in the side force model, since it is assumed that the effective sideslip angle of the strut is very small due to its orientation in the system. The lift and drag model of the elevators is the same for the side force model of the rudders. The drag model of the rudders in undeflected state is the same as that for the elevators in undeflected state.

2.4. NET THRUST

The net thrust of the ducted propeller system consists of the resultant of the thrust generated by the propeller and centerbody, the thrust generated by the duct and the total drag of the system. Similar to the lift model, it is assumed that the propeller and centerbody thrust remain constant over angles of attack. Furthermore, it is also assumed that the duct thrust at axial inflow conditions remains constant at angles of attack, such that it is only reduced by lift induced drag at angles of attack. This installed thrust model is illustrated by the following equation:

$$T_{c,\text{net}} = T_{c_{\text{duct},\alpha=0}} + T_{c_{\text{propcb}}} \cdot \cos(\alpha) - C_{D,\text{system}} \quad (2.94)$$

2.5. CONTROL AND STABILITY COEFFICIENTS

Considering the control and stability application of the ducted propeller system, the critical aerodynamic coefficients required to size the design for control and stability are the lift curve slope of the system C_{L_α} and the maximum lift coefficient $C_{L_{\text{max}}}$. Particularly for control, the effectiveness of the control surfaces, $C_{L_{\delta_e}}$ and $C_{Y_{\delta_r}}$, are important. To model these coefficients for power on and power off conditions for initial conceptual design, assumptions are made for safety reasons.

Considering the lift curve slope of the system first, it is clear that it has contributions from all components of the ducted propeller. However, besides the duct and propeller thrust influence, the level of effective lift contributions by the propeller normal force and internal and external strut is not known with certainty. Therefore, the strut and propeller normal force are neglected in the first estimate of the lift curve slope of the system in power on and power off conditions. The coefficient for power off conditions is then modeled by:

$$C_{L_{\alpha,\text{system,off}}} = \frac{\pi}{2} \zeta_W c_{l_\alpha} \quad (2.95)$$

And for power on conditions:

$$C_{L_{\alpha,\text{system,on}}} = \frac{\pi}{2} \zeta_W c_{l_\alpha} (1 + k_{\text{prop}}) \quad (2.96)$$

The maximum lift coefficient depends on the lift curve slope and the stall angle. In this stage, it is not possible to construct an exact relation of the stall angle as a function of geometry and operational conditions and settings. However, it is known from literature, such as [2] and [1] that the stall angle and consequently maximum lift coefficient is always higher in power on settings compared to power off settings.

Finally, the elevator and rudder effectiveness can be represented by Eq. 2.66.

2.6. NUMERICAL MODEL

In order to study design parameters for optimizing the efficiency of the ducted fan, the influence of several geometrical variations on the performance must be studied. This is heavily related to the interaction effects between duct and propeller and can be studied by aerodynamic numerical models which take into account these interaction effects. Ducted Fan Design Code (DFDC) is an open source aerodynamic tool for rapid design and analysis of ducted rotors, released under the GNU General Public License. It was developed by Mark Drela and Harold Youngren at Massachusetts Institute of Technology (MIT) and has never been completely finished, the latest version being version 0.70. Making use of a lifting line representation of the rotor blades and an axisymmetric panel method for the duct and centerbody, the interaction effects between duct and propeller are modeled. This program can thus be used to study the effect of geometrical design variables on the aerodynamic performance of a ducted propeller. Furthermore, it can be used to determine the duct thrust, corresponding to a given propeller thrust in a ducted propeller. This way, it can be used in combination with the analytical model.

2.7. ANALYSIS METHOD

The final analysis method for the ducted fan system performance consists of a combination of the analytical and numerical models. The method is outline stepwise below.

1. Determine the open propeller thrust T_{prop} of a specific propeller geometry at a specific freestream velocity V_{∞} from XROTOR or design an n-bladed open propeller for a specific thrust setting and freestream velocity in XROTOR
2. Specify the duct geometry without the propeller in DFDC and determine the inflow velocity V_{prop} at the propeller location by the continuity equation or by DFDC.
3. Determine the thrust T_{prop_2} of the same open propeller geometry for the new inflow velocity V_{prop} from XROTOR
4. Determine the thrust of the ducted propeller T_{prop_3} for the same propeller geometry by applying the inverse of the Prandtl tip loss factor
5. Specify the propeller thrust T_{prop_3} in DFDC. Now T_{duct} is obtained as well as the velocities u and u_1 .
6. Input T_{prop_3} and T_{duct} in the analytical model and determine the lift, side force, drag and installed thrust performance at angles of incidence

3

VALIDATION

In this chapter the analytical and numerical model are validated against experimental data. The numerical model is first held against experimental data from a past experiment, after which the combined numerical and analytical performance model is compared to a low speed wind tunnel experiment of a small scale model of the DUUC ducted propeller system at the Delft University of Technology.

3.1. NUMERICAL MODEL VALIDATION

The numerical model that is used in the aerodynamic performance model of the DUUC ducted propeller system, consists of DFDC and XROTOR. Unlike XROTOR, DFDC has never been validated. However, in order to utilize DFDC for aerodynamic analysis and design studies, it must be proved to be a valid tool first. Since little use has been made of DFDC, no validation cases can be found in literature. Therefore, experimental data must be compared to the outputs of the program to determine its order of accuracy and capabilities, before it is used further.

Out of all past experiments on ducted propellers, the technical report by Grunwald & Goodson [2] contains the most data concerning the complete geometry and operating conditions of the ducted propeller and the wind tunnel test, respectively. At the same time, this experiment contains a relatively simple ducted propeller model, which consists of a duct, centerbody and three-bladed propeller, without any other objects in the design. Many other technical reports lack information, such as duct geometry, propeller geometry and data on specific operating conditions, making them less suitable as a means for validation. Furthermore, this experiment is one of few which gives the thrust outputs in terms of the thrust coefficient T_c and absolute values, instead of only the propeller based thrust coefficient C_T . Finally, the experiment is also one of very few in which the propeller thrust and duct thrust are measured separately. This makes the experiment more suitable for validating DFDC and it is therefore used as a reference for validation.

3.1.1. OPERATING CONDITIONS AND GEOMETRY

All measurements in the experiment by Grunwald and Goodson were taken at sea level conditions. The density is therefore $\rho = 1.225 \text{ kg/m}^3$ and the speed of sound is 340.3 m/s . The corresponding dynamic viscosity is $\mu = 1.7894 \cdot 10^{-5} \text{ Pa}\cdot\text{s}$. The experiment only contains one point, that is measured at zero angle of attack. This point is at an advance ratio of $J = 0.595$, corresponding to a freestream velocity of $V_\infty = 100 \text{ ft/s} = 30.48 \text{ m/s}$ and a rotation frequency of $\text{RPM} = 8000$. The corresponding Reynolds number, based on the freestream velocity and duct chord, is $Re = 550,000$.

DFDC takes as input a case file, in which the freestream velocity, rotor RPM, atmospheric density, speed of sound and dynamic viscosity are specified as operating conditions, hence representing the advance ratio and atmospheric properties. Furthermore, the duct and centerbody geometry are specified in terms of absolute x and y coordinates. Finally, the rotor may be specified either as an actuator disk with a specified loading or as blade elements, given as a number of airfoil sections with their properties along the span. The rotor geometry is specified as a number of radial stations with a specified chord length and blade angle distribution.

The duct makes use of an unusual airfoil profile, of which the x and y coordinates are given exactly in the technical note. These coordinates were taken from the report and smoothed by means of CST coefficients, before being input in DFDC.

CST coefficients make use of a shape function that constructs curves from polynomials in order to make a smooth airfoil profile. These polynomials can be converted back to more x and y coordinates that represent a smoother profile than the initial x and y coordinates. The centerbody diameter is also given in the report, but the exact coordinates of the spinner part are not. Therefore, this part is approximated by an ellipse. Figure 3.2 shows a schematic of the complete test up of the experiment [2]. Based on this figure and given values of the duct diameter, propeller diameter and tip clearance, the airfoil coordinates of the duct are scaled and translated, the centerbody is scaled and the propeller location in the duct is determined. These are then input in the case file for DFDC. The geometry from the input case file, compared to the schematics from the report is shown in Fig. 3.2 and Fig. 3.3.

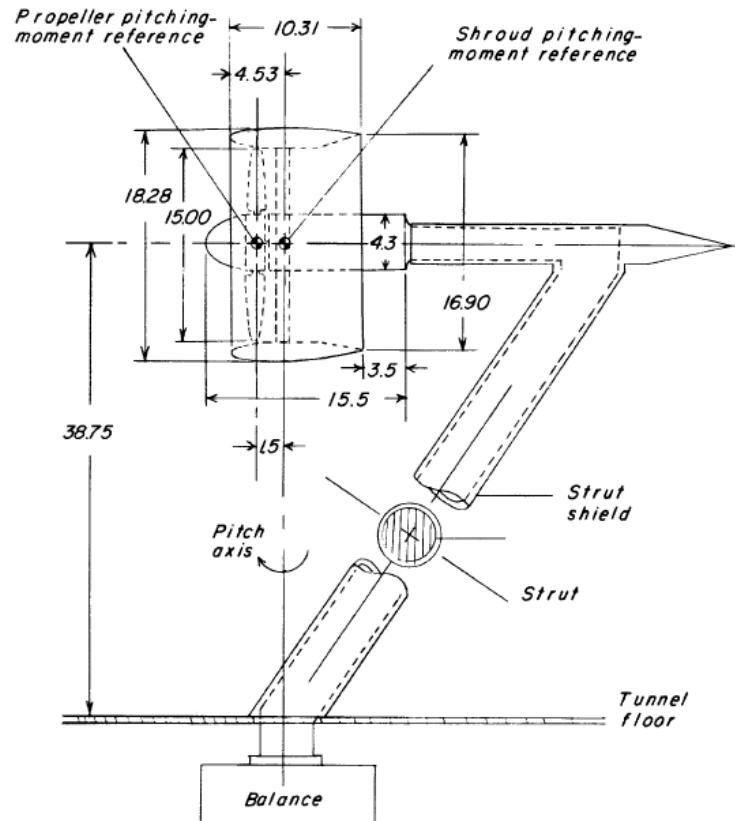


Figure 3.1: Schematics of test model Grunwald & Goodson, all dimensions in inches

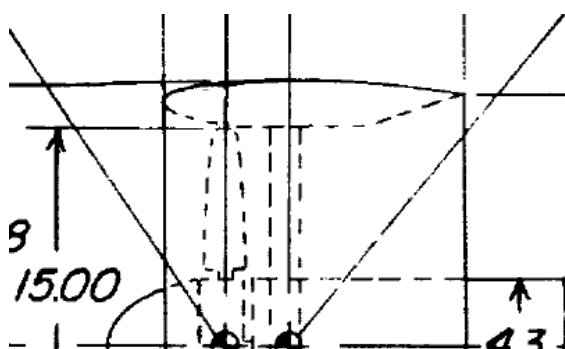


Figure 3.2: Schematics of test model by Grunwald & Goodson, all dimensions in inches

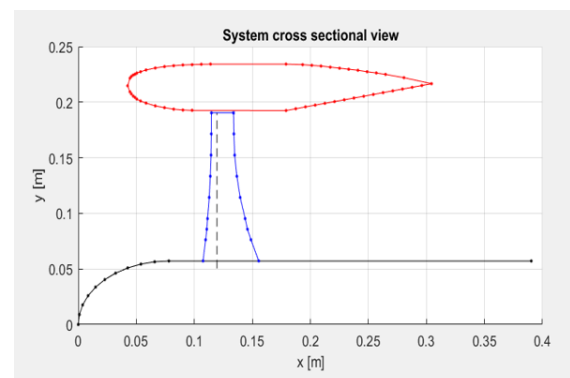


Figure 3.3: Input geometry for DFDC validation

The propeller from the experiment consists of three blades, of which the blade geometry is given in Fig. 3.4.

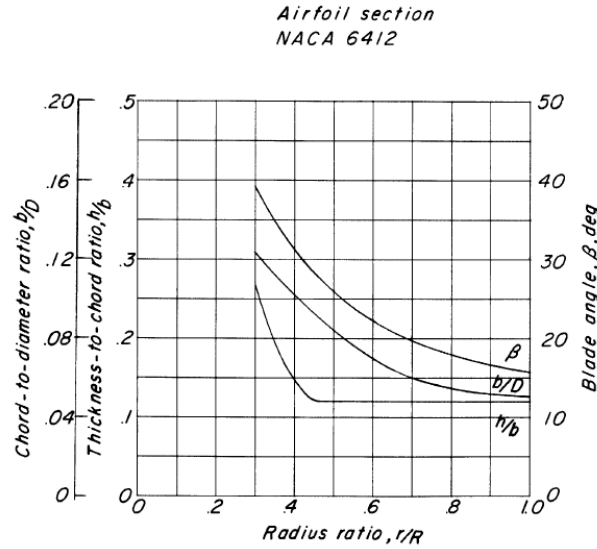


Figure 3.4: Propeller blade geometric characteristics from Grunwald and Goodson

As can be seen the blade airfoil section is given as NACA 6412, although the graph in Fig. 3.4 shows that sections from 0.3 to 0.45 of the blade span have higher thicknesses than 12 percent. Therefore, NACA 6426 and NACA 6415 sections are used for 0.3 and 0.4 of the blade span, respectively.

The case file of DFDC requires, for each blade station along the span, airfoil data to construct lift and drag polars in order to determine the thrust loading over the blade span. Interpolation between the blade sections determines the thrust loading over the entire blade. The airfoil properties required by DFDC are the following:

- α_0 , the zero lift angle of attack
- $\frac{dC_L}{d\alpha}$, the lift curve slope of the linear part of the lift curve
- $C_{L_{max}}$, the maximum lift coefficient
- $C_{L_{min}}$, the minimum lift coefficient
- $(\frac{dC_L}{d\alpha})_{stall}$ the lift curve slope at stall
- C_m , the moment coefficient
- M_{crit} , the critical Mach number
- $C_{D_{min}}$, the minimum drag coefficient
- C_L at $C_{D_{min}}$, the lift coefficient at the minimum drag coefficient
- $\frac{dC_D}{dC_L^2}$ derivative of drag with respect to the lift squared
- Re_{ref} , which is the Reynolds number at which the abovementioned parameters are specified
- f , Reynolds number scaling component, used to calculate the drag coefficient at other Reynolds numbers than the reference Reynolds number

In order to obtain these characteristics, the blade section airfoils are input in XFOIL, in which they are run for viscous flow at Mach number $M = 0$ and critical amplification factor of $n_{crit} = 0$ to simulate fully turbulent flow. The value for critical Mach number is initially chosen as 0.7 and the Reynolds number scaling component used is $f = -1.0$, which is the average value of the scaling component range $f = -0.5 - 1.5$ that holds for the low regime Reynolds number range $Re = 200,000 - 800,000$.

3.1.2. RESULTS AND COMPARISON

The results from DFDC for the geometry and operating conditions of the test in [2] are compared to the actual test results in table 3.4.

Table 3.1: Experimental vs numerical results

Outcomes	Experiment	DFDC	Offset [%]
T_{tot} [N]	90.1	65.4	-27.4
T_{propcb} [N]	64.1	52.2	-18.5
T_{duct} [N]	24.3	13.2	-45.7
Q [Nm]	4.55	3.23	-28.9
η [-]	0.71	0.73	2.7

As can be seen in the table both the propeller and centerbody thrust and the duct thrust are underestimated by DFDC. The duct thrust is underestimated by a higher degree than the propeller and centerbody thrust.

3.1.3. ERROR ANALYSIS

Considering the large offset in both propeller and centerbody thrust and duct thrust, it is interesting to investigate whether this is caused by an error in the duct and centerbody modeling or by an error in the propeller model of DFDC.

DFDC has the option to specify a value for either the total thrust or propeller thrust in order to change the propeller design accordingly. Specifying zero thrust for the propeller should give a pressure distribution of the duct similar to a situation in which the propeller is absent. This pressure distribution can then be compared to the pressure distribution around the duct from XFOIL for the same operating conditions to verify whether the duct modeling is correct.

The duct airfoil is input in XFOIL for Reynolds number $Re = 550,000$ based on the duct chord and freestream velocity. The Mach number specified is $M = 0.896$, based on the freestream velocity and sea level atmospheric conditions. The critical amplification factor n is chosen to be the standard value of 9, which holds for the average wind tunnel.

The comparison between the pressure distribution on the duct only from DFDC and XFOIL is shown in Fig. 3.5.

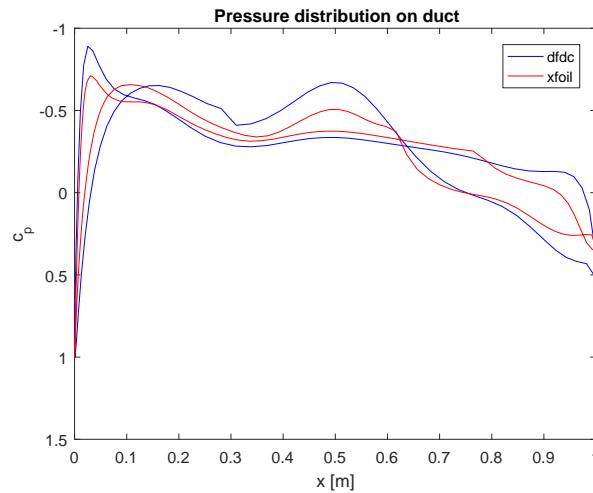


Figure 3.5: Duct pressure distribution from DFDC and XFOIL

As can be seen, the curves differ slightly, which may be due to the presence of the centerbody and possibly due to differences in modeling, such as a difference in amplification factor or difference in paneling. However, the curves follow the same trends and have on average the same c_p values. The drag of the duct in these zero propeller thrust settings can also be compared to the measured drag from Grunwald and Goodson. The comparison is shown in table below:

Table 3.2: Experimental vs numerical results

Outcomes	Experiment	DFDC	Offset [%]
$D_{\text{duct}} [N]$	3.12	3.18	1.9

As can be seen, the drag of the duct from DFDC matches very well with the experimental value. Hence, since the duct modeling in DFDC corresponds very well to both XFOIL and the experiment, it may be concluded that the modeling of the duct aerodynamics in DFDC can not be the cause for the erroneous modeling of the thrust.

To assess the propeller model in DFDC, comparisons to XROTOR can be made. XROTOR is an aerodynamic tool from the same developers of DFDC for the analysis of open rotors, with limited capabilities of ducts, which has successfully been validated and used much more often, contrary to DFDC. As a comparison, the same propeller geometry is loaded into XROTOR and analyzed for an inflow velocity similar to the inflow velocity that the ducted propeller sees in DFDC. The total thrust output from XROTOR and DFDC can then be compared to gain more insight in DFDC's propeller modeling.

In order to determine the inflow velocity that should be input in XROTOR, the velocity at the propeller position for a zero propeller thrust setting is obtained from DFDC, which is the flow velocity that includes the induced velocity by the duct. The spanwise variation of velocity at the propeller location, in absence of the propeller is given in Tab. 3.4, taken from DFDC.

Table 3.3: Spanwise propeller inflow velocity from DFDC

$r [m]$	$V_x [m/s]$
0.06406	33.89
0.08082	34.44
0.09758	34.76
0.1143	34.89
0.1311	35.03
0.1479	35.38
0.1646	36.30
0.1814	37.15

The average velocity of the spanwise distribution of the inflow velocity from DFDC is chosen as an input in XROTOR, which is $V_{\text{prop}} = 35.23$ m/s. Keeping the same RPM of the propeller, the advance ratio is changed according to the new freestream velocity. Furthermore specifying the exact same airfoil sections and propeller blade geometry, the following results are obtained for the thrust and torque of the propeller:

Table 3.4: Numerical results XROTOR

Outcomes XROTOR	Value
T_{prop}	60.6 N
Q	4.41

The propeller thrust and torque from XROTOR are 60.6 N and 4.41 Nm, respectively, which are much higher than the values from DFDC. It is also slightly lower the combined propeller and centerbody thrust from the technical report by Grunwald and Goodson, indicating that this difference is likely due to the absence of the centerbody and duct.

Comparing the outputs by DFDC and XROTOR, it can be concluded that the propeller model in DFDC does not work properly and must be the cause for the erroneous modeling of the ducted fan. It should then be investigated whether DFDC is still a valid tool for predicting trends in ducted fan performance when design changes are made.

Assuming that the duct aerodynamics are modeled properly in DFDC and that only the propeller model is erroneous, it is likely that the influence of the propeller thrust on the duct is modeled right, since the pressure jump corresponding to a particular propeller thrust is taken into account in the duct pressure distribution and corresponding duct thrust.

One way to investigate the correctness of the propeller influence on the duct is to change the propeller and centerbody thrust manually to the experimental value for the same duct geometry. It can be seen that

DFDC changes the propeller thrust by changing the blade angle distribution by a constant increase over the span.

Table 3.5 shows the new values of the duct and propeller thrust from DFDC vs the experimental values from the technical report.

Table 3.5: Experimental vs numerical results DFDC

Outcomes	Experiment	DFDC	Offset [%]
T_{tot} [N]	90.1	91.4	1.48
T_{prop} [N]	64.1	64.1	0
T_{duct} [N]	24.29	22.3	12.68
Q [Nm]	4.546	4.63	1.85
η [N/W]	0.71	0.71	0

As can be seen the prediction of the thrust by DFDC is now much closer to the experimental value, with very small deviations of total thrust and propeller torque. Only duct thrust is overestimated by 13 percent.

Based on these results it can be concluded that with a correct specified propeller thrust, the influence of the propeller on the duct aerodynamics are modeled reasonably well, such that the pressure distribution and thrust of the duct are estimated properly.

Next, it is investigated whether from this specified thrust setting, DFDC is able to predict the changes in thrust with changes in operating conditions and power settings. For this Fig. 3.6 from the technical report is used, in which the variation of lift and thrust with angle of attack are given for several advance ratios.

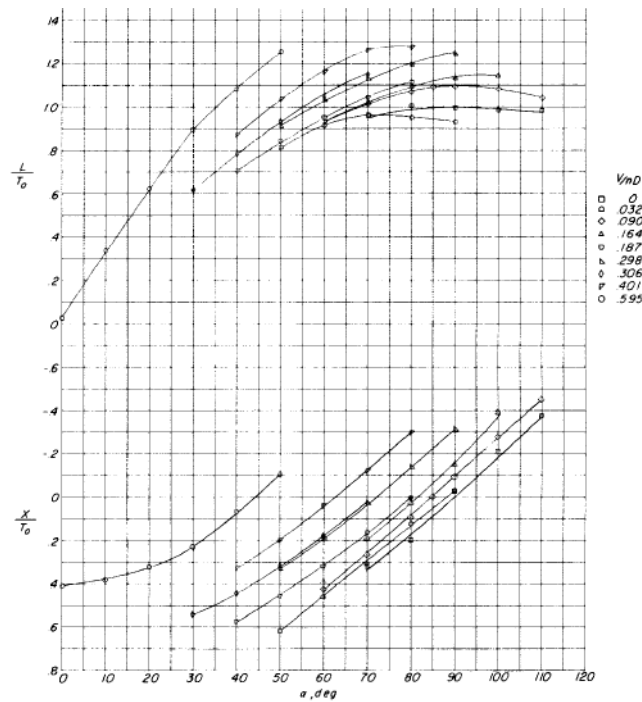


Figure 3.6: Variation of lift and thrust with angle of attack for several advance ratios

Since measurements for axial inflow have been done at one advance ratio only, the curves for the other advance ratios start at higher angles of attack. Still it can be observed that all curves follow more or less the same trends, both for the lift and axial force curves. It can be seen that the slope slightly increases with the onset of stall when comparing the lift and axial force curve of advance ratio $J = 0.595$. Comparing the different curves to each other in their unstalled regimes, it may be assumed that the curves are identical and only translated upwards for increasing advance ratio. Extrapolating all curves this way to zero angle of attack, the predicted values for thrust are obtained. Since the RPM is kept constant in the experiment, the different advance ratios are based on variations in freestream velocity. Changing the freestream velocity in DFDC allows for comparing the thrust values. These are given in table 3.6.

Table 3.6: Extrapolated values of $\frac{X}{T_0}$

J	$\frac{X}{T_0}$	T [N]	DFDC	Offset [%]
0.401	0.6	120	120	0
0.306	0.72	144	136	-5.6
0.298	0.7325	146.6	137	-6.5
0.187	0.8575	171.4	159	-7.2
0.164	0.8825	176.7	164	-7.2
0.090	0.9575	191.7	182	-5.1
0.032	1.0250	205.2	198	-3.5
0	1.1	220.2	208	-5.6

As can be seen DFDC models the trends in total thrust very well, with deviations of maximum 10 percent. It can therefore be concluded that DFDC is able to predict variations in thrust with changing operating conditions accurately.

3.2. ANALYTICAL MODEL VALIDATION

Having validated DFDC to an extent at which it can be used in combination with the analytical model for pre specified thrust inputs, the total performance model must be validated against experimental data. This was done in a low speed wind tunnel test at the Delft University of Technology.

3.2.1. EXPERIMENTAL SET UP AND TEST CONDITIONS DUUC WIND TUNNEL TEST

MODEL GEOMETRY

The DUUC ducted propeller system has been built into a small scale model by Nando van Arnhem at the Delft University of Technology. The model consists of a duct that is made of styrofoam, but has a very smooth surface. Furthermore, it contains a small model three-bladed propeller, a strut with an internal and external part and two horizontal and vertical control surfaces, attached to the centerbody at the trailing edge of the duct. This model is based on the first design of the DUUC propeller system. The dimensions of the scale model geometry are outlined below:

Duct

- Airfoil: NACA0012
- Diameter: 0.25 m
- Chord length: 0.125 m
- Aspect ratio: 2

Centerbody

- Length: 0.2 m
- Diameter: 0.05 m
- Shape: cylindrical with elliptical cone at leading and trailing edge

Propeller

- Number of blades: three
- Diameter: 0.24 m
- Blade airfoil sections: unknown
- Blade geometry: unknown

Internal strut

- Airfoil: NACA0012
- Chord length: 0.06 m
- Span: two times 0.09 m

External strut

- Airfoil: NACA0012
- Chord length: 0.06 m
- Span: 0.09 m

Elevators

- Number of elevators per duct: two
- Airfoil: NACA0012
- Chord length: 0.048 m
- Span: 0.096 m
- Aspect ratio: 2

Rudders

- Number of elevators per duct: two
- Airfoil: NACA0012
- Chord length: 0.048 m
- Span: 0.096 m
- Aspect ratio: 2

This model was tested in the low speed wind tunnel of the Delft University of Technology. The scale model in the test section is shown in Fig. 3.7 and 3.8.



Figure 3.7: Geometric view of the DUUC model mounted in the test section



Figure 3.8: Front view of the DUUC model mounted in the test section

INSTRUMENTATION AND MEASUREMENTS

Measurements of the total forces on the system were recorded at various operating conditions, including various flow velocities, power settings, angles of incidence and control surface deflections. The model was mounted upside down in the test section of the wind tunnel, attached to a strut, which was connected to a six component balance, measuring the forces in x,y and z direction.

A simplified representation of the test set up is shown in Fig. 3.10, 3.9, 3.10 and 3.11.

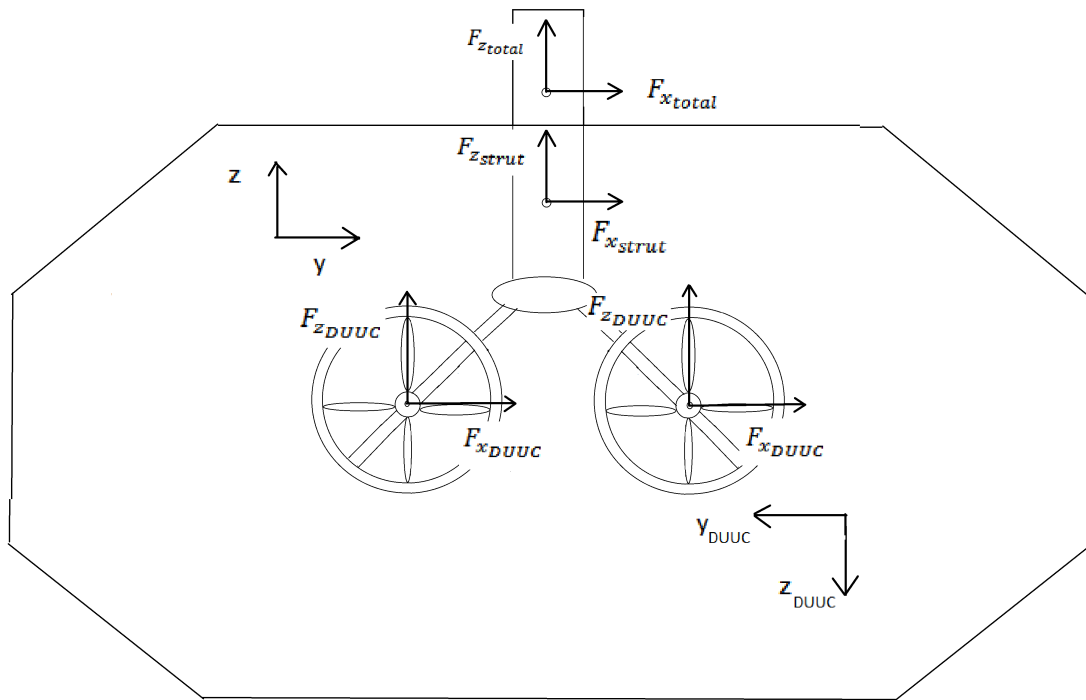


Figure 3.9: Schematic front view of the DUUC ducted propeller scale model in the test section

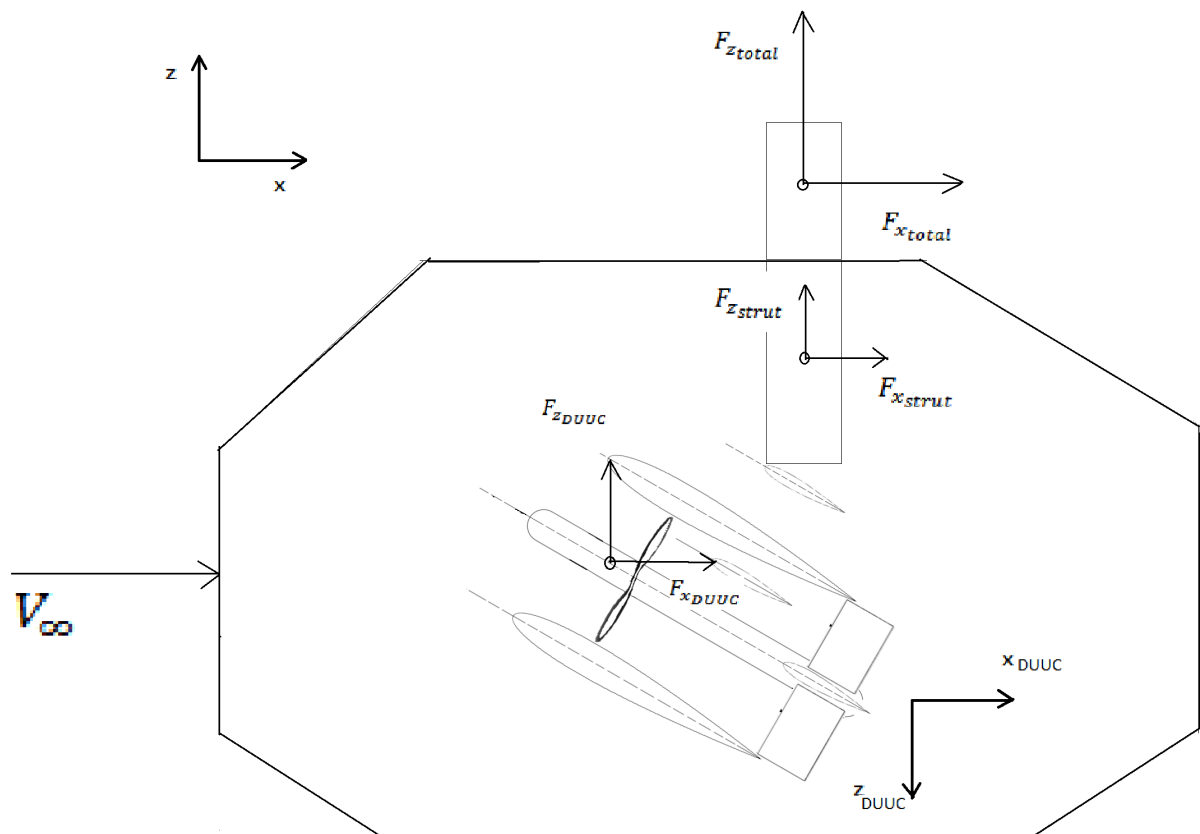


Figure 3.10: Schematic side view of the DUUC ducted propeller scale model in the test section

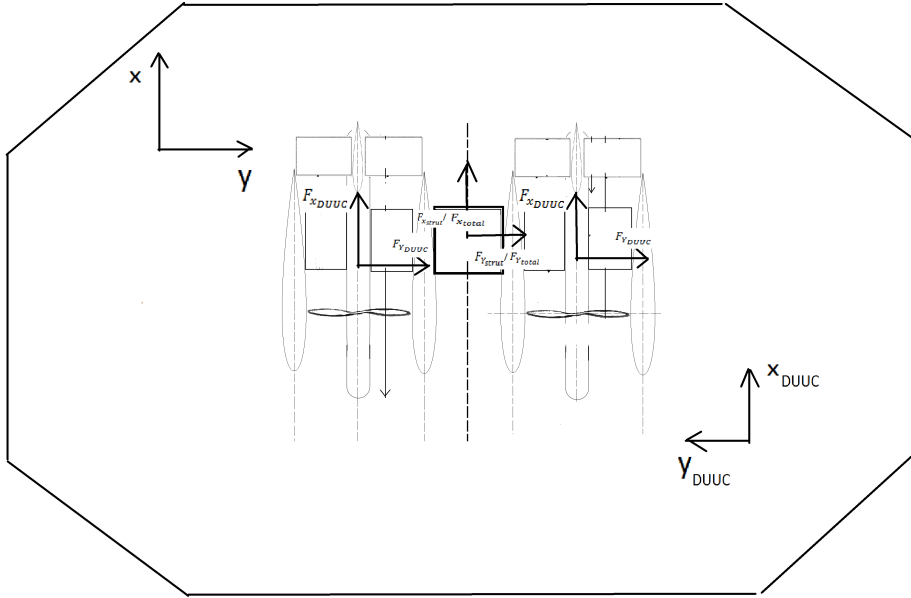


Figure 3.11: Schematic top view of the DUUC ducted propeller scale model in the test section

It can be seen that the balance measures the forces of the complete system in x,y and z direction. The complete system consists of the ducted propeller system and the strut. Thus, the strut forces must be subtracted from the total measured forces to obtain the ducted propeller system forces. Therefore, measurements were also done on the strut only, with the ducted propeller system removed, under the same operating conditions.

Since the ducted propeller system was mounted upside down and the positive direction for axial force was set to the flow direction, the lift, side force, net thrust and drag coefficients are determined from the measurements as follows:

$$C_{L_{DUUC}} = \frac{-(F_{z_{tot}} - F_{z_{strut}})}{\frac{1}{2}\rho V_{\infty}^2 2S_{duct}} \quad (3.1)$$

$$C_{Y_{DUUC}} = \frac{-(F_{y_{tot}} - F_{y_{strut}})}{\frac{1}{2}\rho V_{\infty}^2 2S_{duct}} \quad (3.2)$$

$$C_{x_{DUUC}} = \frac{-(F_{x_{tot}} - F_{x_{strut}})}{\frac{1}{2}\rho V_{\infty}^2 2S_{duct}} \quad (3.3)$$

$$C_{D_{DUUC}} = \frac{(F_{x_{tot}} - F_{x_{strut}})}{\frac{1}{2}\rho V_{\infty}^2 2S_{duct}} \quad (3.4)$$

TEST SETTINGS

The tunnel speed was varied at three settings, $V = 0$ m/s, $V = 10$ m/s and $V = 20$ m/s. The RPM was varied between 6000 and 9000 for free stream velocities and static conditions including control surface deflections. For static conditions without control surface deflections the RPM was varied from 3000 till 9000 for static conditions. Angles of attack were varied between -5 and 20 degrees and sideslip angles were varied from 0 to 20 degrees. Elevator and rudder deflections were varied between -40 and 40 degrees. Elevators and rudders were deflected simultaneously as well. Finally, one engine inoperative (OEI) conditions were tested.

Thus, measurements of the lift, side force, drag and net thrust under angles of attack and angles of sideslip, including various control surface deflections have been recorded on the DUUC ducted propeller scale model under four advance ratios: $J = 0$, $J = 0.28$, $J = 0.42$, $J = 0.56$ and $J = 0.83$.

Measured data were compared to outcomes of the aerodynamic performance model, described in chapter 2. Since the propeller geometry is unknown, a downscaled version of the geometry of the propeller from Grunwald and Goodson is used in the analysis, since this propeller was used successfully in the validation of the numerical model and is also a three-bladed propeller.

3.2.2. RESULTS AND COMPARISON

NET STATIC THRUST AT VARIOUS POWER SETTINGS

The first set of wind tunnel measurements that is compared to the aerodynamic performance model is the set of static conditions. Installed thrust or net axial force was measured on the ducted propeller system for a range of RPM settings. At RPM settings of 6000 and 9000, elevator and rudder deflections were tested as well. Taking the open propeller static thrust values as a base and using them as inputs in the performance model, the installed thrust from the model and the test are compared. Comparison for static installed thrust over the range of tested RPM settings is shown in Fig.

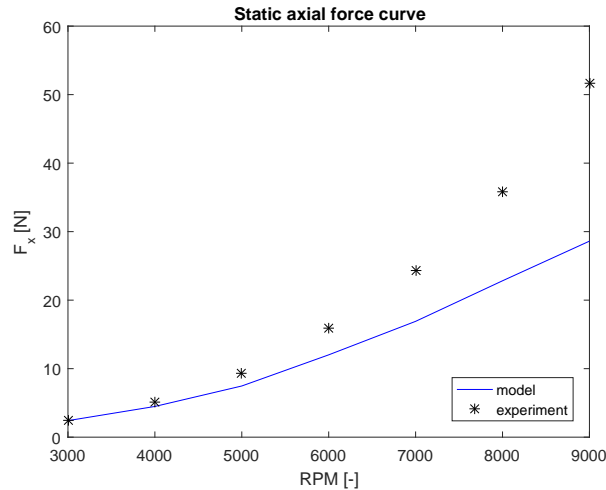


Figure 3.12: Static installed thrust, model vs experiment

It can be seen that the static thrust is modeled properly at an RPM setting of 2000, but is increasingly underestimated at higher RPM settings. Having validated the duct thrust output of the numerical model at a specified propeller thrust, the deficiency in thrust can either be attributed to an erroneous Prandtl tip loss factor, such that the propeller thrust is underestimated, or to an overestimation of the total drag of the system. In case the drag is not significantly overestimated, the tip loss reduction of the duct may become more efficient at higher power settings.

Considering the static conditions with elevator deflections, the model to experiment comparison of the lift with respect to elevator deflections for RPM 6000 and 9000 are shown in Fig. 3.13 and 3.14.

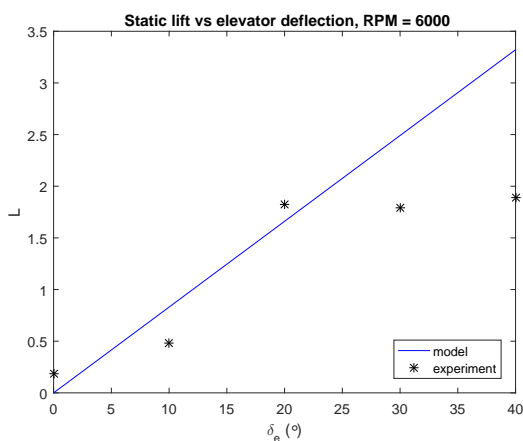


Figure 3.13: Lift vs elevator deflections at RPM = 6000, model vs experiment

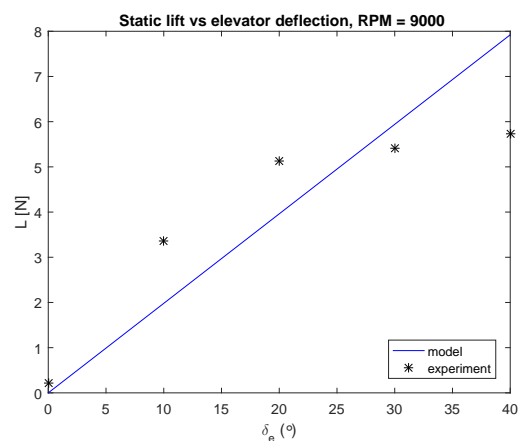


Figure 3.14: Static side force vs rudder deflections at RPM = 9000, model vs experiment

As can be seen, for RPM 6000 the measurement points of lift are near the model line until $\delta_e = 20^\circ$, indicating proper modeling of the elevators. At elevator deflections of $\delta_e = 30^\circ$ and $\delta_e = 40^\circ$, the lift is significantly lower

compared to the model line and is approximately equal to the value at $\delta_e = 20^\circ$, which indicates that the elevators have completely stalled here. It may be concluded that the onset of stall starts between $\delta_e = 20^\circ$ and $\delta_e = 30^\circ$ and that complete stall is reached in this region as well. For RPM 9000, the trend in measured data also follows the trend of the model line. However, deviations are slightly higher than at RPM 6000 and are all above the model line. This may indicate an underestimation of the lift slope of the elevators. Similar to the case at RPM 6000, the lift remains approximately constant after $\delta_e = 20^\circ$, indicating complete stall of the control surfaces.

The installed thrust with respect to elevator deflections for RPM 6000 and RPM 9000 is compared for model and experiment in Fig. 3.15 and 3.16.

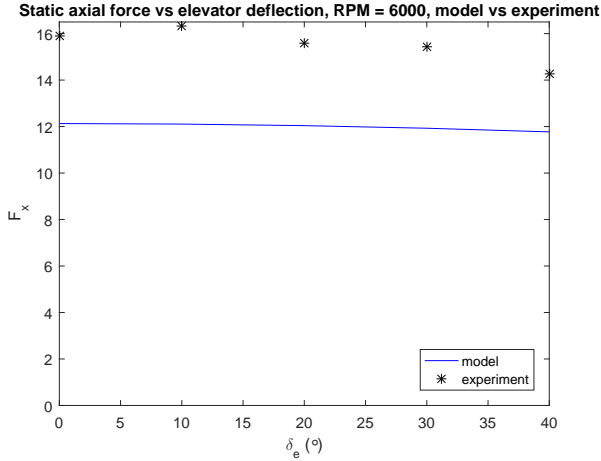


Figure 3.15: Installed thrust vs elevator deflections at RPM = 6000, model vs experiment

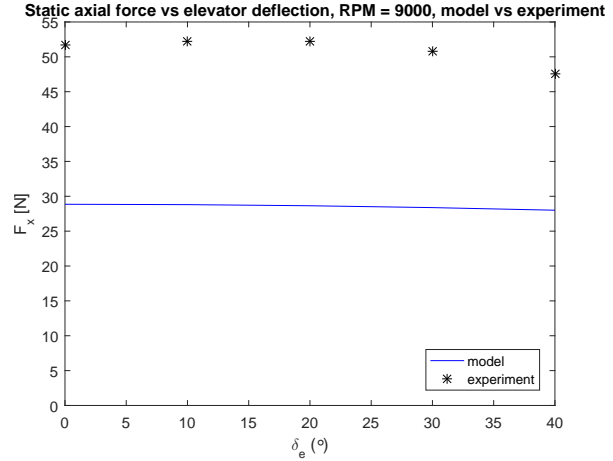


Figure 3.16: Installed thrust vs rudder deflections at RPM = 9000, model vs experiment

As could be seen in Fig. 3.12, the installed static thrust underestimated by the model at RPM 6000. It can be seen in Fig. 3.15, that the reduction in installed thrust due to elevator deflections is negligible according to the model. This trend corresponds well to the measurements, which also show very small variations in installed thrust from $\delta_e = 0^\circ$ until $\delta_e = 30^\circ$. This may indicate that the induced drag due to elevators is very low in static conditions. Only between $\delta_e = 30^\circ$ and $\delta_e = 40^\circ$ the thrust decreases slightly more, which may be attributed to a higher stall of the elevators. The axial force at RPM 9000 is more heavily underestimated than at 6000 RPM, as could already be seen in Fig. 3.12. The model trend also shows a negligibly small decrease in installed thrust due to elevator deflections here. The measurement data again correspond to this trend, showing even smaller deviations in the measurements between $\delta_e = 0^\circ$ and $\delta_e = 20^\circ$. Only between $\delta_e = 20^\circ$ and $\delta_e = 30^\circ$ the measurements show a slightly higher reduction in installed thrust, which then decreases more between $\delta_e = 30^\circ$ and $\delta_e = 40^\circ$, indicating higher drag due to higher levels of stall.

Comparisons of the static side force versus rudder deflections at RPM 6000 and RPM 9000 are shown in Fig. 3.17 and 3.18.

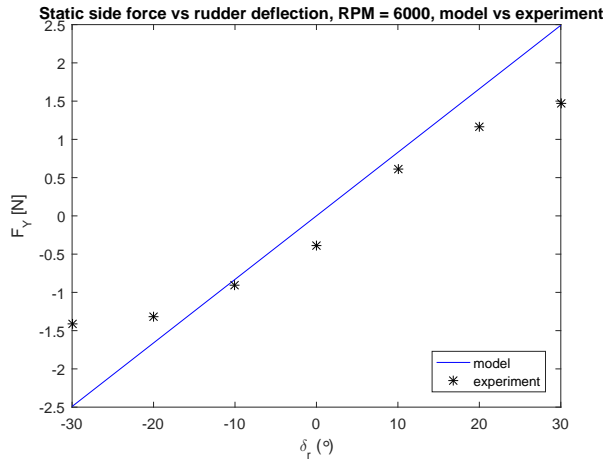


Figure 3.17: Static side force vs rudder deflections at RPM = 6000, model vs experiment

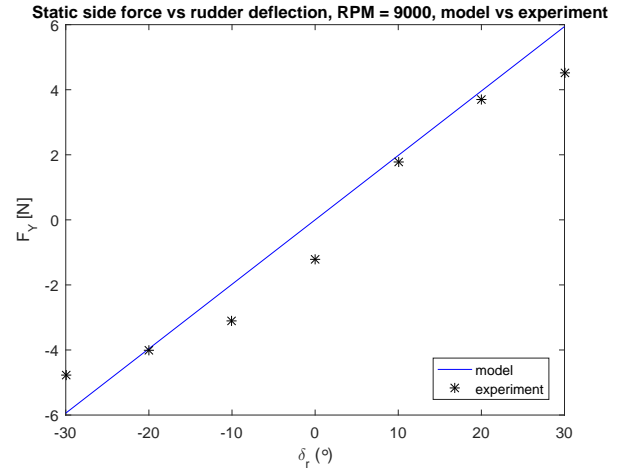


Figure 3.18: Static side force vs rudder deflections at RPM = 9000, model vs experiment

Considering the static side force plot for RPM 6000, the measurement points are not deviating significantly from the model line in the unstalled regime of the rudders, indicating proper modeling of the rudders. Since the same model is used for the rudders and the elevators, the measurement data also indicate that the rudders and elevators behave similarly in static conditions. The deviation of the experimental data from the model becomes significant at $\delta_r = -30^\circ$ and $\delta_r = 30^\circ$, again indicating higher levels of stall and therefore significant decrease in rudder effectiveness. Similar to the case of elevator deflections, it appears that the onset stall begins between $\delta_r = 20^\circ$ and $\delta_r = 30^\circ$. For RPM 9000, the same trends can be seen as for RPM 6000. Only in this case, also higher deviations are observed at $\delta_r = 0^\circ$ and $\delta_r = -10^\circ$. This may be attributed to flow irregularities due to unknown disturbances or defects in the scale model.

Finally, the comparisons of installed thrust versus rudder deflections are shown in Fig. 3.19 and 3.20 for RPM 6000 and RPM 9000.

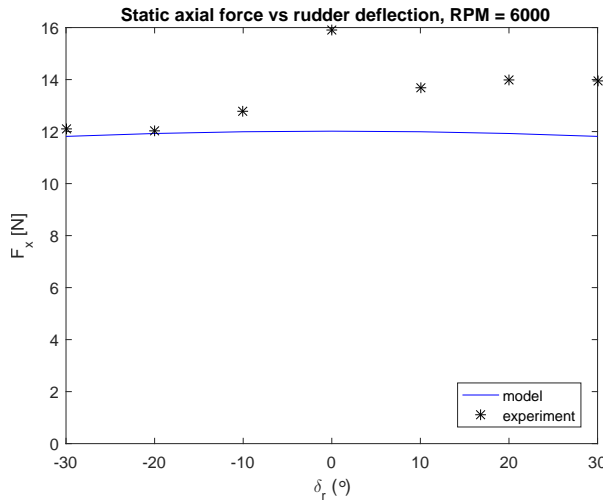


Figure 3.19: Installed thrust vs rudder deflections at RPM = 6000, model vs experiment

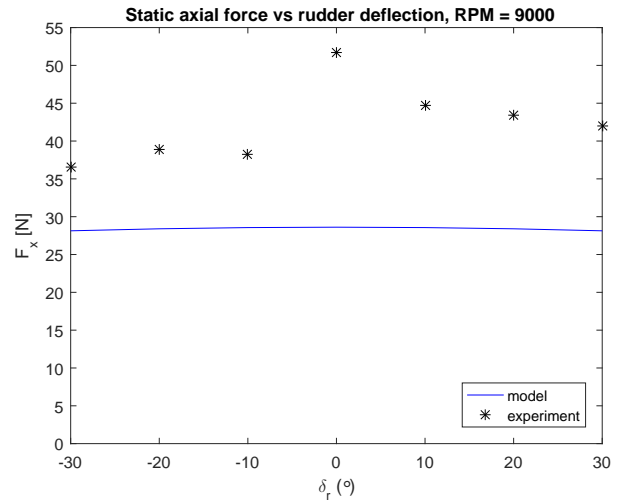


Figure 3.20: Installed thrust vs rudder deflections at RPM = 9000, model vs experiment

At RPM 6000, the decrease in installed thrust is significantly higher at rudder deflections of $\delta_r = 10^\circ$ and $\delta_r = -10^\circ$. Variations in installed thrust are then very low between $\delta_r = -10^\circ$ and $\delta_r = -30^\circ$ and between $\delta_r = 10^\circ$ and $\delta_r = 30^\circ$. The same trends can be observed for RPM 9000. Both for RPM 6000 and RPM 9000, it can also be seen that the decrease in thrust is slightly higher for negative rudder deflections compared to positive rudder deflections. This indicates higher drag as a consequence of rudder deflections, both in the unstalled and stalled regime, as compared to elevator deflections. Since the mounting of the elevators and rudders in the model is the same, it is surprising that the rudders have a significantly higher drag contribution

than the elevators. This may not easily be attributed to interference effects since the trailing edge of the model is axisymmetric. However, the rudders may experience higher levels of disturbed flow than the elevators, possibly due to the swirl characteristics of the slipstream or the presence of the internal strut.

Finally, measurements have been done at static conditions with the elevators and rudders deflected simultaneously. The plots for the variation of static lift versus elevator deflections at various rudder deflections are given in Fig. 3.21 and 3.22.

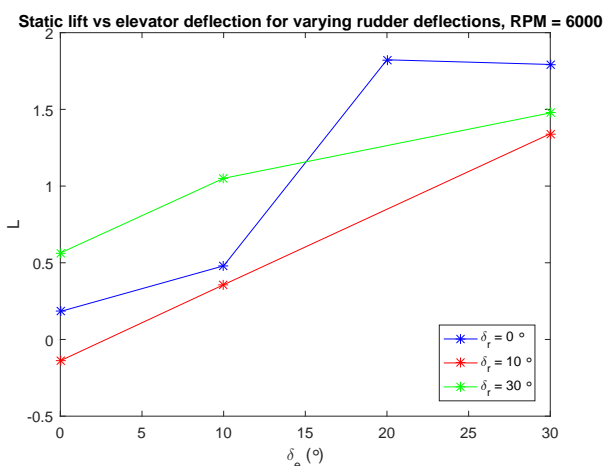


Figure 3.21: Static lift force vs elevator deflections at various rudder deflections, RPM = 6000

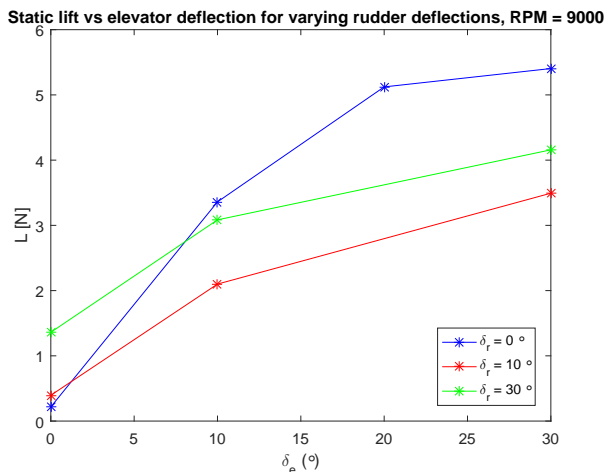


Figure 3.22: Static side force vs rudder deflections at RPM = 9000, model vs experiment

Since measurements with simultaneous elevator and rudder deflections were not taken at $\delta_e = 20^\circ$, the rate of lift increase in the unstalled regime of the elevators can only be compared for $\delta_e = 0^\circ$ until $\delta_e = 10^\circ$. For RPM 6000, the slope in this region slightly increases, which may indicate increased effectiveness of the elevators when rudders are also deflected, possibly due to higher effective velocities by the addition of supervelocities. However, for RPM 9000, the slope of the lift decreases between $\delta_r = 0^\circ$ and $\delta_r = 10^\circ$, which may indicate that at RPM 9000, the effectiveness of the elevators decrease when rudders are deflected simultaneously, possibly due to higher disturbances in effective flow over the elevators because of interference effects. However, a limited set of measurement data and no detailed knowledge on the flow phenomena makes it difficult to be certain about this.

The plots for installed thrust versus elevator deflections at various rudder deflections are shown in Fig.

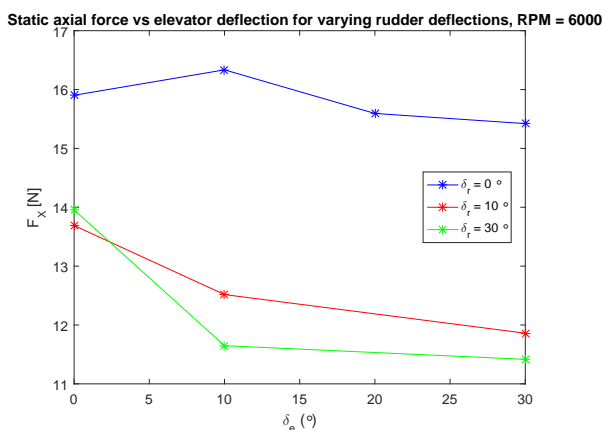


Figure 3.23: Installed thrust vs elevator deflections at various rudder deflections, RPM = 6000

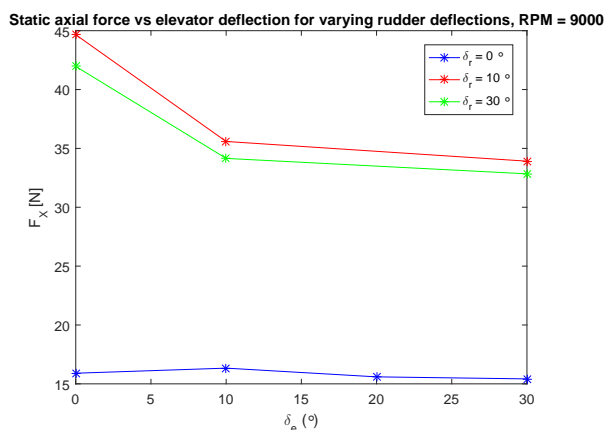


Figure 3.24: Installed thrust vs rudder deflections at RPM = 9000, model vs experiment

The plots of the static side force versus rudder deflections for varying elevator deflections are given in Fig. 3.25 and 3.26.

Static side force vs rudder deflection for varying elevator deflections, RPM = 6000

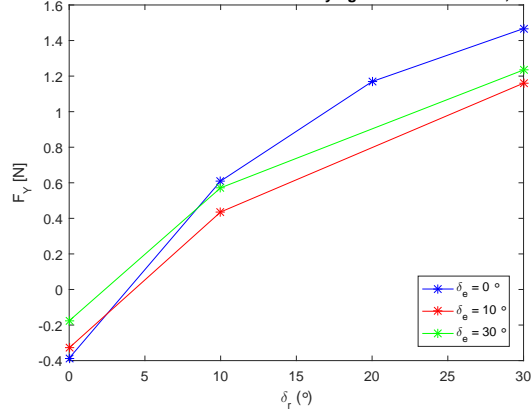


Figure 3.25: Static lift force vs elevator deflections at various rudder deflections, RPM = 6000

Static side force vs rudder deflection for varying elevator deflections, RPM = 9000

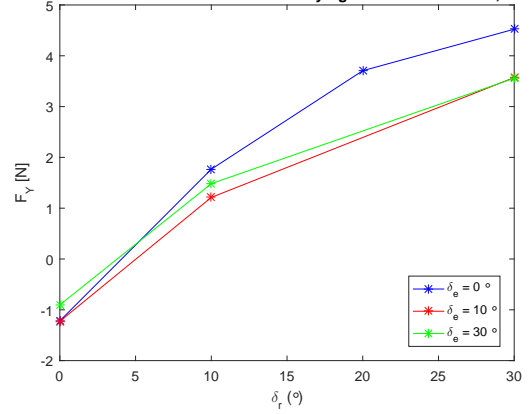


Figure 3.26: Static side force vs rudder deflections at RPM = 9000, model vs experiment

The net thrust versus rudder deflections for various elevator deflections are given for RPM 6000 and 9000 in Fig. 3.27 and 3.28.

Static axial force vs rudder deflection for varying elevator deflections, RPM = 6000

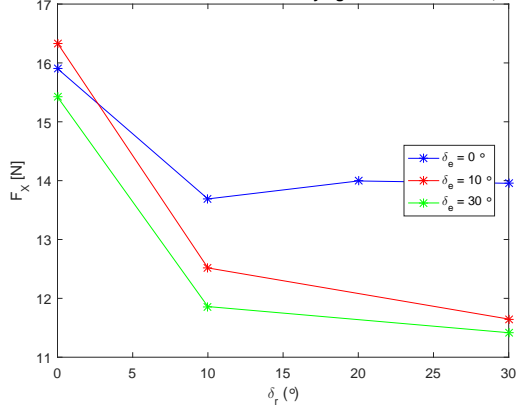


Figure 3.27: Installed thrust vs elevator deflections at various rudder deflections, RPM = 6000

Static axial force vs rudder deflection for varying elevator deflections, RPM = 9000

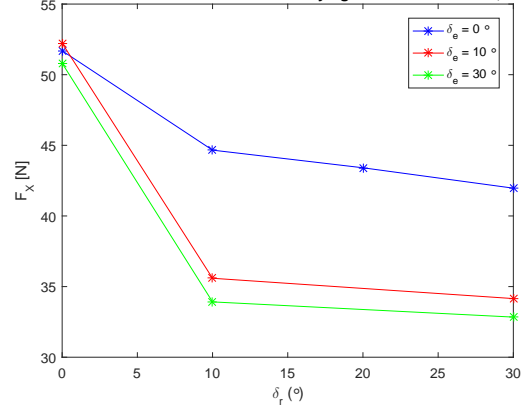


Figure 3.28: Installed thrust vs rudder deflections at RPM = 9000, model vs experiment

POWER OFF CONDITIONS

The first set of wind tunnel measurements that is compared to the analytical model is the power off condition. The propeller of the scale model was taped to the duct by means of stickers in order to prevent it from windmilling. The lift and drag polar of the analytical model and measurements are shown in Fig. 3.29 and 3.30, respectively.

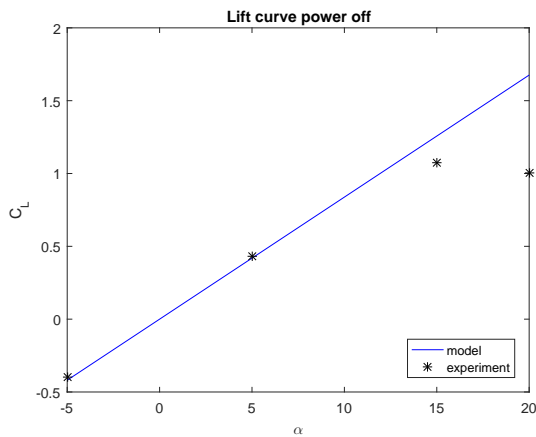


Figure 3.29: Lift curve propeller off condition, analytical vs experimental

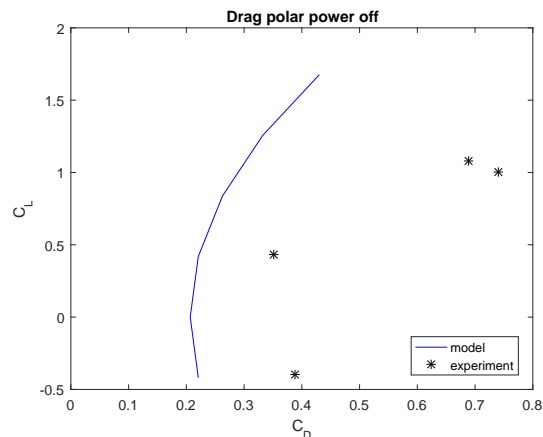


Figure 3.30: Drag polar propeller off condition, analytical vs experimental

As can be seen the lift model corresponds very well to the measurements. It seems as if the duct is the only component generating lift, such that the lift contribution of the internal and external strut are negligible. The lift component of the strut will therefore not be used in the comparison of the model to power on conditions, since it is likely that, if the strut does not significantly contribute to the lift in power off conditions, the same will be true for power on conditions, since the strut is then subject to a higher level of flow disturbance, downstream of the propeller. The drag is significantly underestimated by the propeller off drag model and is measured almost twice as high compared to the predictions. This may be attributed to the propeller of the scale model, which does not represent a real propeller in feather conditions, but could rather be modeled as a sum of flat plates normal to the flow direction, yielding higher levels of flow separation and therefore higher drag. Furthermore, interference effects may be underestimated by the model as well. Since the model uses methods by [27] for interference drag, Reynolds number effects may lead to large deviations of this drag, since the wind tunnel experiment was done at a significantly lower Reynolds number due to the small scale model and low speeds, compared to transport aircraft, for which the interference drag model is specified.

POWER ON AND FREESTREAM FLOW CONDITIONS

Next, the analytical model is compared to the measurements at the four advance ratios $J = 0.42$, $J = 0.28$, $J = 0.83$ and $J = 0.56$, corresponding to $V_\infty = 10\text{m/s}$, $V_\infty = 20\text{m/s}$ and $RPM = 6000$ and $RPM = 9000$.

First, the lift curves are compared. No measurements under angles of attack were done at the third advance ratio $J = 0.83$. For the fourth advance ratio $J = 0.56$, only one angle of attack was measured. Comparisons of the lift curves at advance ratios $J = 0.42$ and $J = 0.28$ are shown in Fig. 3.31, 3.32 and 3.33.

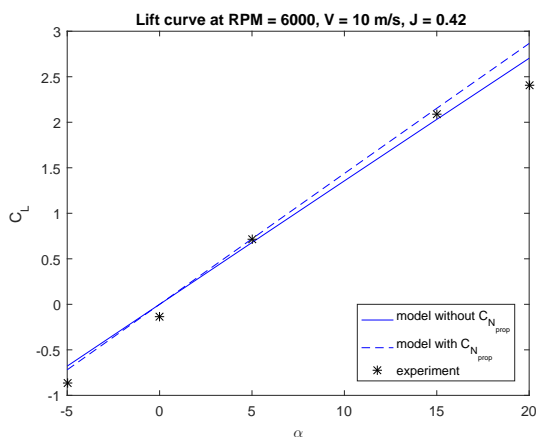


Figure 3.31: Lift curve at $J = 0.42$, analytical vs experimental

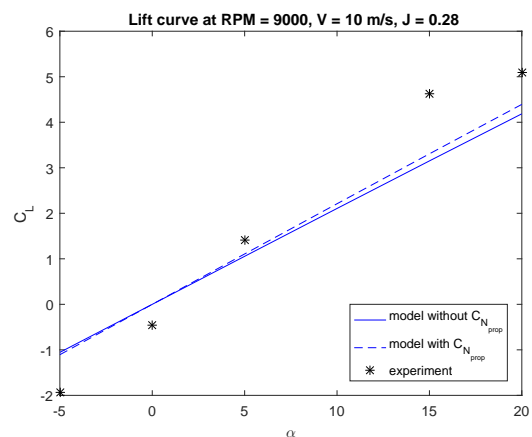


Figure 3.32: Lift curve at $J = 0.28$, analytical vs experimental

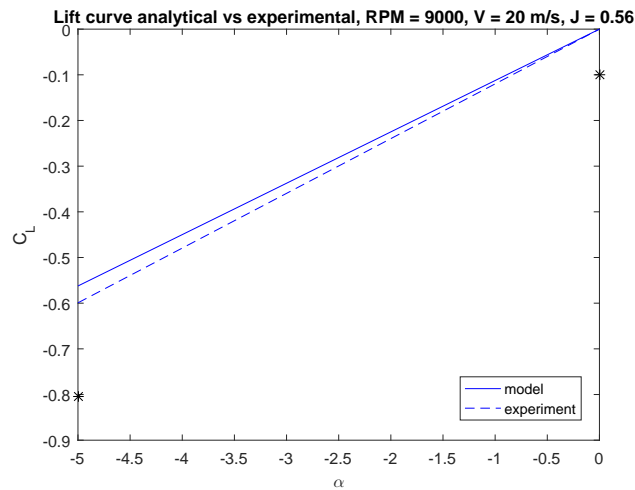


Figure 3.33: Lift curve at $J = 0.56$, analytical vs experimental

It can be seen that at the first advance ratio $J = 0.42$ the measured lift corresponds very well to the model. It can be seen that the lift curve slope may still be slightly underestimated. Since the lift contribution of the propeller normal force is relatively small and the propeller geometry is assumed instead of known, no clear observations about the possible angle of attack effect of the propeller can be made. For the second advance ratio $J = 0.28$ the deviation of the measured lift is significantly larger compared to $J = 0.42$ and it shows that the lift curve slope is underestimated to a higher degree by the model, compared $J = 0.42$. Finally, the two measurements of lift also deviate from the model at $J = 0.56$ and also show an underestimation of the lift curve slope.

The experimental lift curves at the same advance ratios including elevator deflections are shown in Fig. 3.34 and 3.46. Also the lift versus elevator deflections of the third advance ratio is shown for axial inflow conditions in Fig. 3.36.

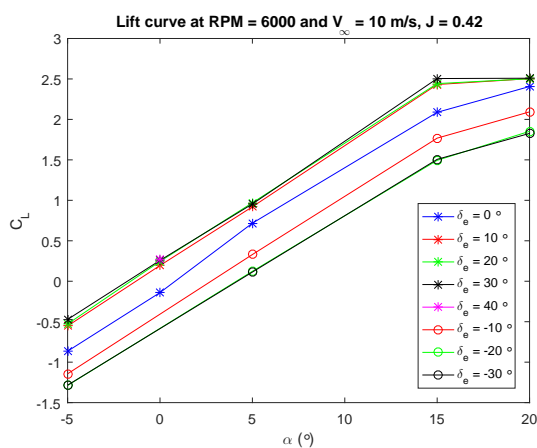


Figure 3.34: Analytical lift curve, $J = 0.42$

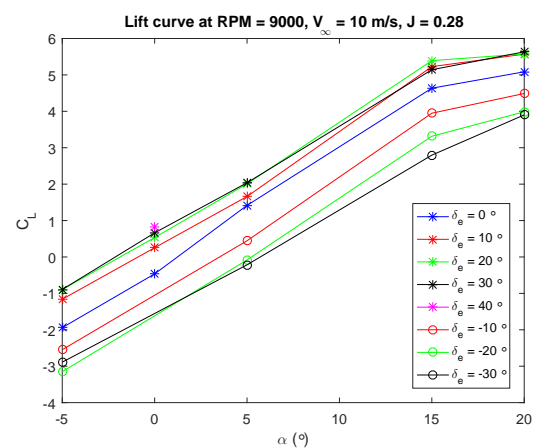


Figure 3.35: Analytical lift curve, $J = 0.28$

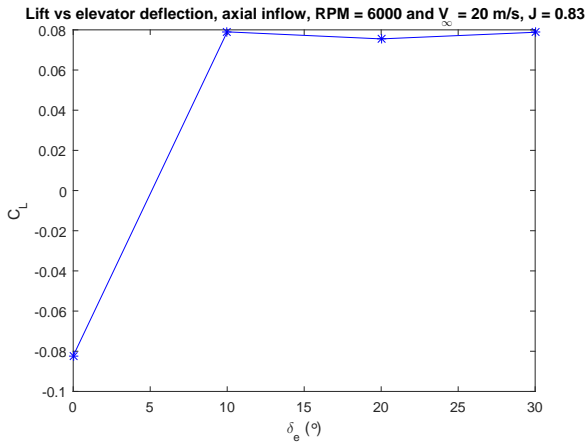


Figure 3.36: Lift versus elevator deflections at $\alpha = 0$, $J = 0.83$

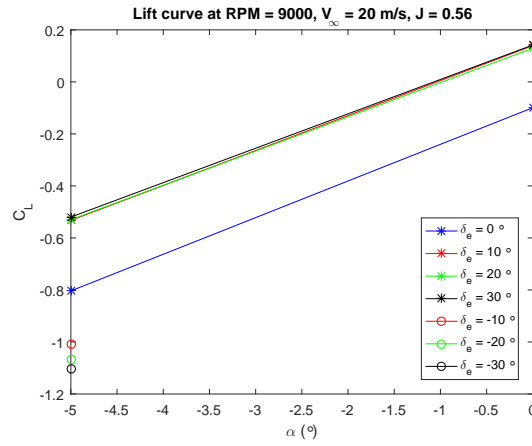


Figure 3.37: Analytical lift curve, $J = 0.56$

It can be seen for $J = 0.42$ and $J = 0.28$, that elevator deflections of $\delta_e = 10^\circ$ and $\delta_e = -10^\circ$ yield a constant increase and decrease in lift, respectively, over the complete range of angles of attack, including the angles of attack after the onset of stall. For $J = 0.83$, no increase in lift can be observed for elevator deflections higher than $\delta_e = 10^\circ$, also indicating complete stall of the elevators after $\delta_e = 10^\circ$. The same trend is observed for $J = 0.56$, where no lift increase can be seen after $\delta_e = 10^\circ$ and very small decreases of lift can be seen below $\delta_e = -10^\circ$. It can therefore be concluded that for all advance ratios, the unstalled regime of elevators is from $\delta_e = 0^\circ$ to $\delta_e = 10^\circ$. Therefore, it is worth investigating the elevator characteristics further in this range.

To take a closer look at the elevator performance in the unstalled regime, comparisons of the elevator effectiveness of model and experiment are made. The results are shown in Fig. 3.38, 3.39, 3.42 and 3.43.

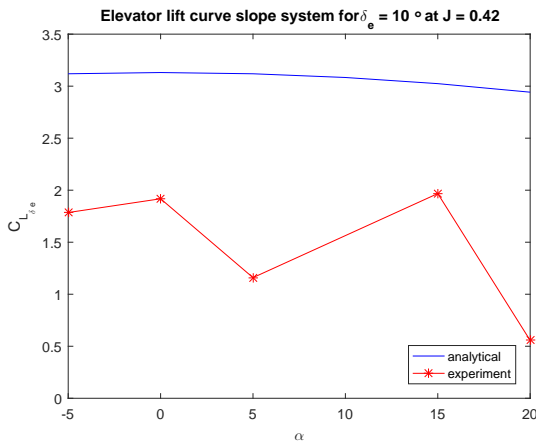


Figure 3.38: Elevator effectiveness for $\delta_e = 10^\circ$, model vs experiment, $J = 0.42$

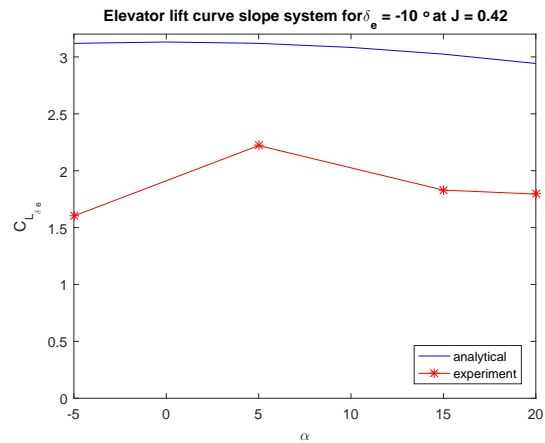


Figure 3.39: Elevator effectiveness for $\delta_e = -10^\circ$, model vs experiment, $J = 0.42$, analytical vs experiment

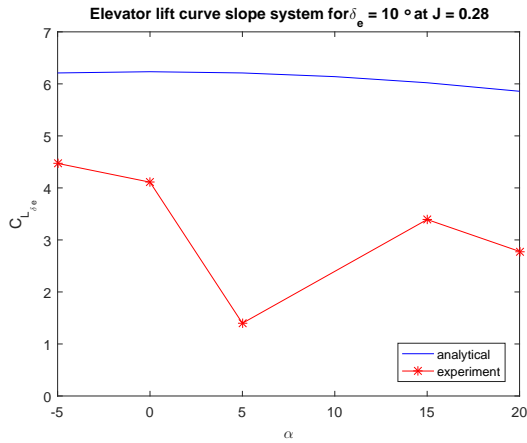


Figure 3.40: Elevator effectiveness for $\delta_e = 10^\circ$, model vs experiment, $J = 0.28$

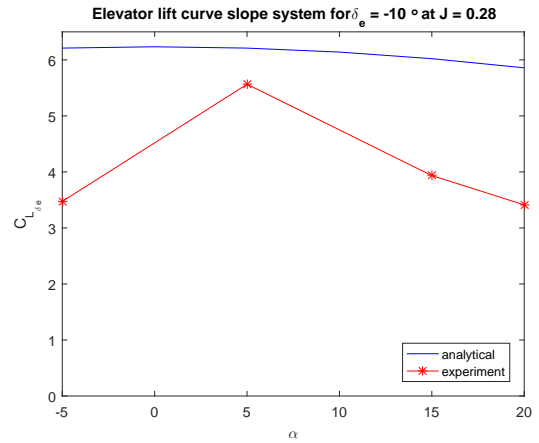


Figure 3.41: Elevator effectiveness for $\delta_e = -10^\circ$, model vs experiment, $J = 0.28$

It can be seen that the elevator effectiveness is overpredicted by the model. The elevator effectiveness also appears to fluctuate significantly over the angle of attack range. This may be caused by deficiencies in the DUUC ducted propeller scale model or by flow disturbances under angles of attack, caused by components of the ducted propeller upstream of the elevators. Since the analytical model approximates the control surfaces as 3D wings with a uniform inflow velocity field, it is not capable of taking into account all flow phenomena, which may be the primary cause for the overprediction of the elevator effectiveness. To compare the elevator effectiveness for advance ratios, the elevator effectiveness as a function of angle of attack for advance ratios $J = 0.42$ and $J = 0.28$ are plotted in Fig. 3.42 and 3.43, respectively.

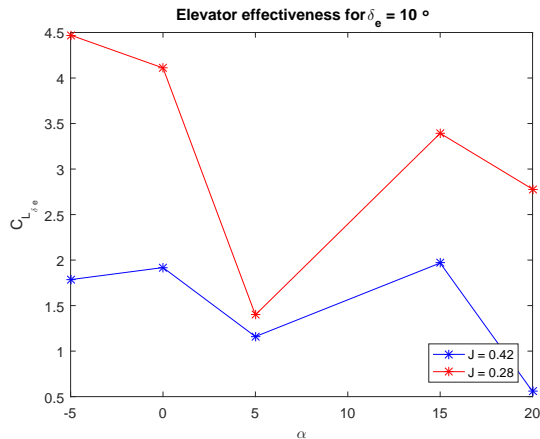


Figure 3.42: Elevator effectiveness for $\delta_e = 10^\circ$, model vs experiment, $J = 0.28$

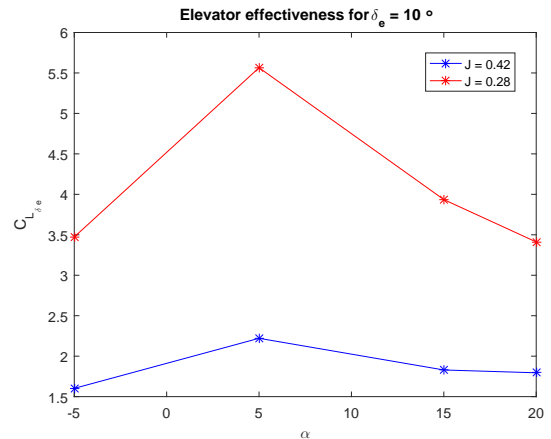


Figure 3.43: Elevator effectiveness for $\delta_e = -10^\circ$, model vs experiment, $J = 0.28$

Not enough measurements were done at advance ratios $J = 0.83$ and $J = 0.56$, to compare the elevator effectiveness at these advance ratios as well.

The installed thrust variation under angles of attack is compared for the model and the experiments for advance ratios $J = 0.42$ and $J = 0.28$ in Fig. 3.44 and 3.45, respectively.

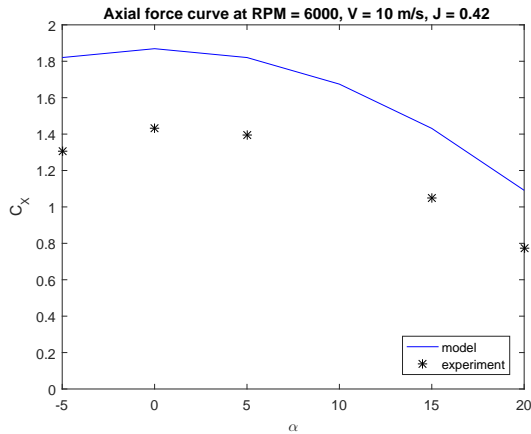


Figure 3.44: Axial force curve at $J = 0.42$, analytical vs experimental

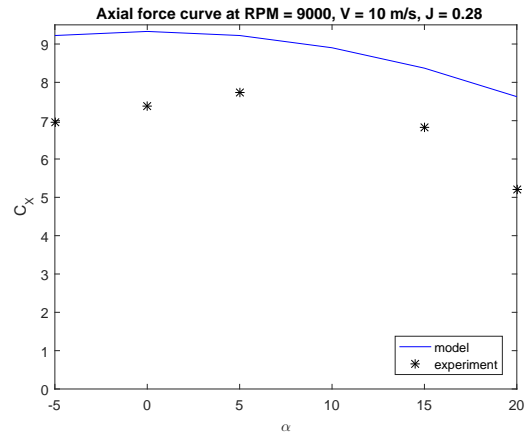


Figure 3.45: Axial force curve at $J = 0.28$, analytical vs experimental

It can be seen that the axial force is overestimated for both advance ratios. Having validated the numerical model in terms of its duct thrust output for a given propeller thrust, the difference in thrust may be attributed to an underprediction of the drag. The analytical model may underpredict the drag because of aerodynamic phenomena and interference effects that can not be modeled by low order analytical methods. Furthermore, similar to the case of power off conditions, the interference drag from [27] that is used in the analytical model may underestimate the interference drag in this Reynolds number range.

The experimental axial force curves at the same advance ratios including elevator deflections are shown in Fig. 3.35, 3.47.

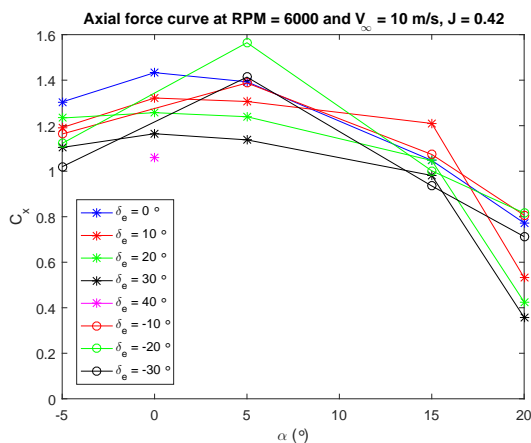


Figure 3.46: Analytical axial force curve, $J = 0.42$

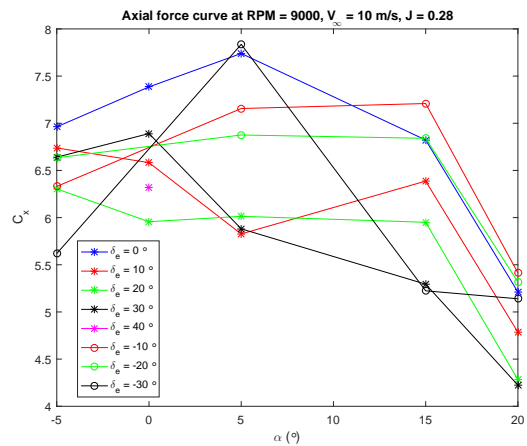


Figure 3.47: Analytical axial force curve, $J = 0.28$

Contrary to the elevator effect on the lift curve slope, the effect of elevator deflections is less pronounced in the net thrust curve. The curve of the first advance ratio contains parts in which a constant decrease of net thrust can be observed at elevator deflections. However, irregularities in trends are observed as well. For the second advance ratio, a higher level of irregularities in the net thrust variation with elevator deflections is seen. This can be attributed to a combination of geometric model irregularities and aerodynamic disturbances in the flow, resulting from interactions effects between elevator deflections and the geometry upstream of the elevators. However, for both advance ratios, the thrust is generally lower for higher elevator deflections, indicating an increase of induced drag with deflections.

The analytical model is now compared to the lift and axial force curves with elevator deflections of $\delta_e = 10^\circ$ and $\delta_e = -10^\circ$ only. The results are shown in Fig. 3.31 and 3.49.

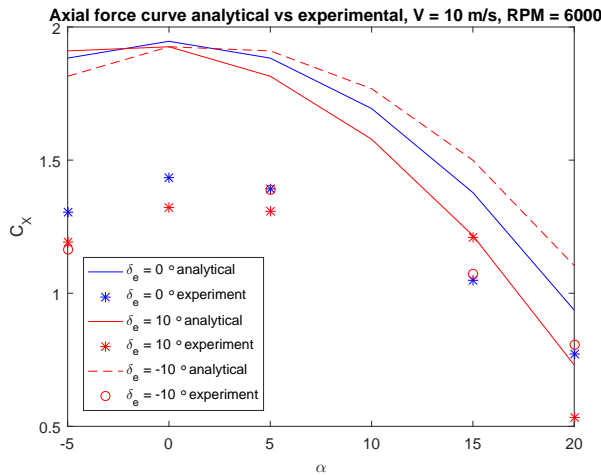


Figure 3.48: Lift curve with control surface deflections at $J = 0.42$, analytical vs experimental

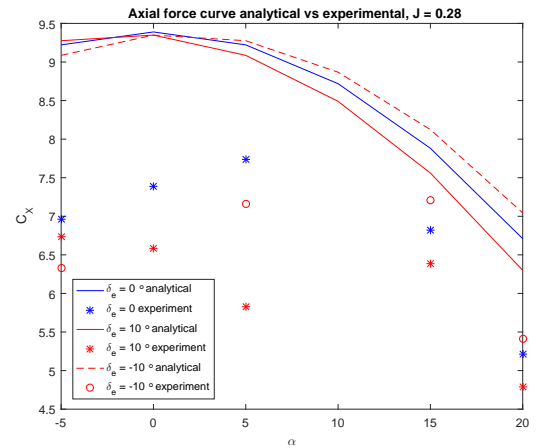


Figure 3.49: Axial force with control surface deflections, $J = 0.42$, analytical vs experiment

It can be seen that the measured data have high levels of deviation from the analytical drag model, which makes the analytical model no valid tool for predicting elevator induced drag.

SIDE FORCE CURVES

As shown in the model, the side force curve for an axisymmetric duct is similar to the lift curve, with a difference in the effective sideslip angle, which is lower than the freestream sideslip angle, because of the configuration of two ducted fans next to each other. It is thus expected that the side force curve slope is lower than the lift curve slope. To investigate this, the lift curve and side force curves without control surface deflections at advance ratios $J = 0.42$ and $J = 0.28$ are plotted in the same figures. The results are shown in Fig. 3.50 and 3.51.

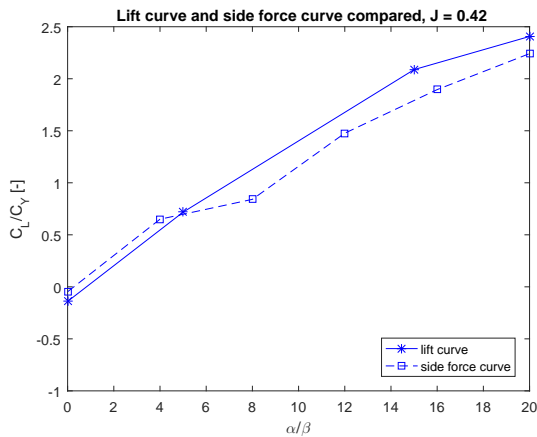


Figure 3.50: Comparison of lift curve and side force curve at $J = 0.42$

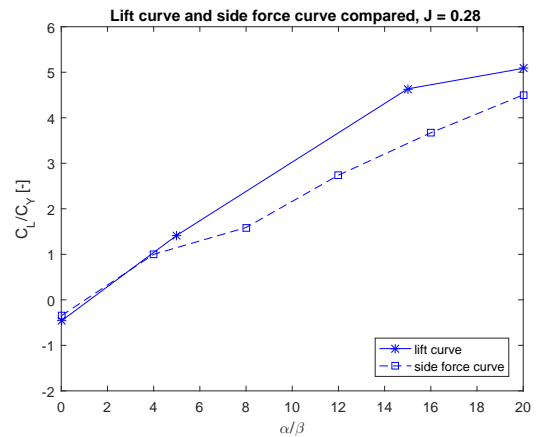


Figure 3.51: Comparison of lift curve and side force curve at $J = 0.28$

It can be seen that for the most part, the side force curve lies below the lift curve, indicating a lower effective sideslip angle indeed. Furthermore, it looks as if the onset of stall is postponed in the side force curve compared to the lift curve at the first advance ratio. At the second advance ratio, it looks as if the side force curve is completely in the unstalled regime.

The side force curves including all rudder deflections for all four advance ratios are given in Fig. 3.52, 3.53, 3.54 and 3.55.

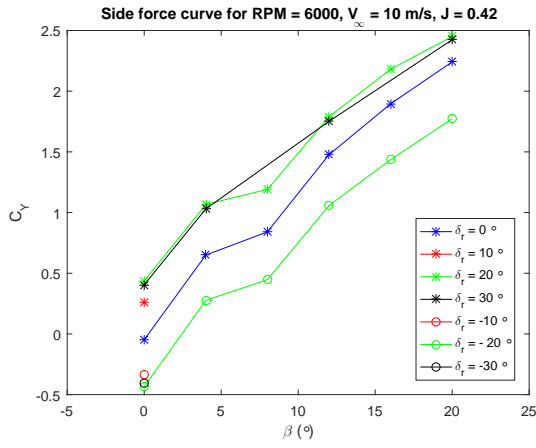


Figure 3.52: Comparison of lift curve and side force curve at $J = 0.42$

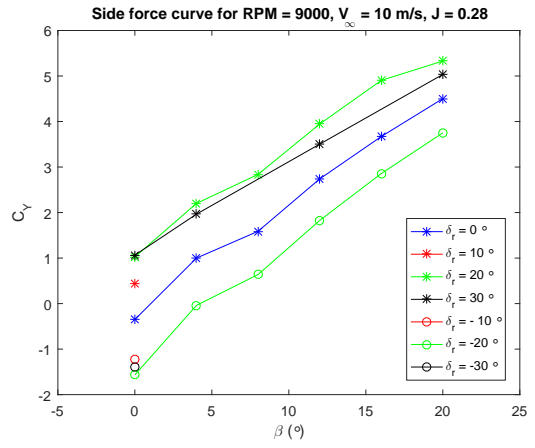


Figure 3.53: Comparison of lift curve and side force curve at $J = 0.28$

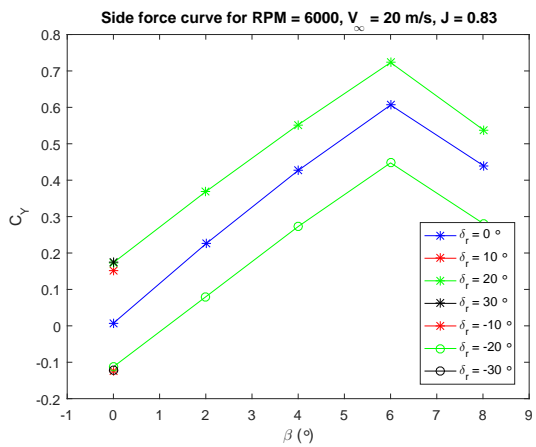


Figure 3.54: Comparison of lift curve and side force curve at $J = 0.28$

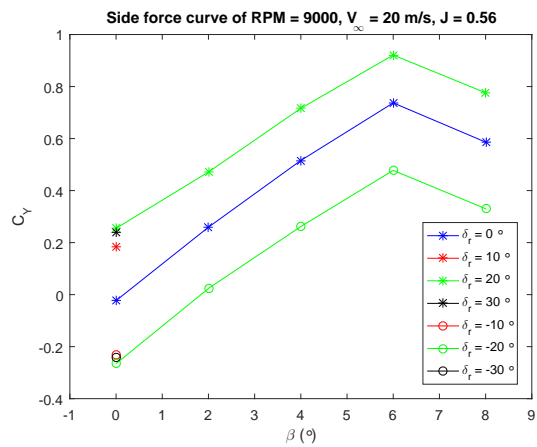


Figure 3.55: Comparison of lift curve and side force curve at $J = 0.28$

Considering all advance ratios, the stall of control surfaces is delayed compared to the lift curves, since there is a larger gap in lift between the absolute rudder deflections of $\delta_r = 10^\circ$ and $\delta_r = 20^\circ$. Also, for all four advance ratios the increase in side force for rudder deflections is almost perfectly constant over the range of sideslip angles, contrary to what is seen in the lift curves for elevator deflections. For advance ratios $J = 0.83$ and $J = 0.56$, the stall angle is very low and stall happens very abrupt. The onset of stall takes place between $\beta = 6^\circ$ and $\beta = 8^\circ$ and complete stall can be observed in both advance ratios at $\delta_r = 8^\circ$. Since the stall is very abrupt, no effect of the power settings on the onset of stall can be observed. It can be noted that the rudder effectiveness is not influenced significantly by the stall of the system. This may indicate leading edge stall and consequently no change in the flow at the trailing edge of the system. Deflections of the rudder in the unstalled regime were only recorded in axial inflow conditions. Therefore this effectiveness is plotted for positive and negative rudder deflections for all advance ratios in Fig. 3.56.

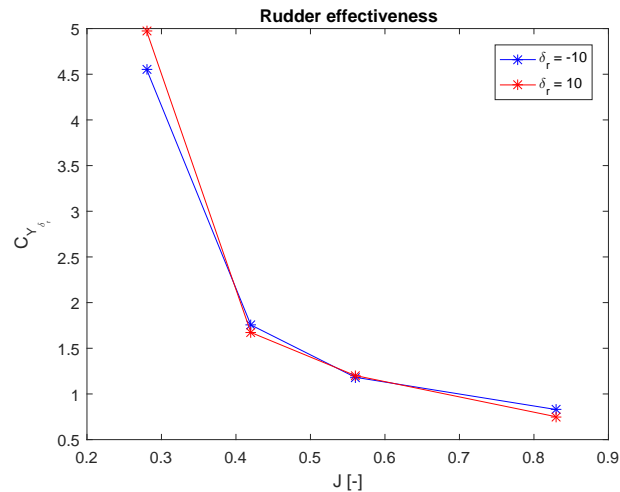


Figure 3.56: Static installed thrust, model vs experiment

It can be observed that elevator effectiveness decreases with advance ratio.

Next, it is interesting to consider the influence of elevator deflections in the unstalled regime on the side force curve of the ducted propeller. These results are shown for all advance ratios in Fig. 3.57, 3.58, 3.59 and 3.60.

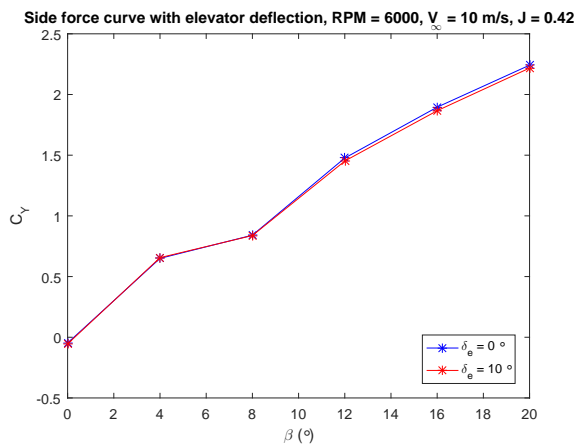


Figure 3.57: Side force curve including elevator deflection at $J = 0.42$

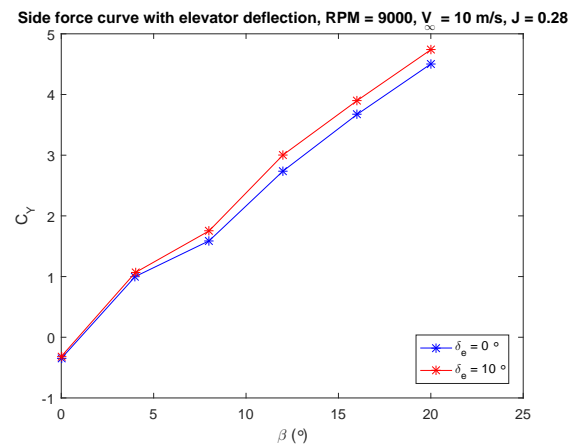


Figure 3.58: Side force curve including elevator deflection at $J = 0.28$

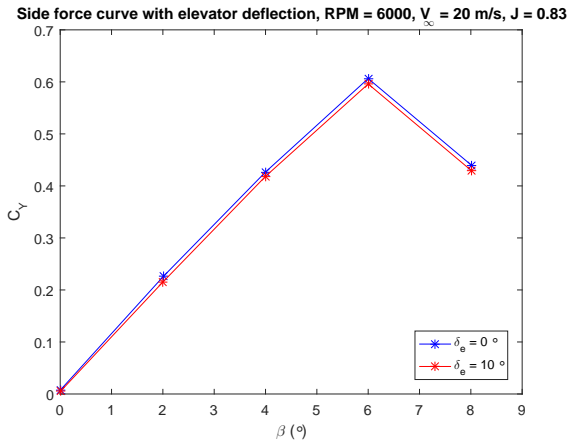


Figure 3.59: Side force curve including elevator deflection at $J = 0.28$

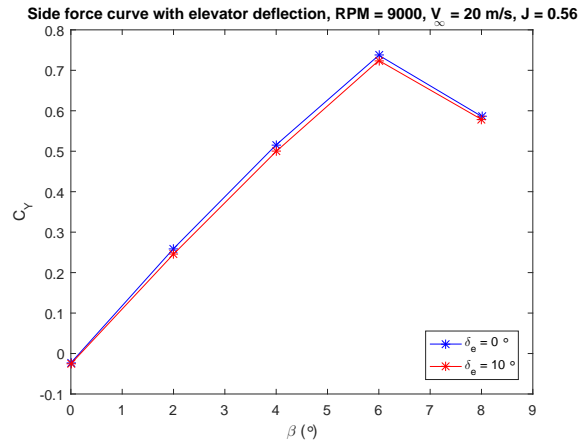


Figure 3.60: Side force curve including elevator deflection at $J = 0.28$

As can be seen, the elevator deflection of 10 degrees has no significant influence on the side force curve at any of the advance ratios. This may indicate no significant upstream effect of elevator deflections on the flow in at least their unstalled regime.

NET THRUST AT SIDESLIP ANGLES

The comparisons of the net thrust versus angle of attack and the net thrust versus sideslip angle at the same advance ratios are shown in Fig. 3.61 and 3.62.

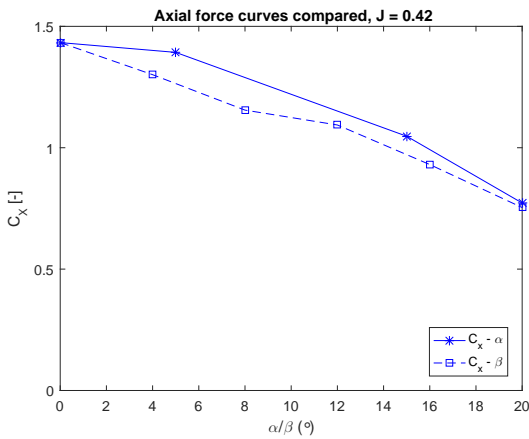


Figure 3.61: Comparison of axial force curves at $J = 0.42$

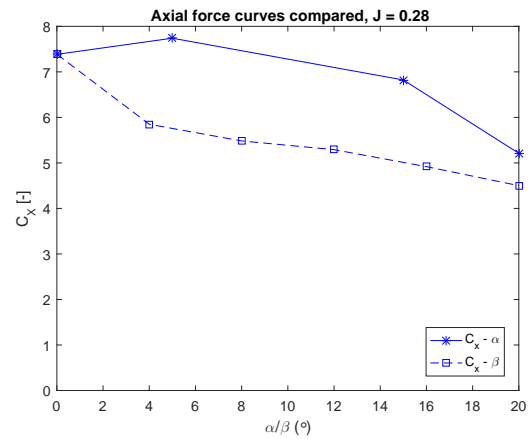
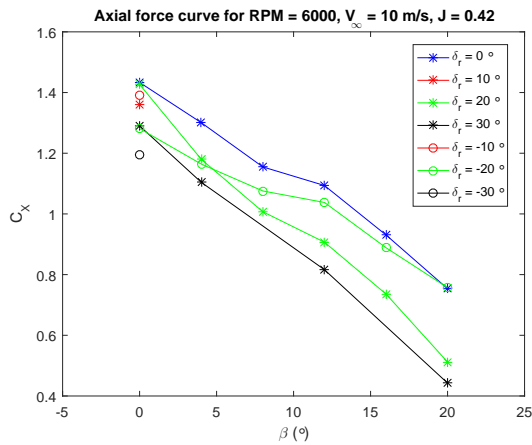
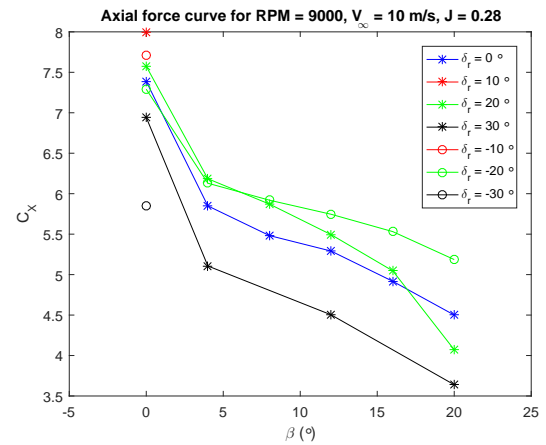
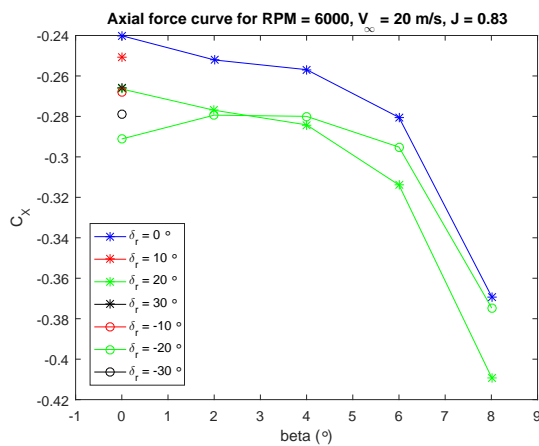
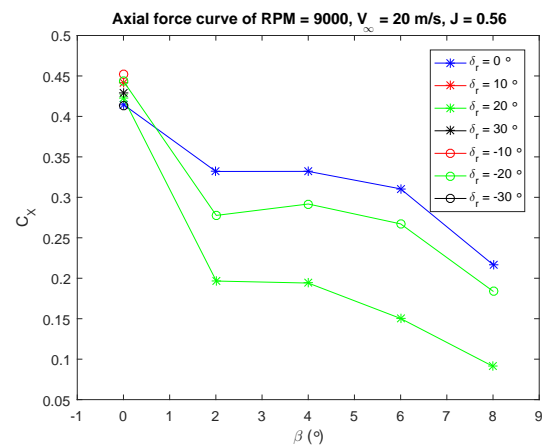


Figure 3.62: Comparison of axial force curves at $J = 0.28$

It can be seen that the axial force is lower for sideslip angles compared to angles of attack. It is not clear from theory how this effect is caused.

Next, the axial force versus sideslip angles including all rudder deflections are given for all advance ratios in Fig. 3.63, 3.64, 3.65 and 3.66.

Figure 3.63: Side force curve including elevator deflection at $J = 0.42$ Figure 3.64: Side force curve including elevator deflection at $J = 0.28$ Figure 3.65: Side force curve including elevator deflection at $J = 0.28$ Figure 3.66: Side force curve including elevator deflection at $J = 0.28$

First, it can be seen that the thrust is slightly negative and very low at $J = 0.83$ and $J = 0.56$, respectively. This indicates the loss of effectiveness of the duct at higher speeds. Furthermore, it can be seen that the variations in axial force with rudder deflections are more structured compared to the variations in lift with elevator deflections. However, trends are still not predictable and even axial force increases with rudder deflections can be observed at the second and fourth advance ratio. It is unclear how this effect is caused.

The elevator deflection in the unstalled regime on the axial force curve versus sideslip angle is also interesting to consider. The results for all advance ratios are given in Fig. 3.67, 3.68, 3.69 and 3.70.

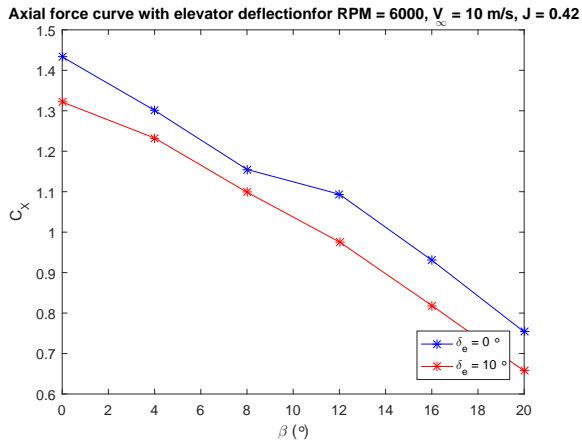


Figure 3.67: Axial force curve including elevator deflection at $J = 0.42$

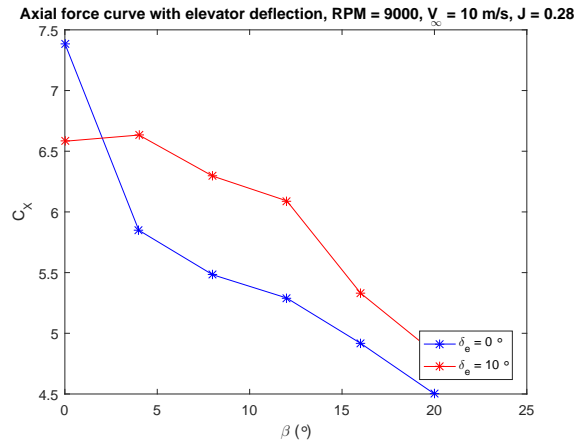


Figure 3.68: Axial force curve including elevator deflection at $J = 0.28$

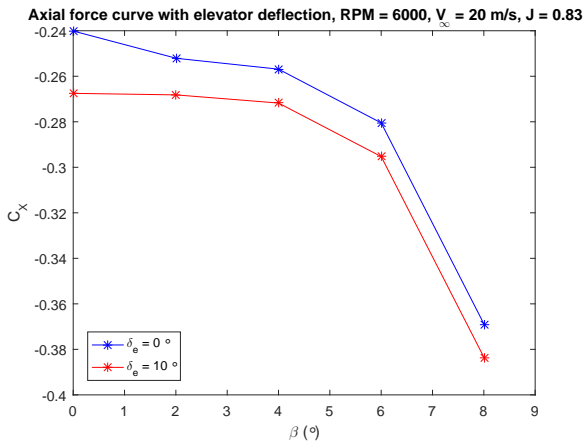


Figure 3.69: Axial force curve including elevator deflection at $J = 0.28$

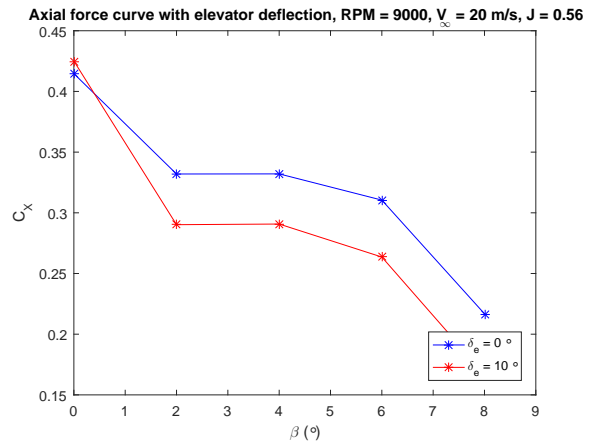


Figure 3.70: Axial force curve including elevator deflection at $J = 0.28$

It is clearly visible that for the first, third and fourth advance ratio, the decrease in axial force is approximately constant over the complete range of sideslip angles, indicating a constant increase in induced drag. However, the second advance ratio shows an increase in axial force, which is not constant over the range of sideslip angles either. This is caused by unknown phenomena.

SIMULTANEOUS ELEVATOR AND RUDDER DEFLECTIONS IN PROPELLER ON CONDITIONS

In propeller on conditions, the simultaneous deflections of elevators and rudders have been tested in axial inflow conditions at all four advance ratios. The effect on lift, side force and axial force is investigated.

The lift force as a function of elevator deflections for various rudder deflections at all four advance ratios are given in Fig. 3.71, 3.72, 3.73 and 3.74.

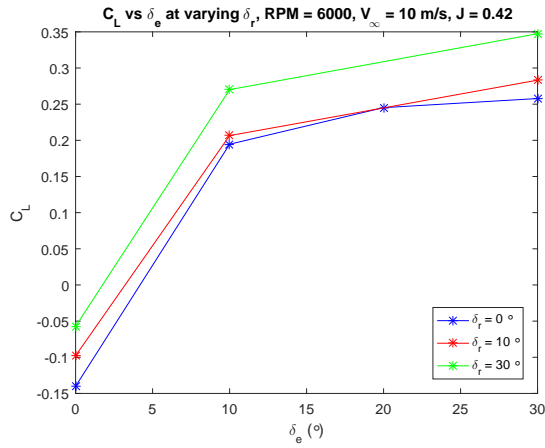


Figure 3.71: Lift vs elevator deflection for various rudder deflections at $J = 0.42$

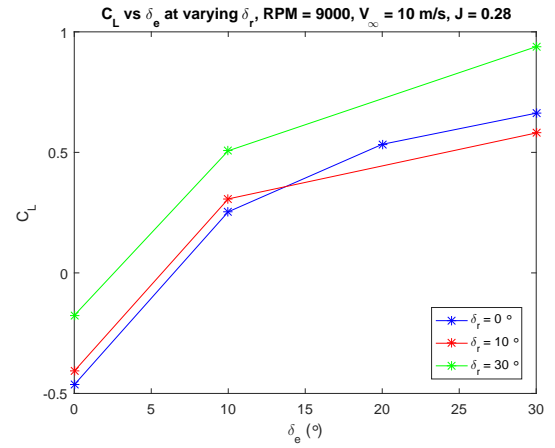


Figure 3.72: Lift vs elevator deflection for various rudder deflections at $J = 0.28$

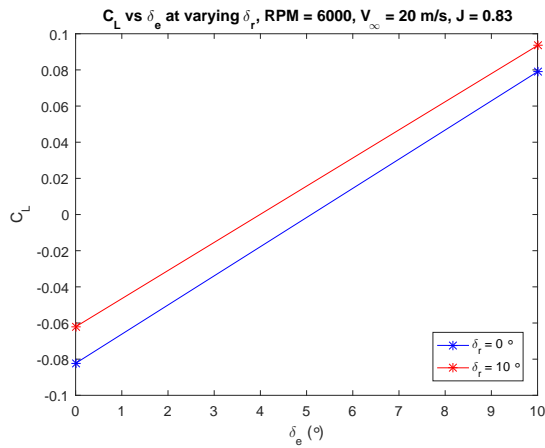


Figure 3.73: Lift vs elevator deflection for various rudder deflections at $J = 0.28$

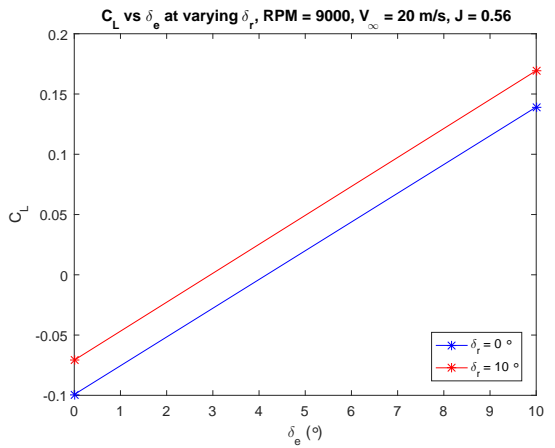


Figure 3.74: Lift vs elevator deflection for various rudder deflections at $J = 0.28$

As can be seen, the rudder deflections add approximately a constant increase in lift for all advance ratios and do not affect the elevator effectiveness, since the slope of the curves is unchanged in the unstalled regime from $\delta_e = 0^\circ$ to $\delta_e = 10^\circ$. It is possible that the rudders and elevators yield superelevations without flow separation effects, resulting in a higher effective velocity that the elevators see, and therefore a higher lift increase. However, this would yield a higher elevator effectiveness and not specifically a constant lift increase over the complete angle of attack range. This is observed for all advance ratios and may be due to geometric deficiencies in the model, which yield a lift generation by the rudders as well.

The side force as a function of rudder deflection for several elevator deflections at all advance ratios is given in Fig.

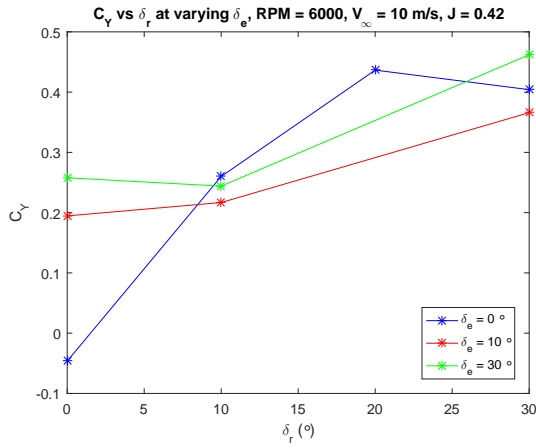


Figure 3.75: Side force vs rudder deflection for various elevator deflections at $J = 0.42$

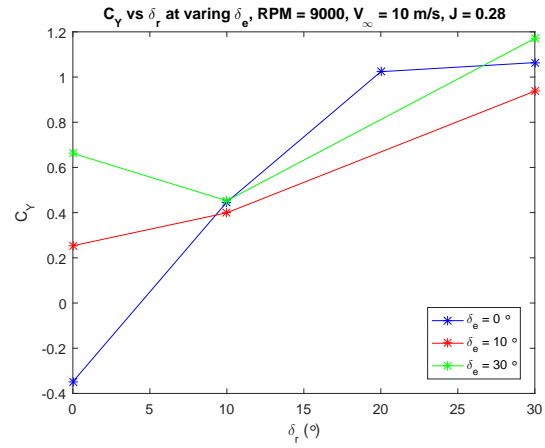


Figure 3.76: Side force vs rudder deflection for various elevator deflections at $J = 0.28$

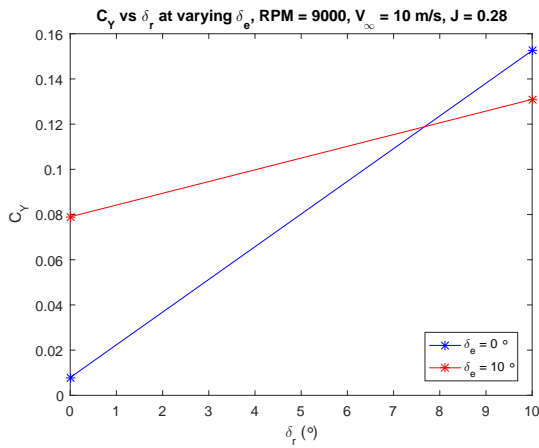


Figure 3.77: Side force vs rudder deflection for various elevator deflections at $J = 0.28$

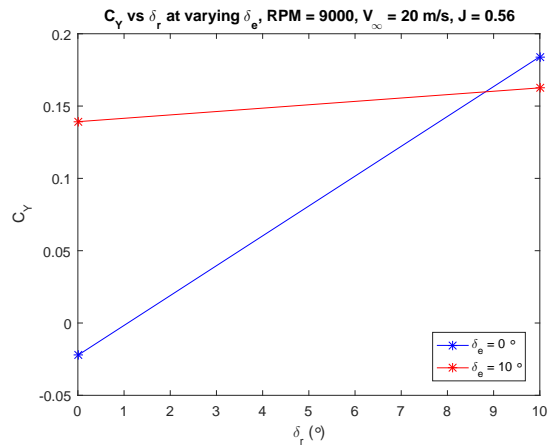


Figure 3.78: Side force vs rudder deflection for various elevator deflections at $J = 0.28$

It can be seen that, contrary to the rudder effect on the elevators, the elevators have a significant effect on the rudder effectiveness. This may be due to interference effects, which are heavily dependent on the geometric design.

4

DESIGN STUDIES

It can be concluded that the complete aerodynamic performance model was not validated completely. It is clear that the model has several deficiencies, including its prediction of lift and drag. The numerical part of the model, consisting of XROTOR and DFDC are validated to a higher degree. DFDC was shown to predict thrust variations for one particular reference case of a ducted propeller very accurately. For the DUUC configuration, the model was shown to predict trends in thrust very well over the range of speeds and power settings. Since DFDC does not include a drag model for the DUUC configuration and the analytical drag model appeared to have defects, the absolute thrust prediction of the DUUC ducted propeller scale model could not be verified against experimental data. Due to a lack of reference cases with enough data on geometry and operational conditions, DFDC could not be validated for a wide range of ducted propeller geometries. However, being very accurate for one reference case, it is assumed that DFDC is capable of modeling performance trends for geometric changes as well. Therefore, DFDC is used in this chapter to model the influence of both general geometric design parameters and operational conditions and power settings on the total efficiency and propeller efficiency at zero angle of attack. The ducted fan model by Grunwald and Goodson, which was initially used to validate the program, is taken as the base model, on which several design changes are applied separately. Duct, propeller and centerbody aerodynamics from DFDC are studied to gain more insight into how the design and operational condition influence the performance.

4.1. DEFINITION OF VARIABLES AND METHODOLOGY

A number of geometric parameters as well as operational conditions are used for a sensitivity analysis of the ducted fan system. The results are then analyzed in terms of several variables. Before the results are outlined, clear definitions of all investigated variables and outcomes are given. Some of the variables may differ in definition from the same variables, used in the performance model in Chapter 2. When varying one parameter, other parameters are kept constant as much as possible. Furthermore, for all analyses the propeller geometry is kept constant.

4.1.1. REYNOLDS NUMBER

The Reynolds number that is used in the sensitivity analysis is based on the freestream velocity and duct chord. Although the duct does not see the actual freestream velocity if the propeller is on, this Reynolds number is still used as a reference for comparison. It can be illustrated with the following equation:

$$Re = \frac{\rho V_{\infty} c_{\text{duct}}}{\mu} \quad (4.1)$$

where ρ , μ and c_{duct} are the atmospheric gas density, dynamic viscosity and duct chord length, respectively.

The Reynolds number is changed only by changes in gas properties ρ and μ , since changes in velocity would yield changes in either advance ratio or geometry, which are parameters that are to be investigated separately and should be kept constant in this case.

The Reynolds number is varied to four values in the analysis. To vary the Reynolds number, the validation model from Grunwald and Goodson is taken as the baseline model, which has a Reynolds number of 550,000

based on the freestream velocity and duct chord. The following changes are applied to change the Reynolds number:

- The atmospheric properties of air at 15000 m altitude in the standard atmosphere are taken, which correspond to a density of $\rho = 0.1948 \text{ kg/m}^3$ and a dynamic viscosity of $\mu = 1.422 \cdot 10^{-5} \text{ Ns/m}^2$. This yields a lower Reynolds number of $Re = 109,340$.
- Only the density is multiplied by three to obtain $\rho = 6.675 \text{ kg/m}^3$, while the dynamic viscosity is kept the same, namely $\mu = 1.728 \cdot 10^{-5} \text{ Ns/m}^2$. This yields a Reynolds number that is three times as high as that of the baseline model, namely $Re = 1,639,300$.
- Finally, the properties of water at 5° C are used as input, in order to obtain a much higher Reynolds number. The density and dynamic viscosity of water at 5 degrees Celcius are $\rho = 1000 \text{ kg/m}^3$ and $\mu = 1.519 \cdot 10^{-3} \text{ Ns/m}^2$, respectively, yielding a Reynolds number of $Re = 4,465,800$.

4.1.2. ADVANCE RATIO

Besides the Reynolds number, it is interesting to look at the effect of advance ratio on the ducted fan performance. The advance ratio of a propeller is defined as the ratio of the freestream velocity to the tip speed of the propeller. Another definition is the ratio of the distance traveled during one revolution of the propeller blades to the diameter of the propeller. It is illustrated by the following equation:

$$J = \frac{V_{\infty}}{n D_{\text{prop}}} \quad (4.2)$$

where n is the revolutions per second and D is the propeller diameter.

Keeping the propeller geometry constant to avoid Reynolds number effects, either the freestream velocity or the propeller RPM should be varied to change the advance ratio. It is chosen to vary only the freestream velocity, while keeping RPM constant. This is a common setting in propeller aircraft, where the RPM of the propeller is kept constant during several phases of flight, such as take-off, cruise and landing, while the velocity varies in these phases. Taking the validation baseline model, which has an advance ratio of 0.6, the advance ratio is varied between 0 and 1.4 by varying the freestream velocity.

4.1.3. TIP CLEARANCE

Tip clearance is an important parameter in ducted propeller design, since it is closely related to one of the main benefits of ducting a propeller, namely reducing its tip losses. From several research on ducted fan performance it can be concluded that the tip clearance should always be kept as low as possible, since propeller efficiency always increases with decreasing tip clearance. Tip clearances that are too high may lead to flow reversal at the blade tips, which may lead to lip separation on the inner duct surface.

The tip clearance of a ducted propeller is defined as the gap between the tip of the propeller blades and the duct's inner surface at the propeller blade position and is an important parameter in ducted fan design. The definition of tip clearance used here is the tip gap expressed as a ratio to the propeller diameter:

$$tc = \frac{D_{\text{duct,inner}}(x/c_{\text{prop}}) - D_{\text{prop}}}{2 D_{\text{prop}}} \quad (4.3)$$

DFDC does not allow for a tip clearance in its input file and when a gap is specified in the geometry it extrapolates the rotor in the gap, to obtain an ideal tip clearance of zero. However in the program itself the option of changing the tip gap is present. By using this option a gap is generated between the blade tips and the lower duct surface by keeping the propeller diameter constant and shifting the duct away from the propeller, hence slightly increasing the duct diameter as well. The effect of tip clearance on the performance is investigated in this way.

4.1.4. PROPELLER LONGITUDINAL POSITION

The longitudinal position of the propeller in the duct is expressed as the ratio of the propeller location to the duct chord length as follows:

$$(x/c)_{\text{prop}} = \frac{x_{\text{prop}}}{c_{\text{duct}}} \quad (4.4)$$

Here x_{prop} is the position of the propeller measured from the leading edge of the duct. When changing the propeller position the tip clearance is kept constant to the ideal zero value, such that the duct diameter inevitably changes with changing propeller location. However, for this analysis it is proper to use another duct airfoil profile with a flat lower surface, such that, over part of the chord length, the tip clearance, outer duct diameter and possibly inflow velocity can all be kept constant while varying the propeller position. This way, the effect of propeller position only can be investigated properly. Therefore a Clark Y airfoil is used for the duct, which is rotated, such that the lower surface is horizontally straight from $0.3c$ to c . Also the leading edge of the duct is shifted to the right compared to the baseline model, such that the spinner part of the centerbody lies completely outside of the duct. This enables for a constant propeller radius and propeller area at different propeller positions in DFDC.

4.1.5. ASPECT RATIO

Aspect ratio is an important parameter in ducted fan design, as could already be seen in the analytical model. The aspect ratio that is used in this analysis differs from the aspect ratio used in the model in Chapter 2, where the duct diameter is used. Since duct diameter changes with variations in duct profile, propeller position and possibly other variables, the aspect ratio used here is based on the propeller diameter, as follows:

$$AR_{\text{prop}} = \frac{D_{\text{prop}}}{c_{\text{duct}}} \quad (4.5)$$

Thus, since the propeller geometry is kept constant, only the duct chord is varied to change the aspect ratio. The Clark Y airfoil is taken again and elongated and shortened for different aspect ratios. Complete scaling of the airfoil leads to changes in duct diameter and consequently changes in tip clearance and in propeller inflow velocity, compared to the baseline model. For several aspect ratios, the propeller position as a fraction of the duct chord $(x/c)_{\text{prop}}$ is kept constant as well.

4.1.6. CAMBER

The airfoil profile of the duct is a critical design variable as it has great influence on the lift and drag performance and stall characteristics. However, it also affects the thrust performance and consequently the efficiency of the ducted propeller. One of the most important geometric airfoil parameters is camber. Camber is a means to express the asymmetry between the upper and lower surface of an airfoil. It is expressed as the distance between the camber line, which is a curve halfway between upper and lower surface, and the chord line, which is the straight line running from leading to trailing edge. This distance is then expressed in percentages of the chord. For the sensitivity analyses the camber of the duct is varied by using NACA 4 digit series airfoils for the duct shape, which all have equal thicknesses and the same maximum camber position. Only camber itself is varied. These airfoil profiles are loaded in DFDC, starting with a NACA0012 profile. The other airfoils all have maximum camber at $0.4c$ of the chord and equal thicknesses of 12 percent. They are thus NACA1412, NACA2412, NACA3412, NACA4412, NACA5412, NACA6412, NACA7412, NACA8412 and NACA9412 profiles.

4.1.7. THICKNESS TO CHORD RATIO

Thickness to chord ratio is another critical airfoil property and simply defined as the ratio of the maximum thickness of an airfoil to its chord length. To study the effect of airfoil thickness, while keeping most of the other variables constant, symmetrical NACA 4 digit series airfoils are used and only the thickness is varied. Propeller location is kept constant. Thickness is varied from 6 to 24 percent yielding NACA006, NACA009, NACA012, NACA015, NACA018, NACA021 and NACA024 airfoils.

4.2. SENSITIVITY ANALYSIS

4.2.1. REYNOLDS NUMBER

Before the effects of several design parameters on the performance of the ducted fan are studied, the influence of Reynolds number is investigated first. The effect of Reynolds number on the efficiency, thrust and power of the propeller, duct and spinner is shown in Fig. 4.1, 4.2, 4.3 and 4.4.

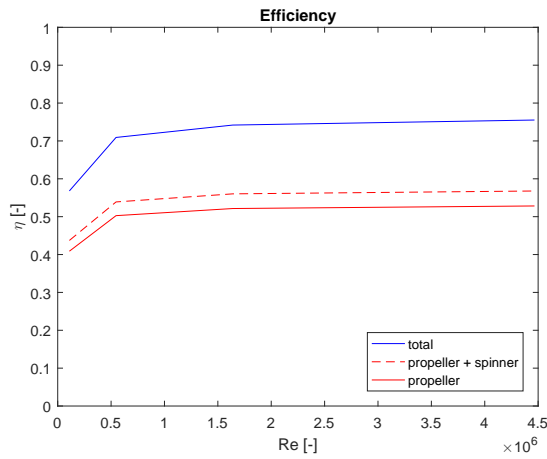


Figure 4.1: Efficiency vs Reynolds number

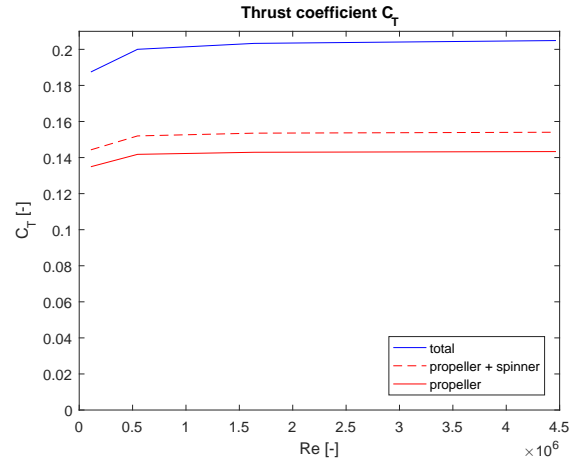


Figure 4.2: Thrust coefficient C_T vs Reynolds number

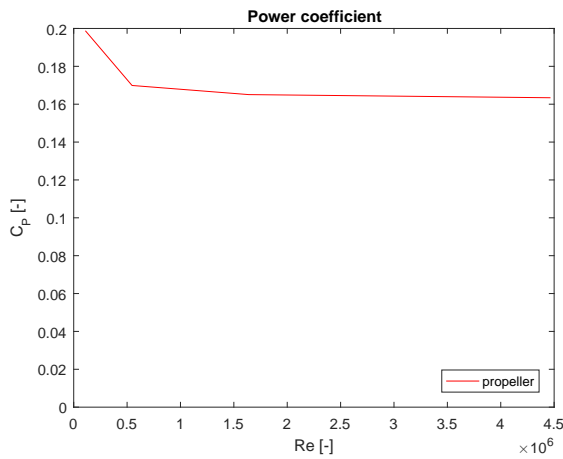


Figure 4.3: Power coefficient vs Reynolds number

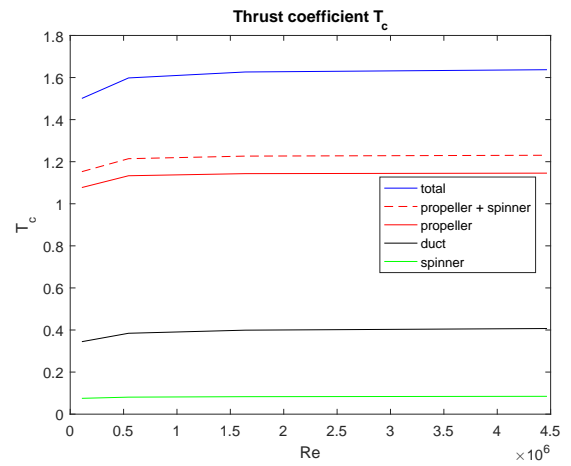


Figure 4.4: Thrust coefficient T_c vs Reynolds number

It can be seen that the Reynolds number has considerable influence on the propeller efficiency and total efficiency between Reynolds numbers of approximately $Re = 0.1 \cdot 10^6$ and $Re = 1.5 \cdot 10^6$. In this range, the efficiency increases with Reynolds number. At Reynolds numbers higher than $1.5 \cdot 10^6$, the efficiency keeps increasing but the rate of increase becomes less. Observing the C_T and C_P plots, it can be seen that the increase in efficiency is due to an increase in thrust coefficient with Reynolds number and a decrease in power coefficient with Reynolds number, which both have the highest rate in the low Reynolds number range as well. The influence of the spinner on the thrust and efficiency is approximately constant over the Reynolds number range, indicating that the spinner aerodynamics are not influenced significantly by the Reynolds number, whereas the duct and propeller thrust coefficients increase with Reynolds number.

The pressure distributions around the duct and centerbody at the different Reynolds number are shown in Fig. 4.5 and 4.6, respectively.

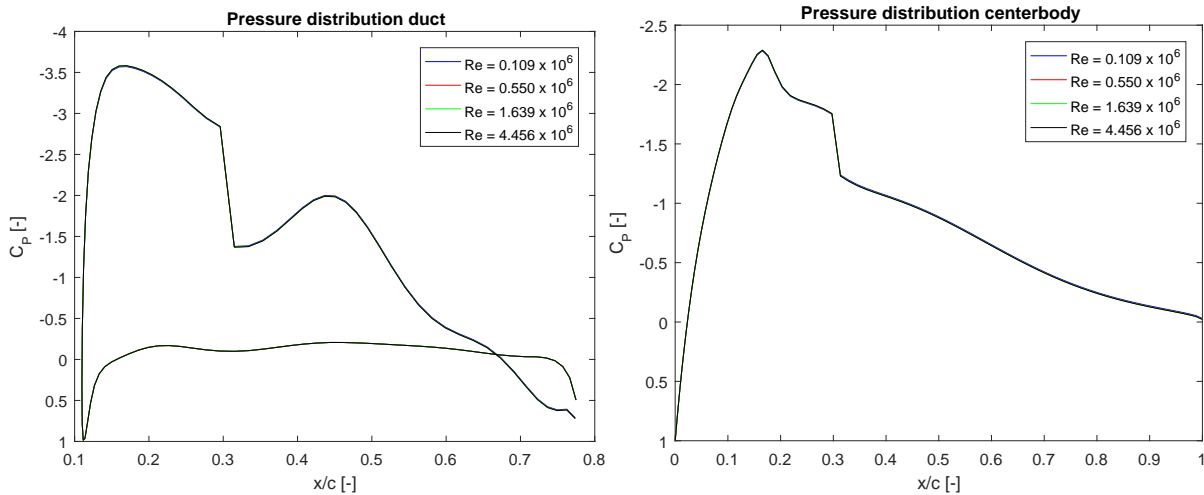


Figure 4.5: Pressure distribution around the duct for various Reynolds numbers

Figure 4.6: Pressure distribution around the centerbody for various Reynolds numbers

It can be seen that the shapes of the pressure distributions remain constant over the Reynolds number range, hence not changing the aerodynamics of the duct and centerbody. It can therefore be concluded that the change in efficiency is due to changes in dynamic pressure, which decreases the power coefficient and increases the thrust coefficient of the system as the Reynolds number gets higher. This yields a more efficient system at higher Reynolds numbers. Figures of the pressure vectors around the duct, centerbody and propeller, illustrating this effect, can be found in Appendix B.

4.2.2. ADVANCE RATIO

The performance of the ducted fan model with varying advance ratios is shown in Fig. 4.7, 4.8, 4.9 and 4.10.

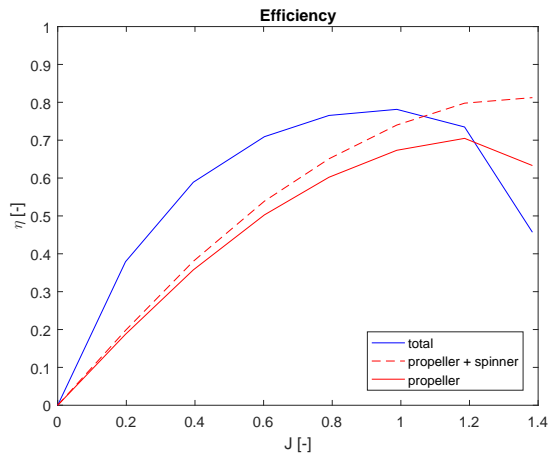


Figure 4.7: Efficiency vs advance ratio

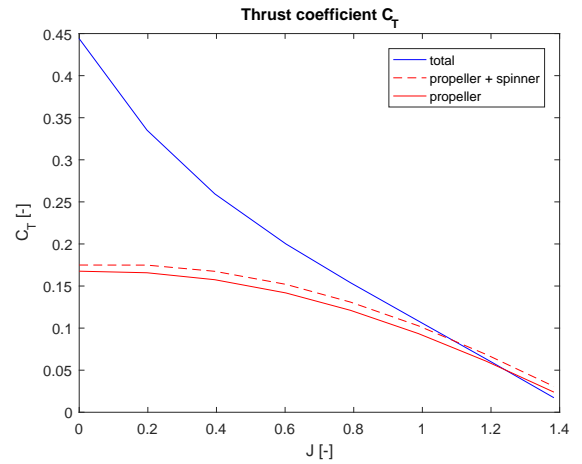


Figure 4.8: Thrust coefficient C_T vs advance ratio

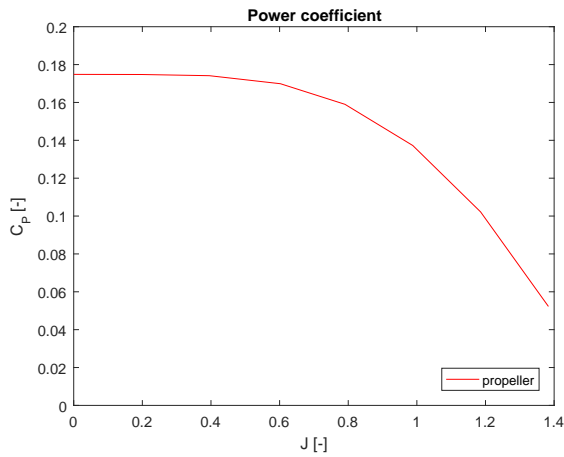


Figure 4.9: Power coefficient vs advance ratio

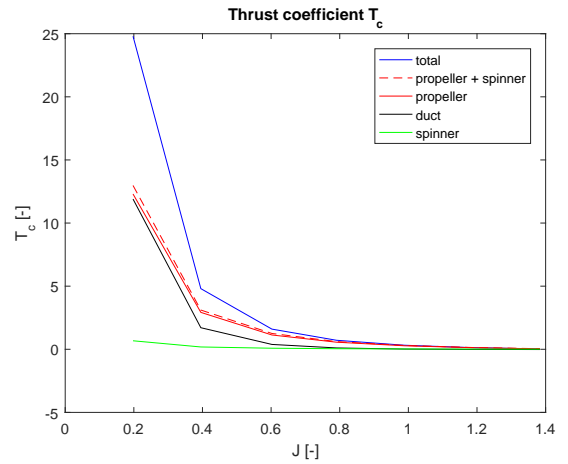


Figure 4.10: Thrust coefficient T_c vs advance ratio

The same trend in efficiency for the propeller, propeller and spinner combined and duct can be observed with advance ratio. The efficiency increases until a maximum, after which it decreases again. The point of maximum efficiency is reached earlier for the total system than for the propeller and propeller and spinner combined. The highest efficiency can be reached at the highest advance ratio for the propeller and spinner combined. It can be seen that the thrust of all components, except for the spinner, significantly decreases with increasing advance ratio. The decrease in propeller thrust can be attributed to higher propeller inflow velocities, whereas the decrease in duct thrust is due to an increase in drag of the duct. The power coefficient of the propeller remains almost constant over a significant part of the advance ratio range and decreases rapidly afterwards. The duct and propeller have approximately the trend in thrust variation over the advance ratios.

The pressure distributions around the duct and centerbody for various advance ratios are given in Fig. 4.11 and 4.12, respectively.

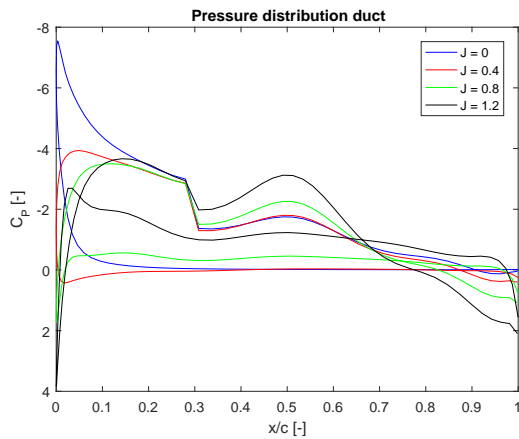


Figure 4.11: Pressure distribution around the duct for several advance ratios

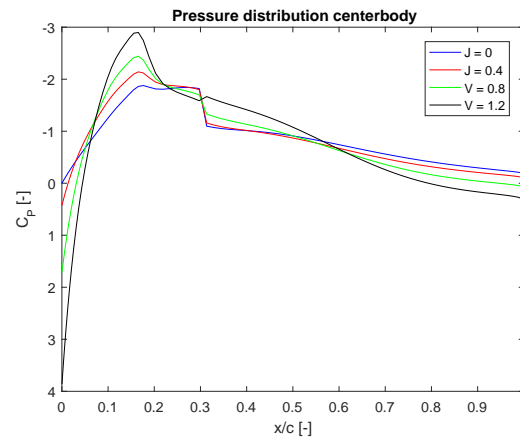


Figure 4.12: Pressure distribution around the centerbody for several advance ratios

Considering the pressure distribution around the duct and centerbody for various advance ratios, it can be seen that the area of the pressure peaks on the duct decrease for increasing advance ratios. The area enclosed by the pressure distribution around the upper and lower surface also decreases, indicating a loss in thrust. The pressure distribution around the centerbody shows an increase in pressure peaks with increasing advance ratio, followed by an increase in the adverse pressure gradient. This yields approximately a constant net pressure distribution, therefore not influencing the spinner thrust significantly. The pressure vectors, that illustrate this can be found in Appendix B.

4.2.3. TIP CLEARANCE

The results for efficiency, power coefficient and thrust coefficients as function of tip clearance are shown in Fig. 4.13, 4.14, 4.15 and 4.16.

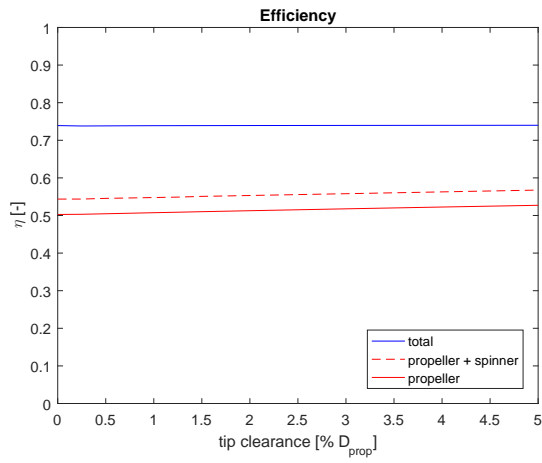


Figure 4.13: Efficiency vs tip clearance

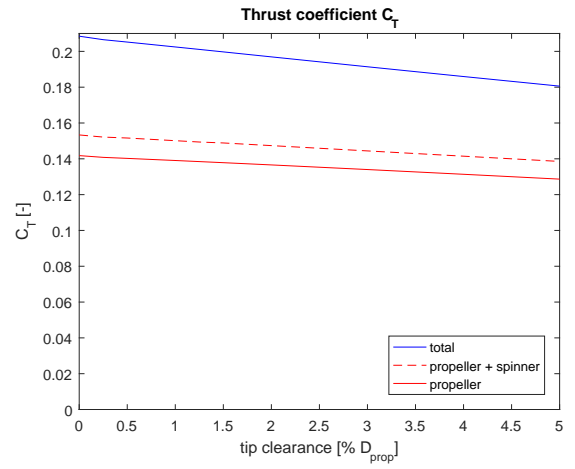


Figure 4.14: Thrust coefficient C_T vs tip clearance

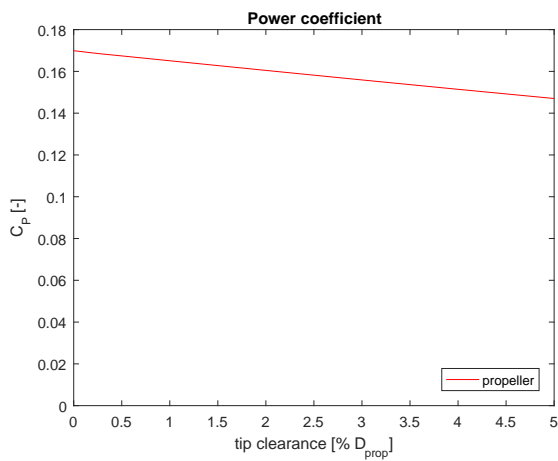


Figure 4.15: Power coefficient C_P vs tip clearance

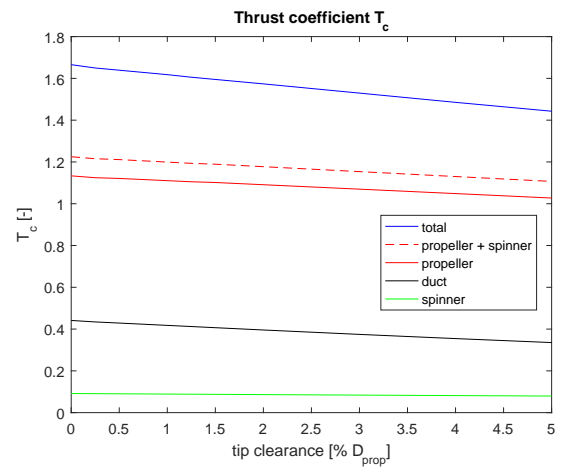


Figure 4.16: Thrust coefficient T_c vs tip clearance

It can be seen that there seems to be an almost linear relation between tip clearance and all performance parameters. The thrust of the total system, propeller and combined propeller and spinner all decrease linearly with increasing tip clearance. The total thrust decreases at a slightly higher rate than the combined propeller and spinner thrust. This is caused by the linear decrease in both propeller and duct thrust and no change in spinner thrust, as can be seen in Fig. The power coefficient of the propeller decreases linearly as well, at approximately the same rate as the total thrust coefficient. This explains the constant total system efficiency. Although the system efficiency does not change with tip clearance, the tip clearance should be kept as low as possible in order to maximize the propeller and total thrust of the system.

The pressure distributions around the duct and centerbody for the range of tip clearances are given in Fig. 4.17 and 4.18.

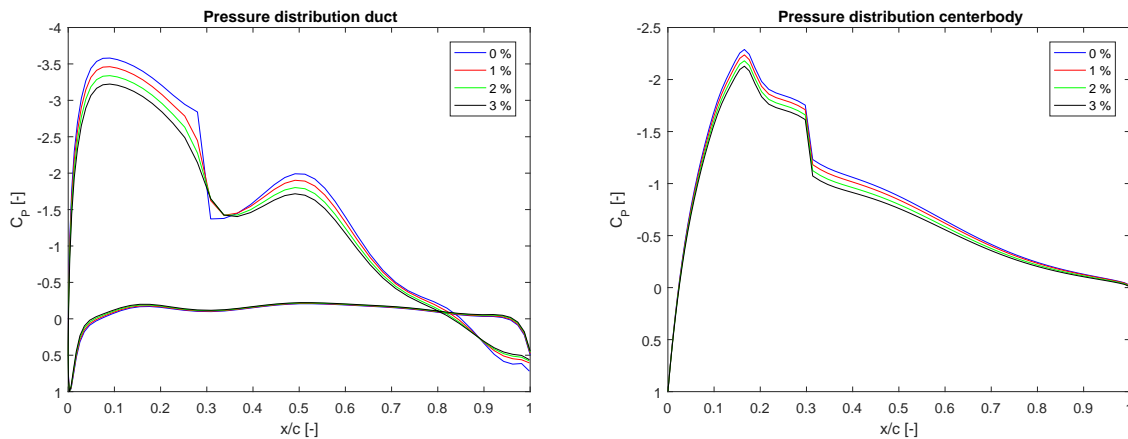


Figure 4.17: Pressure distribution around the duct for variable tip clearance

Figure 4.18: Pressure distribution around the centerbody for variable tip clearance

The pressure distribution on the duct shows approximately constant increases in pressure on the upper surface of the duct with increasing advance ratio and no negligible changes on the lower surface. This indicates a loss of thrust. The pressure distribution on the centerbody shows slight increases in pressure peaks which are canceled out by increases in pressure in the adverse pressure gradient. This illustrates a constant spinner thrust over the range of tip clearances. More details pressure vectors can be found in Appendix B.

4.2.4. PROPELLER LONGITUDINAL POSITION

The trends in efficiency, thrust coefficients and power coefficients versus propeller longitudinal position are shown in Fig. 4.19, 4.20, 4.21 and 4.22.

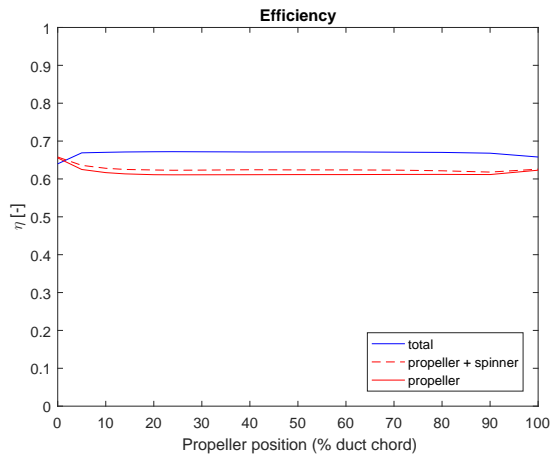


Figure 4.19: Efficiency vs propeller position

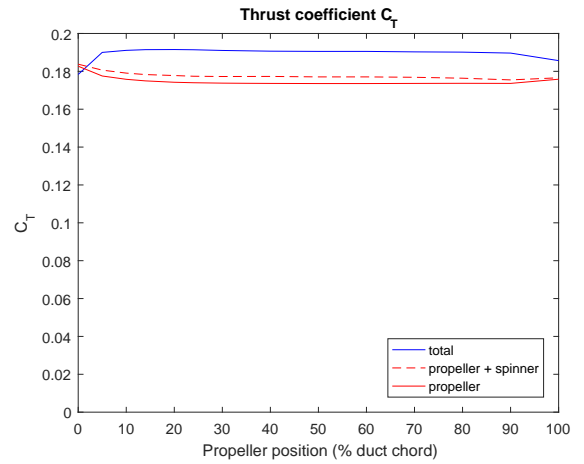


Figure 4.20: Thrust coefficient C_T vs propeller position

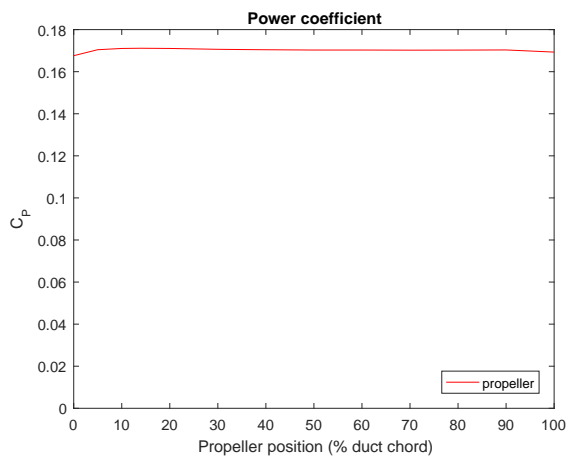


Figure 4.21: Power coefficient C_P vs propeller position

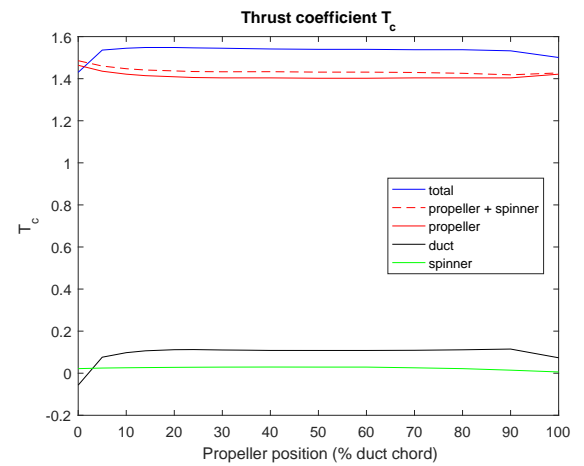


Figure 4.22: Thrust coefficient T_c vs propeller position

It can be seen that the efficiency stays constant over most of the duct chord. This is due to an almost unchanging propeller and total thrust and unchanging power coefficient. The Clark Y airfoil that was used for this analysis has a straight lower surface over most of its chord length. This yields a constant propeller inflow velocity which does not change the propeller thrust. Also the duct thrust is not affected by propeller position, as can be explained by Fig. 4.23. Here it can be seen that after 0.1 c , the suction peak does not increase any further. Only the pressure jump from low to high pressure is postponed downstream. The same can be observed in the pressure distribution around the centerbody in Fig. 4.24. This is probably due to the increasing inflow velocity which decreases the propeller thrust output. However, the duct thrust increases from a slightly negative value, i.e. drag at 0 percent to a maximum value at 25 percent, hence just slightly before the point of maximum thickness of the airfoil. From 25 percent on the propeller and total efficiency both stay fairly constant. Appendix B shows the pressure vectors around the centerbody, duct and propeller.

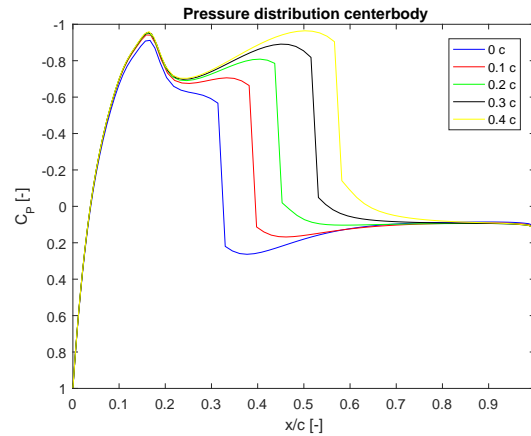
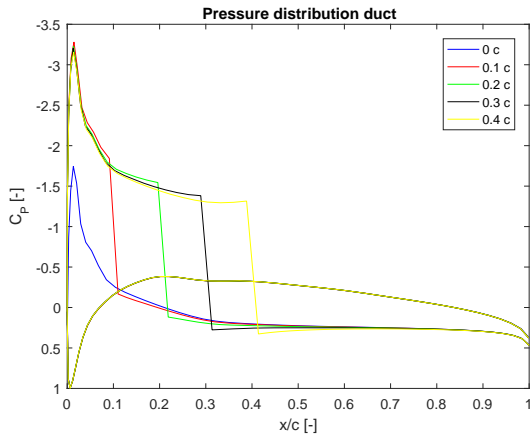


Figure 4.23: Pressure distribution around the duct for variable propeller position

Figure 4.24: Pressure distribution around the centerbody for variable propeller position

4.2.5. ASPECT RATIO

The results for the performance variables as a function of aspect ratio are show in Fig. 4.25, 4.26, 4.27 and 4.28.

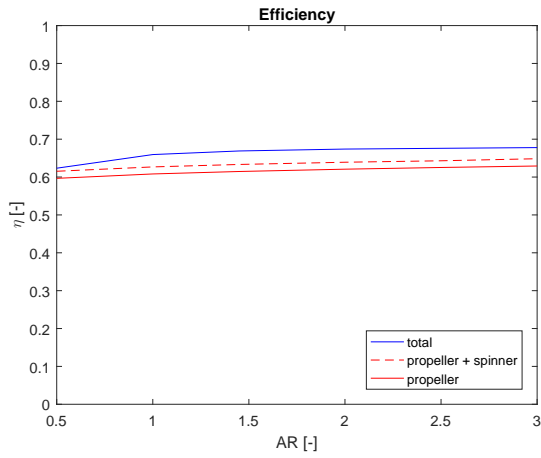


Figure 4.25: Efficiency vs aspect ratio

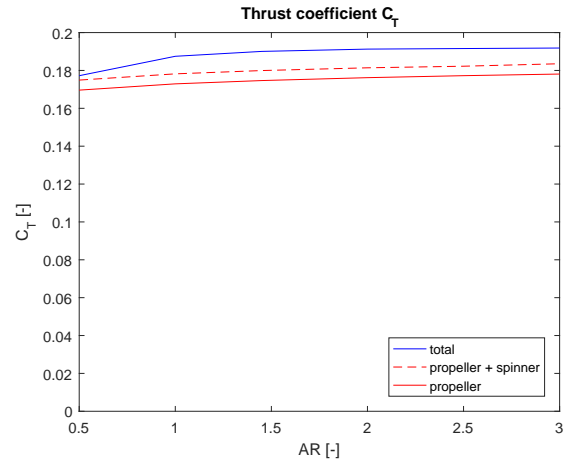


Figure 4.26: Thrust coefficient C_T vs aspect ratio

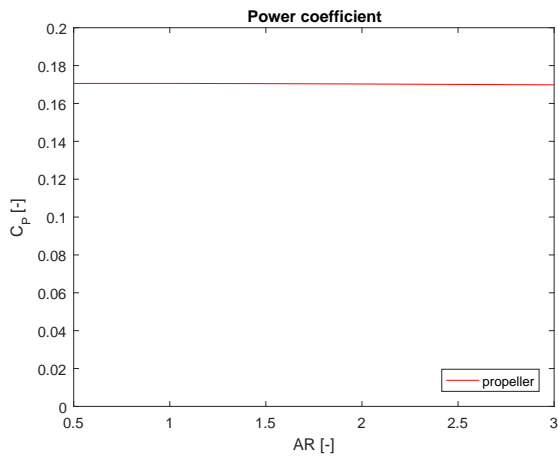


Figure 4.27: Power coefficient C_P vs aspect ratio

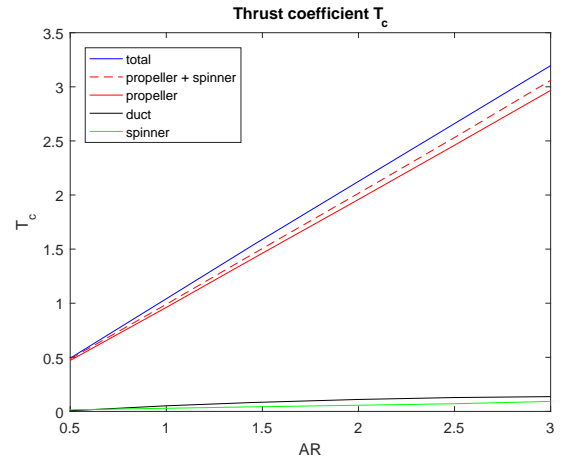


Figure 4.28: Thrust coefficient T_C vs aspect ratio

It can be seen that the efficiency increases with a few percent from aspect ratio 0.5 to 1, the rate of increase then reduces, but the efficiency keeps increasing with increasing aspect ratio. It can be seen this is caused by all thrust components increasing with increasing aspect ratio, while the power coefficient remains constant. The increase in thrust of the duct and centerbody may be caused by a reduction in chord length, which decreases the drag caused by the propeller slipstream. The propeller thrust may slightly increase because of a slight increase in propeller inflow velocity, caused by a shorter convergent cross sectional area as a result of a decrease in duct chord. The shape of the pressure distribution of the duct in Fig. 4.29 is changed in a way which yields a constant area enclosed by the upper and lower surface distribution. The same can be observed for the centerbody in Fig. 4.30. The pressure vectors around the duct, centerbody and propeller are given in Appendix B.

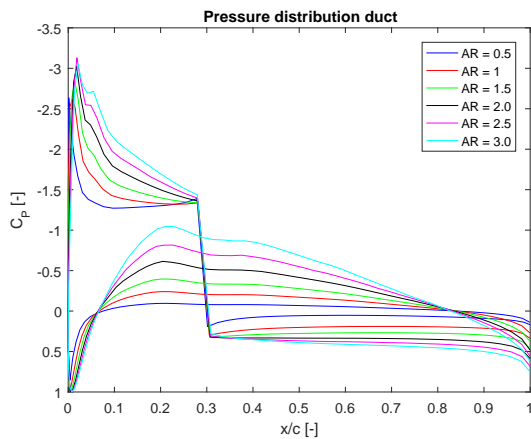


Figure 4.29: Pressure distribution around the duct for variable aspect ratio

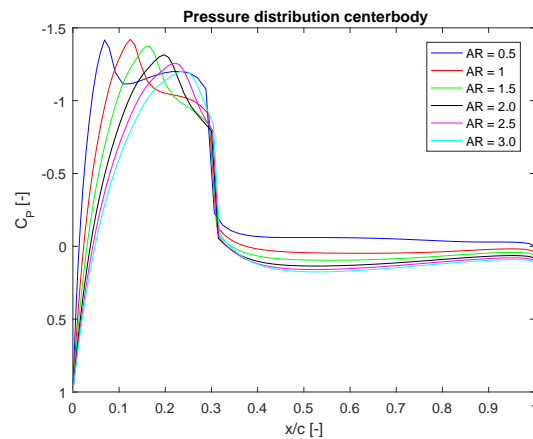


Figure 4.30: Pressure distribution around the centerbody for variable aspect ratio

4.2.6. CAMBER

The results of the performance trends as a function of duct airfoil camber are shown in Fig. 4.31, 4.32, 4.33 and 4.34.

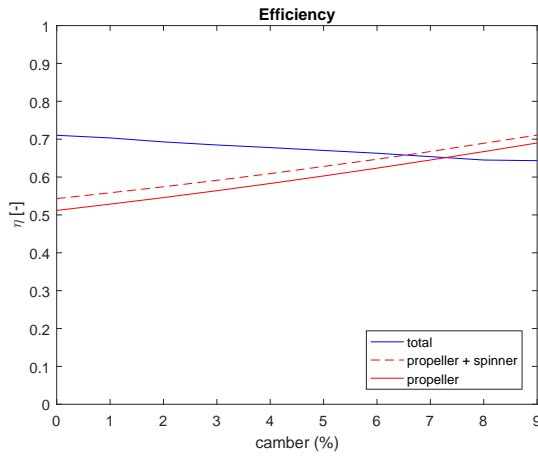


Figure 4.31: Efficiency vs camber

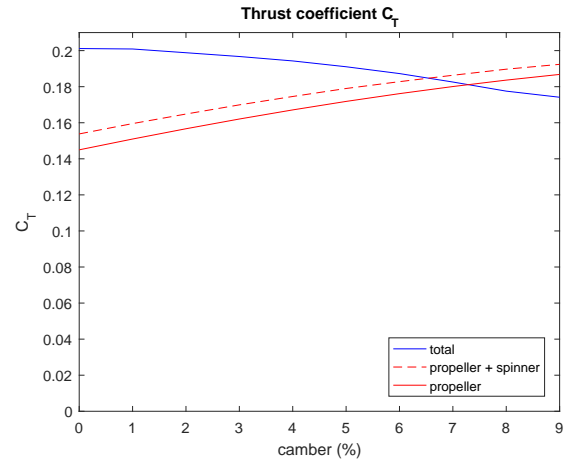


Figure 4.32: Thrust coefficient C_T vs camber

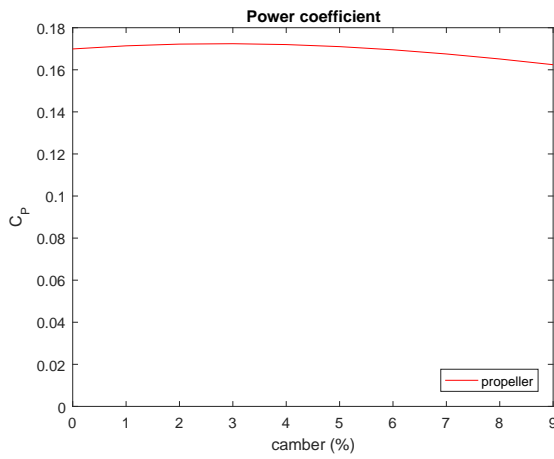


Figure 4.33: Power coefficient C_P vs camber

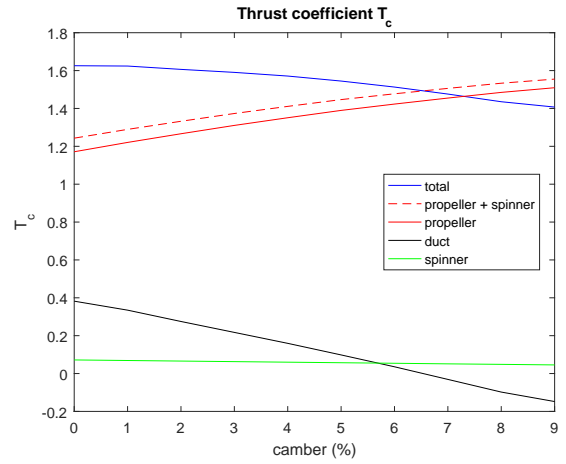


Figure 4.34: Thrust coefficient T_c vs camber

It can be seen that the total efficiency decreases with camber, while the propeller efficiency goes up with camber. At a camber of approximately 7 percent, the efficiencies intersect and the propeller efficiency becomes higher than the total efficiency. This is caused by the fact that the total thrust decreases with camber, while the propeller thrust increases, as can be seen in Fig. At the same time, the power coefficient of the propeller decreases over most of the camber, but at a lower rate, compared to the duct and the propeller. The increase in propeller thrust can be attributed to the larger cross sectional area that results from higher camber and constant propeller location. This increases the propeller inflow velocity, hence causing a higher thrust. The decrease in duct thrust may be due to the duct shape, which yields a lower forward component of the pressure vectors. This is illustrated in Appendix B.

The pressure distributions around the duct and centerbody for varying camber of the duct airfoil are given in Fig. 4.35 and 4.36, respectively.

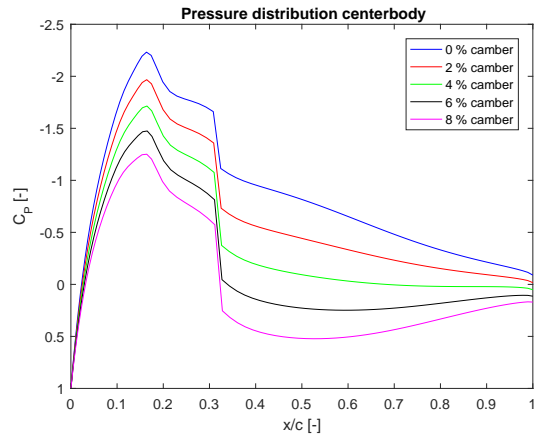
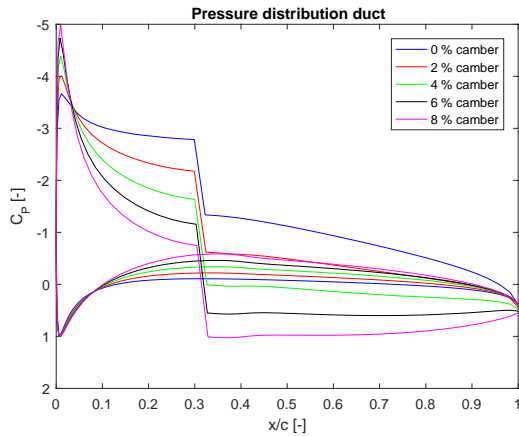


Figure 4.35: Pressure distribution around the duct for variable camber

Figure 4.36: Pressure distribution around the centerbody for variable camber

4.2.7. THICKNESS TO CHORD RATIO

The results of the performance trends versus thickness to chord ratio of the duct airfoil are shown in Fig. 4.37, 4.38, 4.39 and 4.40.

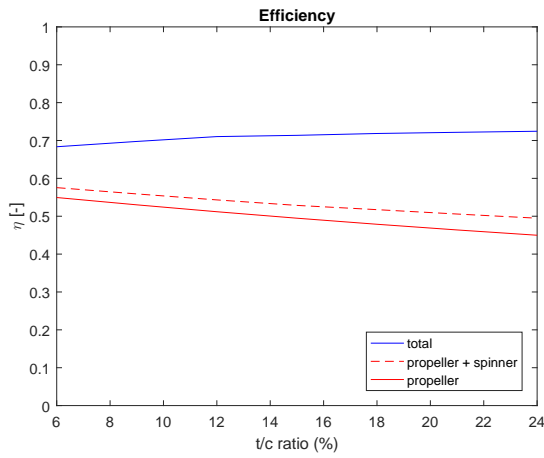


Figure 4.37: Efficiency vs thickness

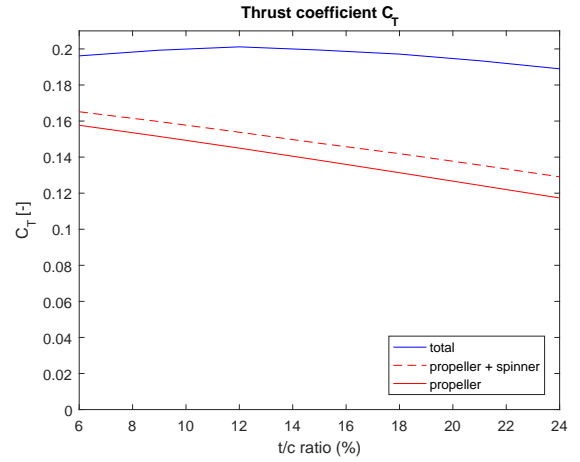


Figure 4.38: Thrust coefficient C_T vs thickness

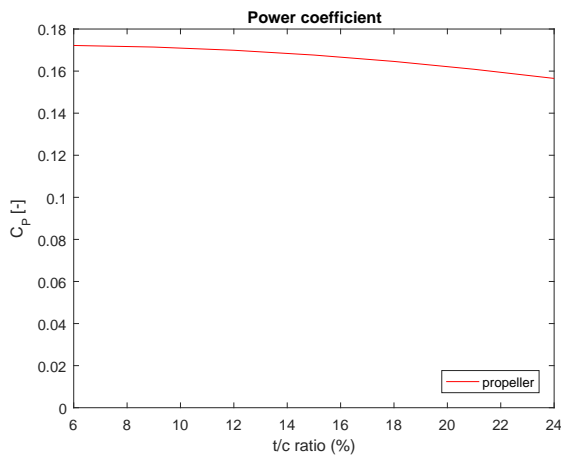


Figure 4.39: Power coefficient C_P vs thickness

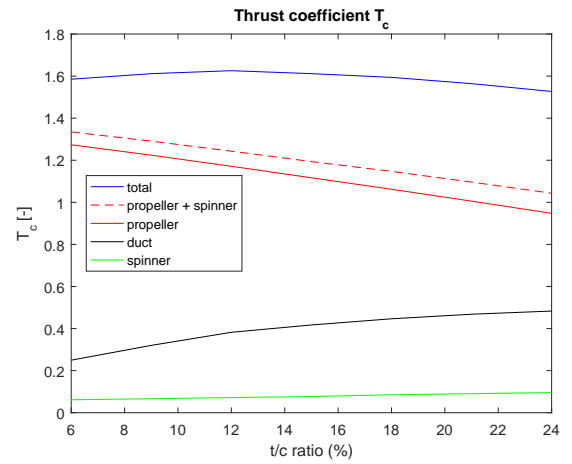


Figure 4.40: Thrust coefficient T_c vs thickness

From the graphs it appears that the total efficiency increases with a few percent for increasing thickness to chord ratios. This is caused by a slight increase, followed by a slight decrease in total thrust, while the power coefficient decreases at a higher rate. The decrease in propeller thrust results possibly from a higher rate of convergence, caused by a larger thickness to chord ratio. The initial increase in duct thrust can be caused by a slightly large duct volume, first causing an increase of forward pressure components, but causing higher drag at larger thicknesses.

The pressure distributions around the duct and centerbody for various thickness to chord ratios of the duct airfoil are given in Fig. 4.41 and 4.42. More detailed pressure vectors can be found in Appendix B.

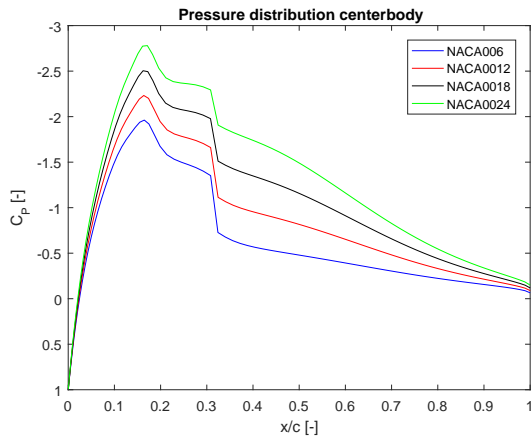


Figure 4.41: Pressure distribution around the duct for variable duct airfoil thickness

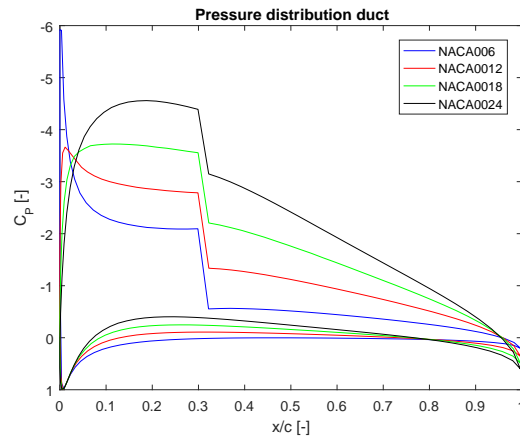


Figure 4.42: Pressure distribution around the centerbody for variable duct airfoil thickness

5

CONCLUSION & RECOMMENDATIONS

5.1. CONCLUSION

The objective of this project was to model the aerodynamic performance of a ducted propeller system, that is critical for propulsion, control and stability under various operational conditions and thrust settings. The model that was constructed aimed on predicting the lift, side force, thrust and drag and their corresponding aerodynamic coefficients under various conditions.

Considering the duct only, it can successfully be modeled as a ring wing in terms of its lift and drag performance under angles of attack by Weissinger's ring wing model. In case of engine out conditions in which the propeller is not windmilling, the lift performance of the duct is not affected significantly by either the feathering propeller or the internal and external strut. Therefore the ring wing lift model can also be applied successfully to the ducted propeller in engine out conditions. This also means that the lift and side force of the duct in power off conditions are only significantly influenced by the airfoil and the aspect ratio. The same model is valid for the side force of the duct under angles of sideslip and Reynolds number effects are negligible. However, in a system of two ducted propellers, the effective sideslip angle is lower compared to the angle of attack because of the sidewash effect that one ducted propeller has on another. Therefore, the derivative of the side force with respect to sideslip is lower compared to the derivative of the lift with respect to angles of attack. The drag of the ducted propeller system in engine out conditions can not be modeled by the sum of the zero lift drag and induced drag of all components, since more complex flow aerodynamics and interference effects yield significantly higher drag.

When the propeller is on, the lift of the ducted propeller is increased as thrust is increased. The increase in lift consists of a change in aerodynamic performance of the duct, a lifting component of the combined propeller and centerbody thrust and a lifting component of the propeller normal force. No general relation can be found between the thrust setting and the change in lifting performance of the duct, since this heavily depends on the duct shape. The same trend is observed for side force under sideslip angles. The effect of thrust settings on the drag is not easy to model, especially since it is difficult to measure drag without thrust contributions. It may be stated that overall drag increases because of higher component velocities and higher levels of flow disturbance, due to swirl in the slipstream.

The stall angle and corresponding maximum lift coefficient are heavily dependent on the airfoil of the duct and the overall ducted propeller configuration, such that no general relations can be drawn on it. Higher thrust increases the onset of stall of a ducted propeller, compared to power off conditions, and consequently the maximum lift coefficient. However, higher speeds may decrease the stall angle.

Deflections of horizontal and vertical control surfaces increase the lift and side force of a ducted propeller by an approximately constant value, independent of angles of incidence. However, the effectiveness of these elevators and rudders are lower than those of conventional elevators and rudders, which may be attributed to differences in inflow velocities at the trailing edge of the ducted propeller compared to the horizontal and vertical tail trailing edge of a conventional aircraft. After the onset of stall of the ducted propeller, the control surfaces do not lose effectiveness, indicating that total system stall does not influence the flow on the control surfaces significantly. When control surfaces have partially stalled themselves, they yield a smaller constant lift increase, indicating loss of effectiveness. Relations between ducted propeller geometry and the onset of elevator and rudder stall are difficult to draw, since they depend on many aerodynamic phenomena. The

drag and consequent loss in net thrust caused by control surface deflections is not constant over the range of incidence angles, nor is the derivative of the drag with respect to control surface deflections linear. Several aerodynamic phenomena, heavily depending on the geometry of the system, may be contributing to this.

Finally, speed and consequently advance ratio are the most critical operational conditions affecting the aerodynamic performance. It is clear that the duct increases the total thrust to power ratio at rather low speeds, after which it decreases total thrust to power ratio. Reynolds number effects are much less pronounced become lower as Reynolds number is increased. Duct shape and aspect ratio are the most critical geometric parameters affecting performance, where higher aspect ratio and thickness are beneficial for total thrust to power ratio, whereas this is decreased by camber.

5.2. RECOMMENDATIONS

To study the effect of the propeller on the duct aerodynamics and particularly its lift performance, CFD simulations should be executed to obtain insight in the effect of the propeller on the pressure distribution around the duct for various duct shapes under angles of attack.

Furthermore, advanced wind tunnel tests, including multiple models of various scales and geometries can be executed to allow for higher levels of analytical and numerical model validation. These tests should be done under a broader range of angles of incidence with smaller intervals, to obtain more insight in the onset and development of stall.

Finally, control surface effectiveness can possibly be improved by investigating several other control surface designs, such as deflectable parts of the duct.

A

APPENDIX A

Throughout the years several experiments have been carried out with ducted propellers under angles of attack. Some of these experiments give insight in the influence of the propeller on the lift generation of the ducted fan. However, no analytical models for the propeller effect on ducted propeller lift have been constructed so far.

One study of the aerodynamic loads on a small scale ducted propeller under angles of attack was done by Grunwald & Goodson [2]. Lift curves were constructed with the power on, the propeller windmilling and the power off. Another ducted propeller wind tunnel test was done by Mort & Gamse [1], who studied a larger model. Lift curves were constructed with the power off and the propeller removed. By comparing the power on and power off lift curves of these experiments a trend is attempted to be found between the increase in lift curve slope and the thrust setting. This has been done by taking the total thrust coefficient T_c at axial inflow conditions. Although the total thrust in axial inflow conditions is not the same as the total thrust over the range of angles of attack, because of changes in both duct and propeller performance, the assumption of a non varying total thrust is used in the construction of the propeller lift model. The total lift curve at a specific thrust setting is reduced by the vertical component of the assumed non varying total thrust at each angle of attack to obtain a lift curve that represents the duct only, including the influence of the propeller, but without the lifting total thrust component of the propeller and duct. The following assumptions have been made in this process:

- The combined propeller, centerbody and duct thrust $T_{propcbduct}$ is non varying over the range of angles of attack. This is based on the fact that for an axisymmetric duct and particularly for a symmetrical duct airfoil, the pressure on the upper surface of the duct decreases with angle of attack, whereas the pressure on the lower surface of the airfoil increases with angle of attack. This yields a pressure increase on the upper inner duct surface and a pressure decrease on the lower inner duct surface. This means that the flow velocity increases with respect to the axial value on the upper inner surface and it decreases on the lower inner surface. However, it is assumed that the resultant/average of this velocity field over the propeller disk stays constant, such that the propeller sees the same average inflow velocity over the range of angles of attack, thus yielding the same thrust
- The ratio of propeller thrust to total thrust is different for each design and advance ratio. However it is assumed that the relation between the factor k_{prop} vs $T_{propcbduct}$ and the factor k_{prop} vs T_{prop} is approximately similar, such that $T_{propcbduct}$ can be used in all cases
- It is assumed that the component drag of the model by Grunwald and Goodson and Mort and Gamse are approximately the same, even though the geometry differs.
- The propeller removed condition and propeller off condition, i.e. feathering condition, are equal, or the propeller drag in Grunwald and Goodson compensates for the exit vane drag in Mort and Gamse

Applying this method, the "propeller reduced" lift coefficient becomes the following:

$$C_{L,red} = C_{L,total} - T_c \cdot \sin(\alpha) \quad (A.1)$$

By doing this, also a "reduced" lift curve $C_{L,red}$ is obtained. Determining $C_{L,red}$ at different angles of attack for the experimental data from [2] and [1], the lift curves in Fig. A.1 are obtained.

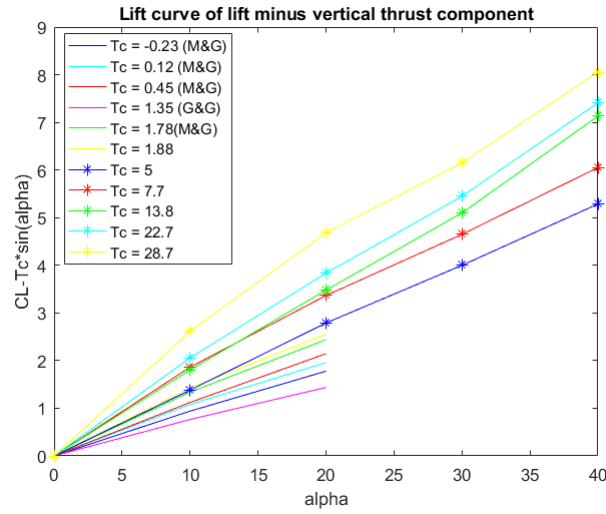


Figure A.1: Thrust reduced lift curves from experimental data

As can be seen in Fig. A.1 the lift curves are not completely straight. Therefore the average of the lift curve slope is taken to obtain the thrust reduced lift curve slope $C_{L\alpha,red}$.

Defining a factor k_{prop} , which relates the lift curve slope of the duct only/propeller off condition to the lift curve slope of the duct only/propeller on condition, the following equation is obtained:

$$C_{L\alpha,duct,on} = (1 + k_{prop}) C_{L\alpha,duct} \quad (A.2)$$

Hence, the factor k can be modeled by:

$$k = \frac{C_{L\alpha,duct,on}}{C_{L\alpha,duct}} - 1 \quad (A.3)$$

Determining the factor k for the different lift curves from the experiments from [2] and [1] and plotting this factor against the corresponding total axial thrust coefficient T_c , yields a trend that best fits the relation between the propeller thrust coefficient T_c and factor k given by:

This factor k_{prop} is a function of the propeller and centerbody thrust coefficient $T_{c_{propcb}}$ and is given by:

$$k = 0.2 \cdot \sqrt{T_{c_{propcb}}} \quad (A.4)$$

The comparison between this approximation and the experimental data points is illustrated in the following figure:

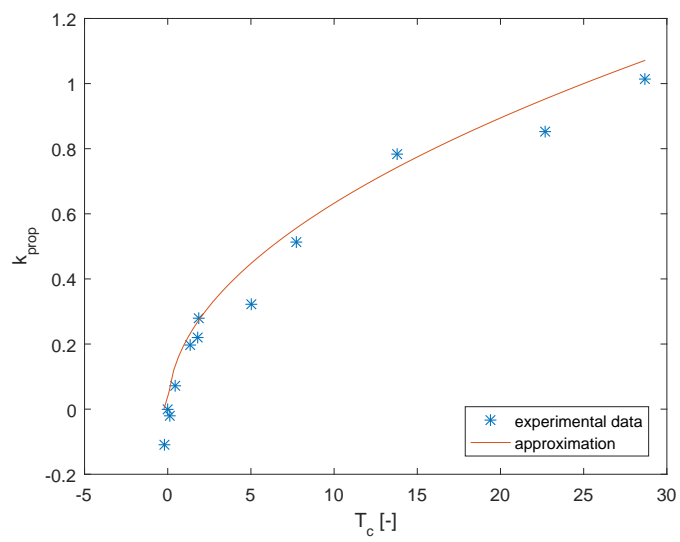


Figure A.2: k factor vs thrust coefficient

B

APPENDIX B

B.1. REYNOLDS NUMBER

Considering the normal pressure vectors around the duct, centerbody and propeller, it can be seen that these also remain unchanged over the Reynolds number range.

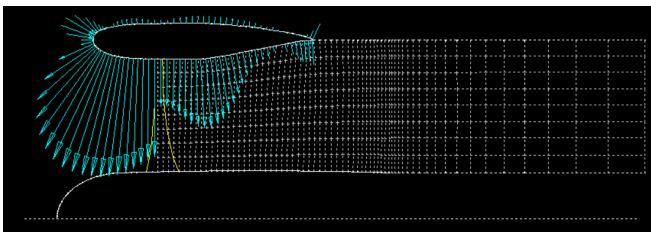


Figure B.1: Pressure vectors around the duct, $Re = 109,340$

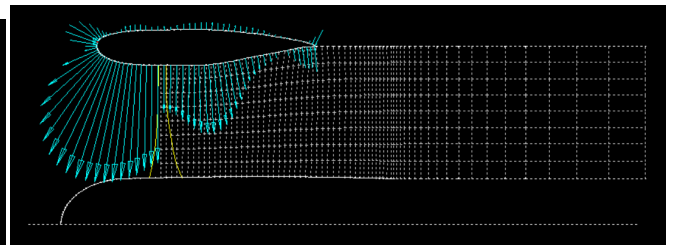


Figure B.2: Pressure vectors around the duct, $Re = 550,000$

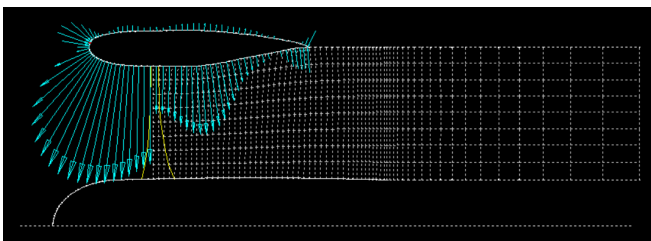


Figure B.3: Pressure vectors around the duct, $Re = 1,639,300$

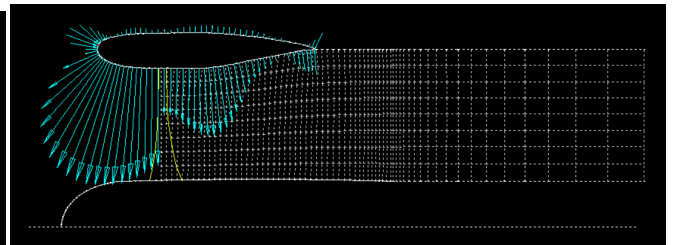
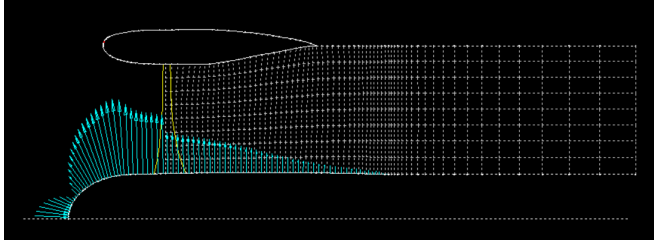
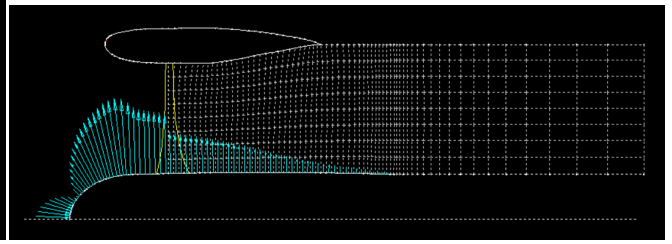
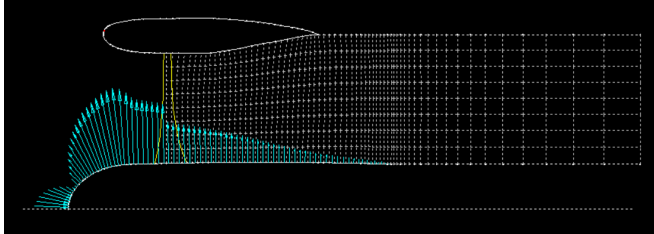
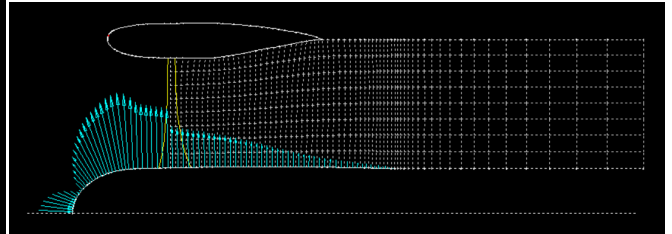
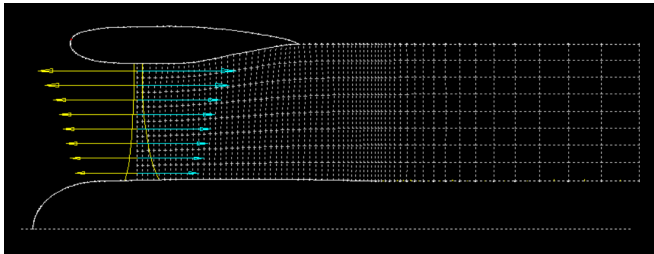
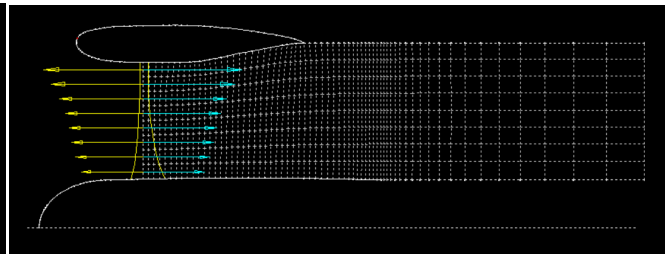
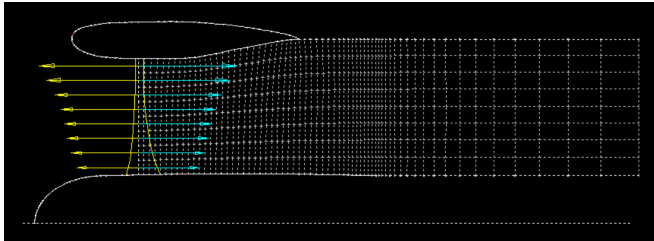
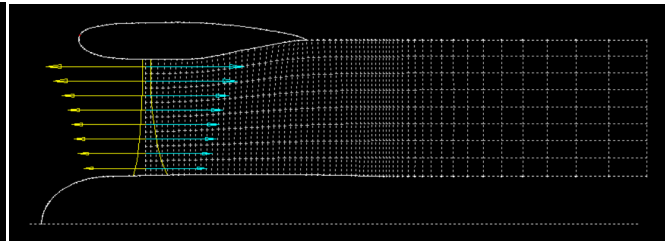


Figure B.4: Pressure vectors around the duct, $Re = 4,465,800$

Figure B.5: Pressure vectors around the centerbody, $Re = 109,340$ Figure B.6: Pressure vectors around the centerbody, $Re = 550,000$ Figure B.7: Pressure vectors around the centerbody, $Re = 1,639,300$ Figure B.8: Pressure vectors around the centerbody, $Re = 4,465,800$ Figure B.9: Pressure vectors of the propeller, $Re = 109,340$ Figure B.10: Pressure vectors of the propeller, $Re = 550,000$ Figure B.11: Pressure vectors of the propeller, $Re = 1,639,300$ Figure B.12: Pressure vectors of the propeller, $Re = 4,465,800$

B.2. ADVANCE RATIO

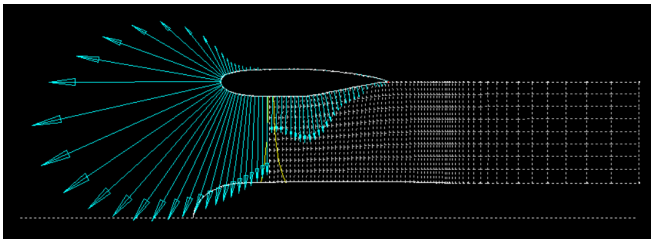


Figure B.13: Pressure vectors around the duct, $J = 0$

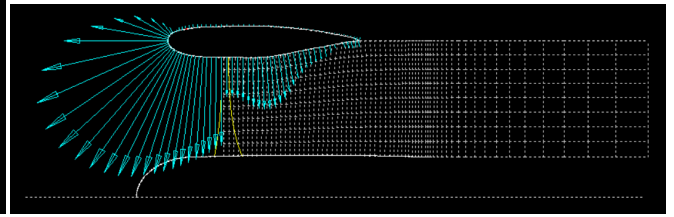


Figure B.14: Pressure vectors around the duct, $J = 0.2$

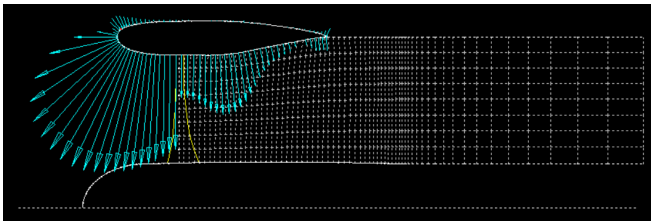


Figure B.15: Pressure vectors around the duct, $J = 0.4$

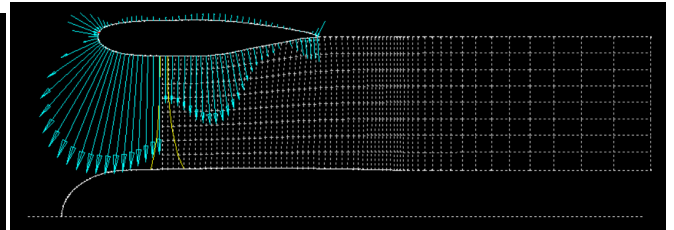


Figure B.16: Pressure vectors around the duct, $J = 0.6$

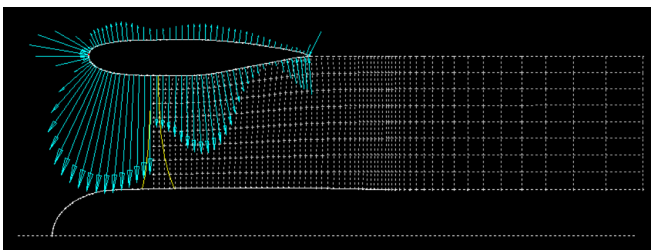


Figure B.17: Pressure vectors around the duct, $J = 0.8$

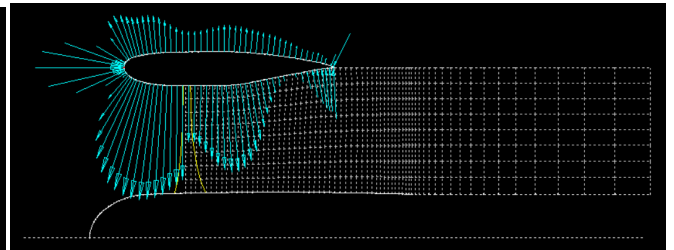


Figure B.18: Pressure vectors around the duct, $J = 1.0$

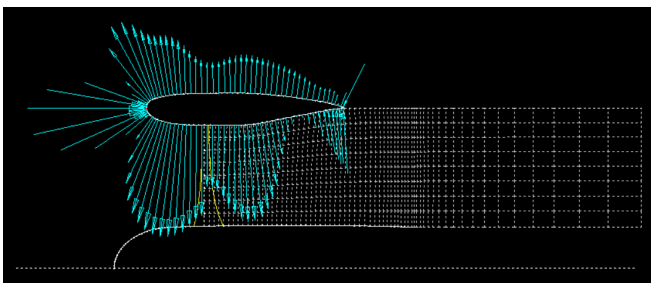


Figure B.19: Pressure vectors around the duct, $J = 1.2$

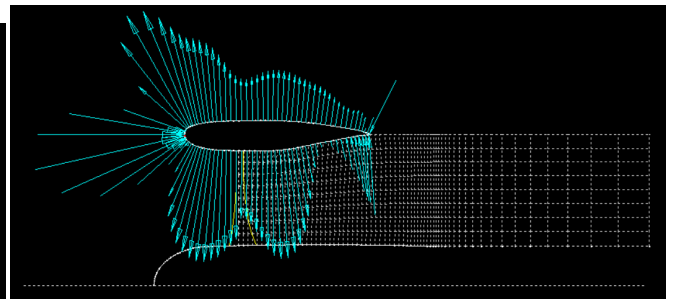
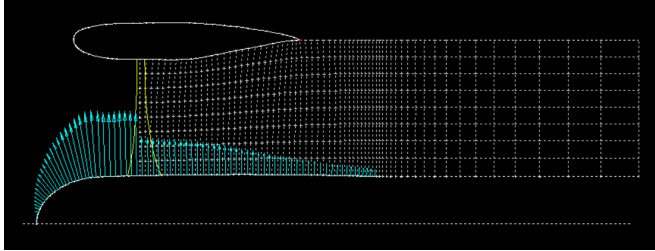
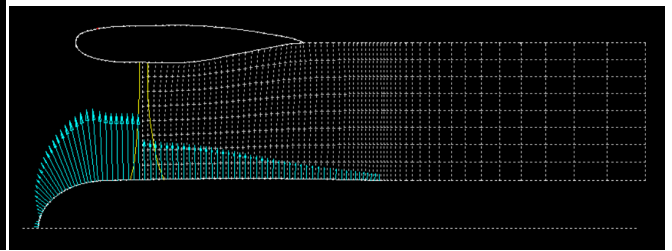
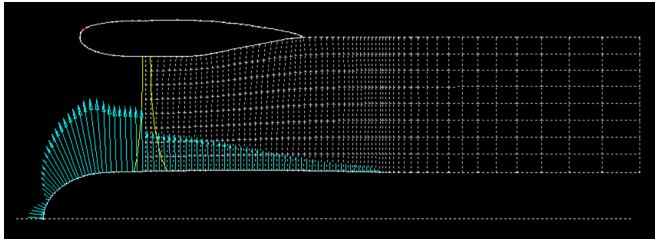
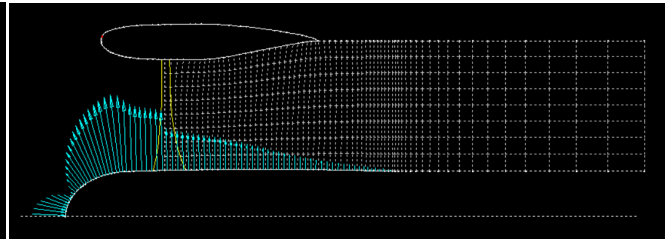
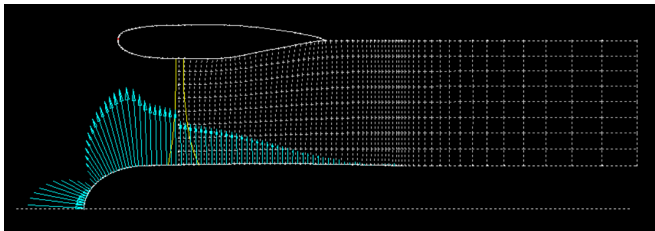
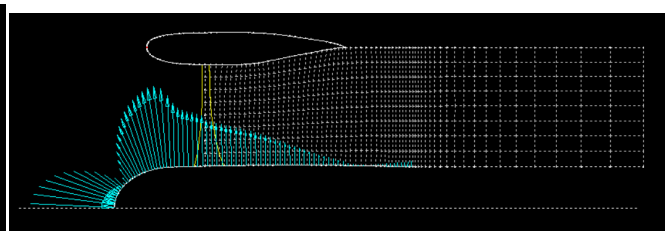
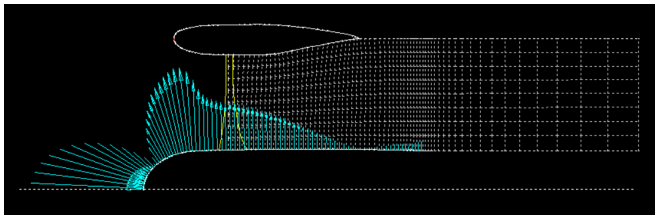
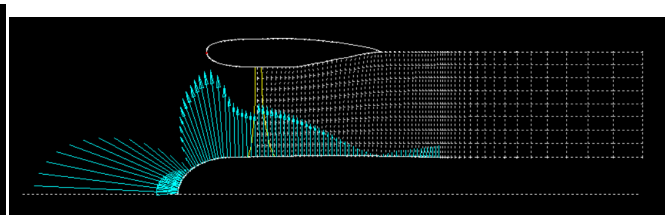
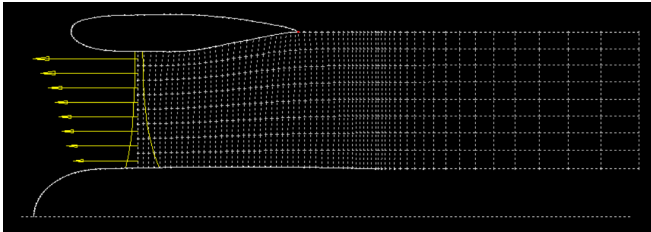
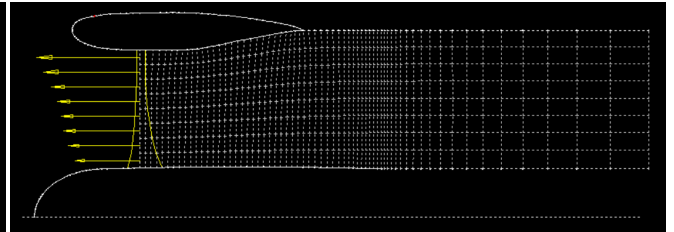
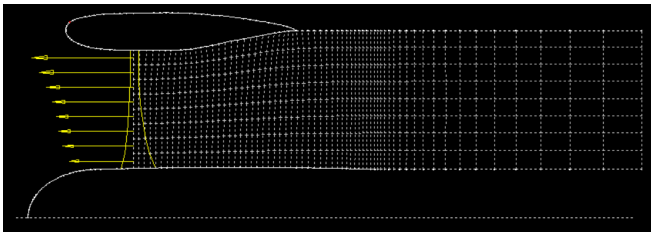
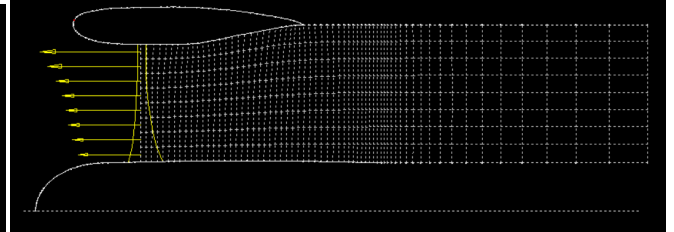
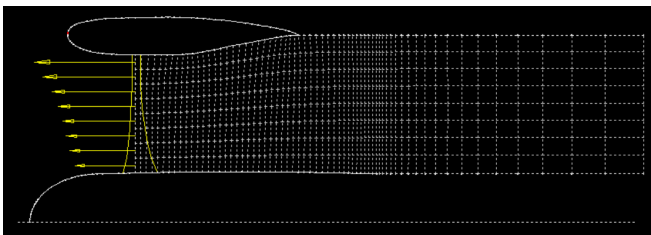
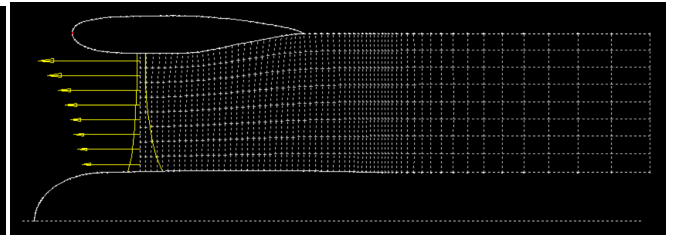
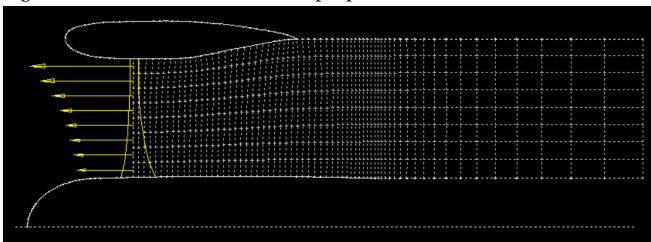
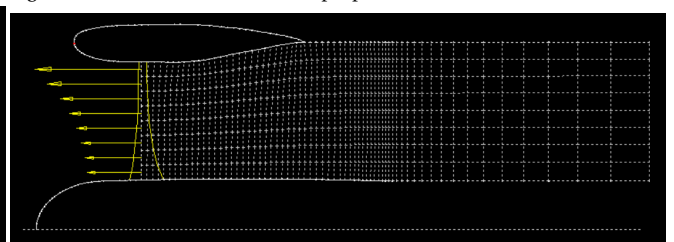


Figure B.20: Pressure vectors around the duct, $J = 1.4$

Figure B.21: Pressure vectors around the centerbody, $J = 0$ Figure B.22: Pressure vectors around the centerbody, $J = 0.2$ Figure B.23: Pressure vectors around the centerbody, $J = 0.4$ Figure B.24: Pressure vectors around the centerbody, $J = 0.6$ Figure B.25: Pressure vectors around the centerbody, $J = 0.8$ Figure B.26: Pressure vectors around the centerbody, $J = 1.0$ Figure B.27: Pressure vectors around the centerbody, $J = 1.2$ Figure B.28: Pressure vectors around the centerbody, $J = 1.4$

Figure B.29: Pressure vectors of the propeller, $J = 0$ Figure B.30: Pressure vectors of the propeller, $J = 0.2$ Figure B.31: Pressure vectors of the propeller, $J = 0.4$ Figure B.32: Pressure vectors of the propeller, $J = 0.6$ Figure B.33: Pressure vectors of the propeller, $J = 0.8$ Figure B.34: Pressure vectors of the propeller, $J = 1.0$ Figure B.35: Pressure vectors of the propeller, $J = 1.2$ Figure B.36: Pressure vectors of the propeller, $J = 1.4$

B.3. TIP CLEARANCE

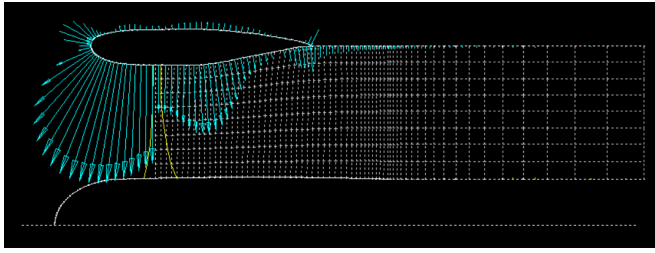


Figure B.37: Pressure vectors around the duct, $tc = 0\%$

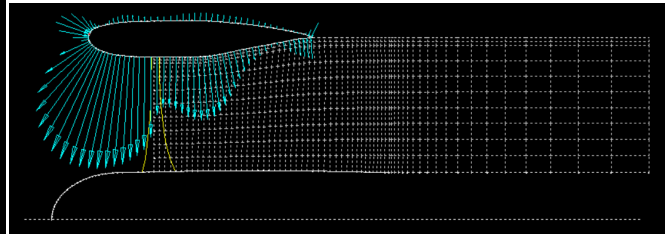


Figure B.38: Pressure vectors around the duct, $tc = 1\%$

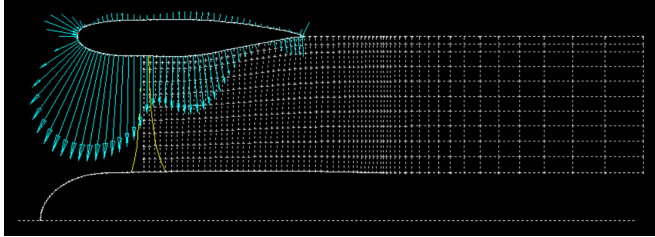


Figure B.39: Pressure vectors around the duct, $tc = 2\%$

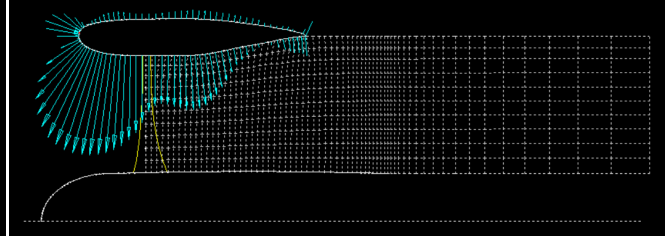


Figure B.40: Pressure vectors around the duct, $tc = 3\%$

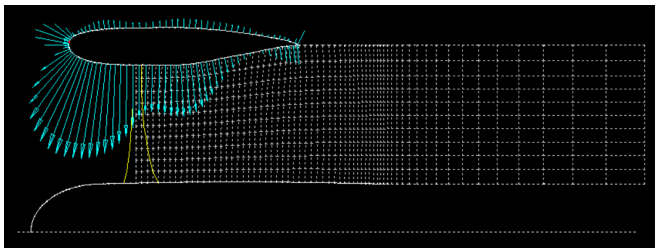


Figure B.41: Pressure vectors around the duct, $tc = 4\%$

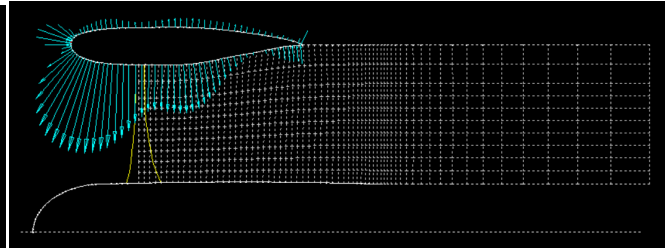


Figure B.42: Pressure vectors around the duct, $tc = 5\%$

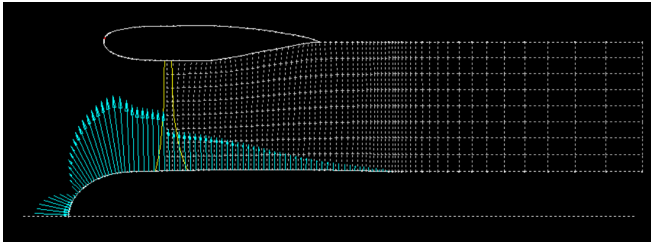


Figure B.43: Pressure vectors around the centerbody, $tc = 0\%$

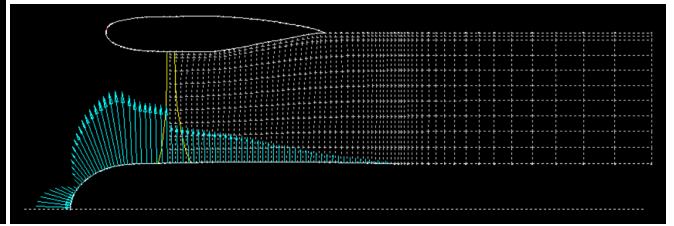


Figure B.44: Pressure vectors around the centerbody, $tc = 1\%$

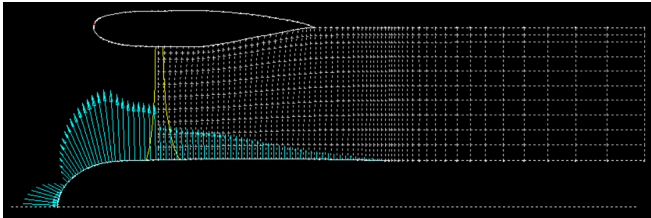


Figure B.45: Pressure vectors around the centerbody, $tc = 2\%$

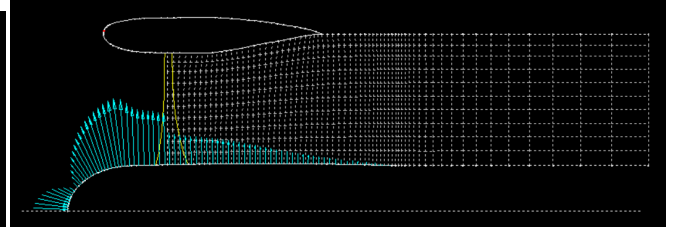


Figure B.46: Pressure vectors around the centerbody, $tc = 3\%$

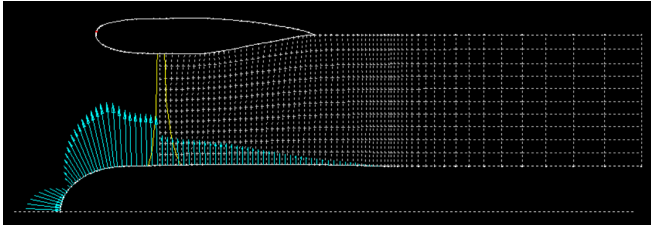


Figure B.47: Pressure vectors around the centerbody, $tc = 4\%$

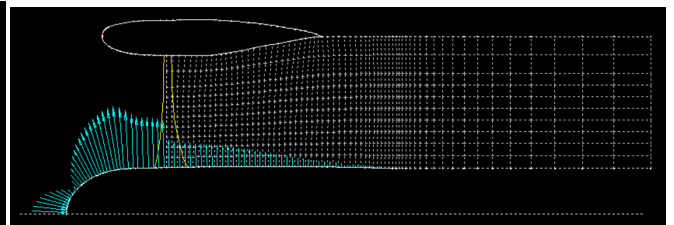


Figure B.48: Pressure vectors around the centerbody, $tc = 5\%$

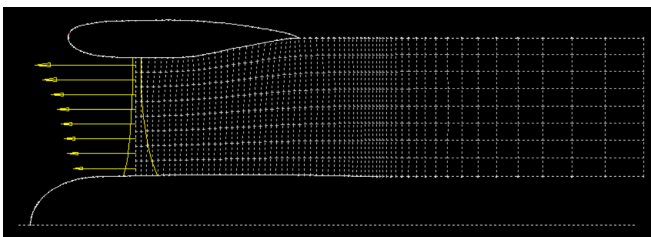


Figure B.49: Pressure vectors of the propeller, $tc = 0\%$

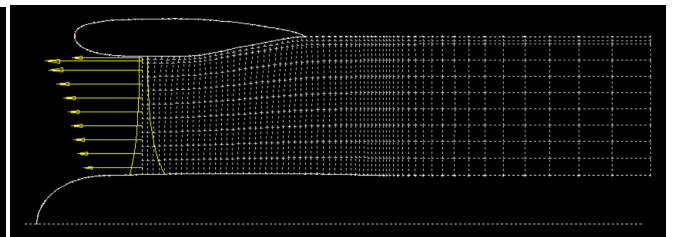


Figure B.50: Pressure vectors of the propeller, $tc = 1\%$

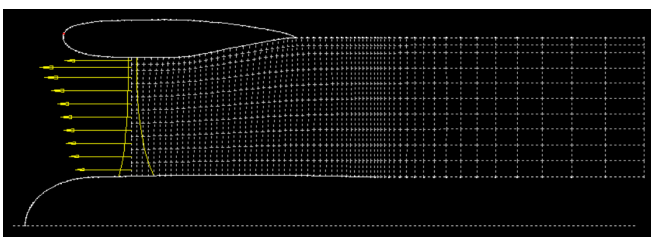


Figure B.51: Pressure vectors of the propeller, $tc = 2\%$

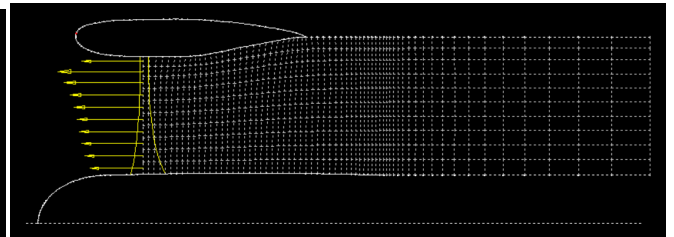


Figure B.52: Pressure vectors of the propeller, $tc = 3\%$

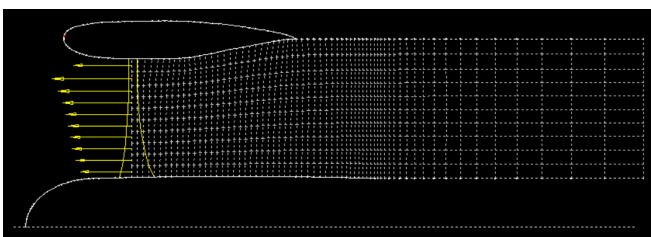


Figure B.53: Pressure vectors of the propeller, $tc = 4\%$

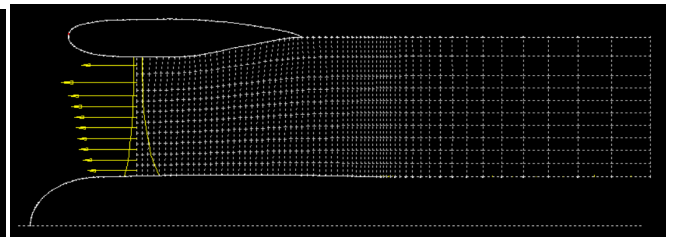
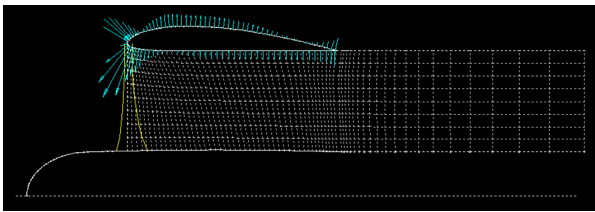
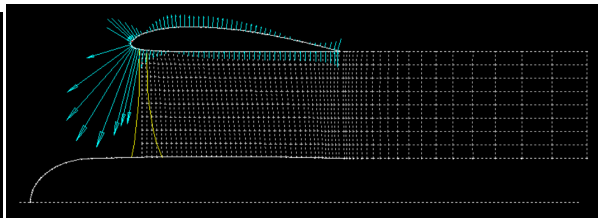
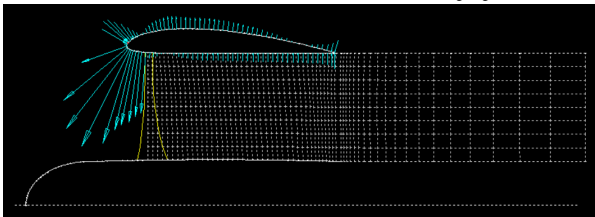
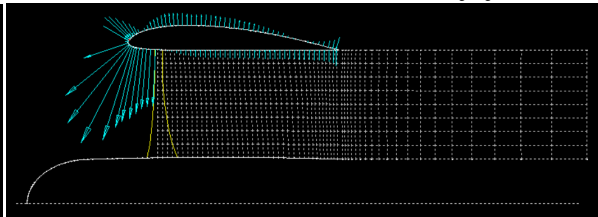
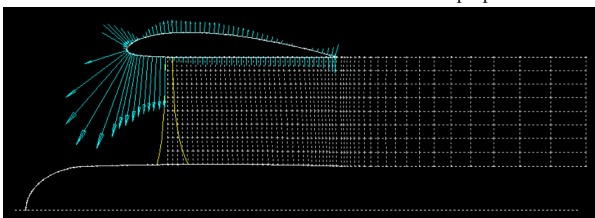
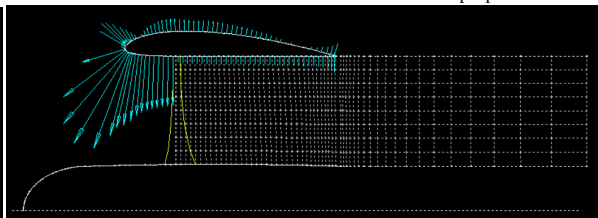
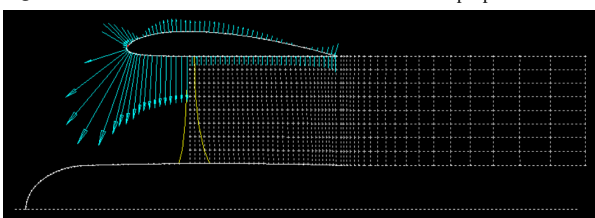
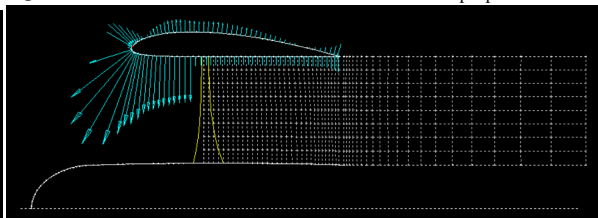
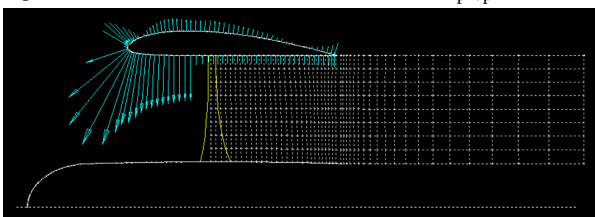
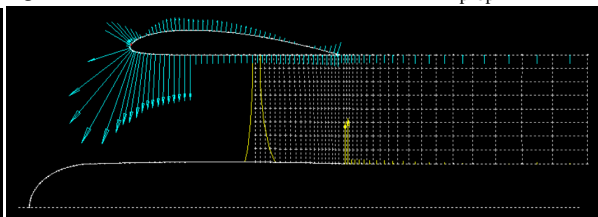
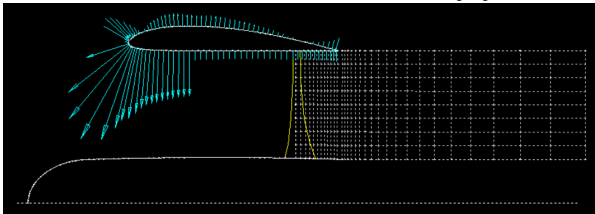
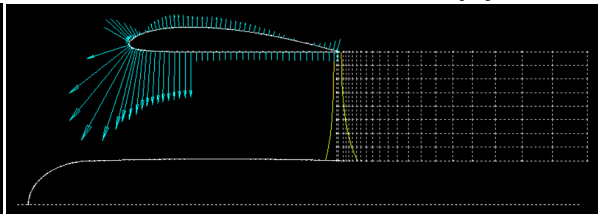
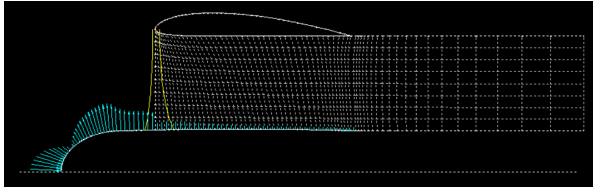
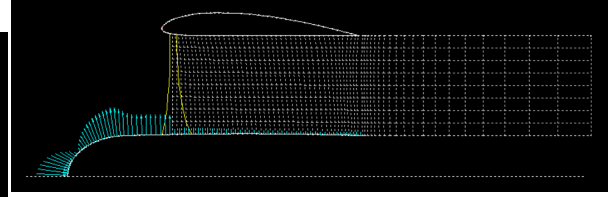
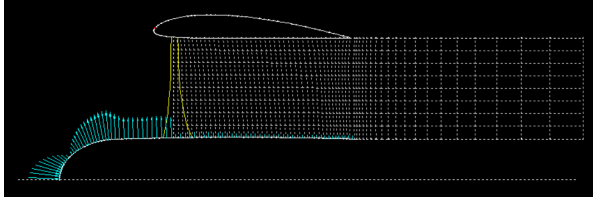
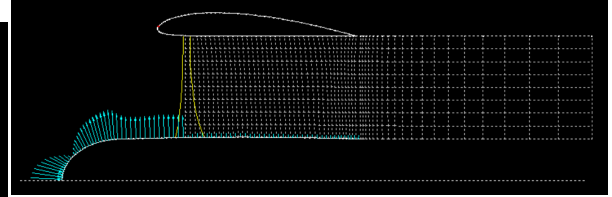
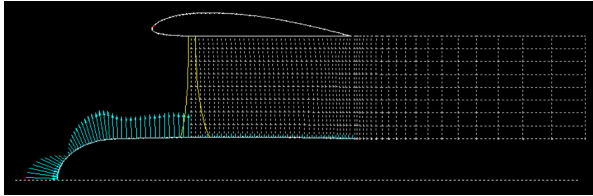
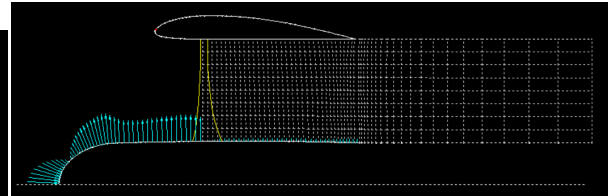
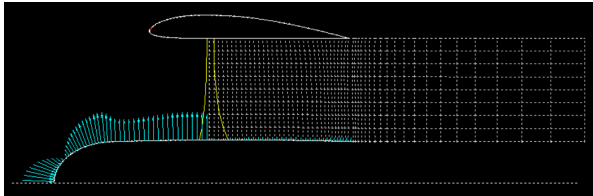
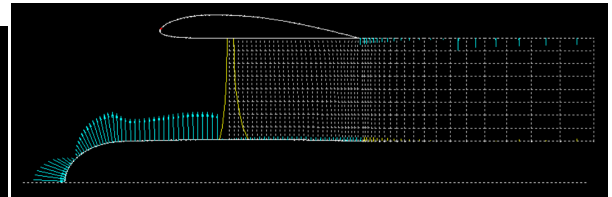
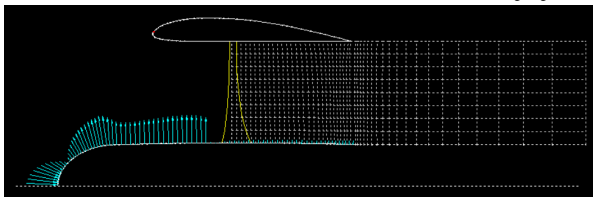
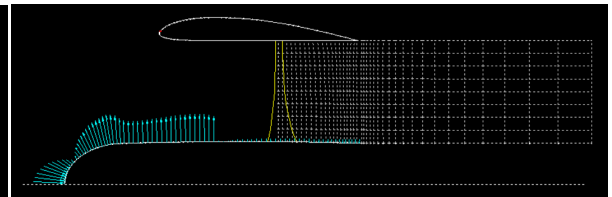
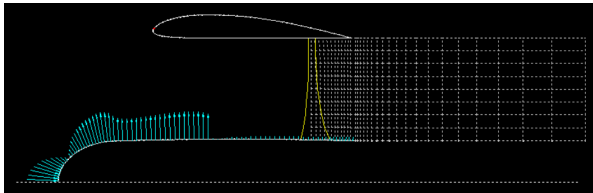
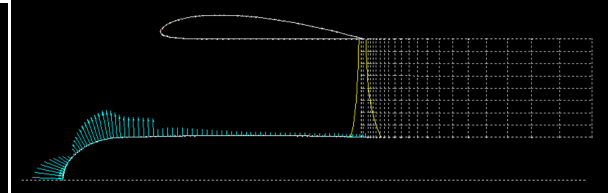
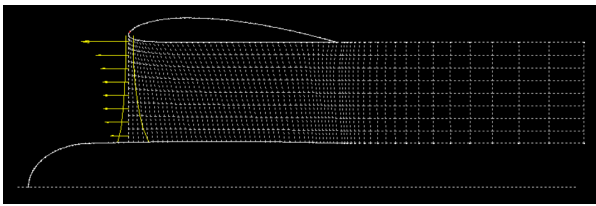
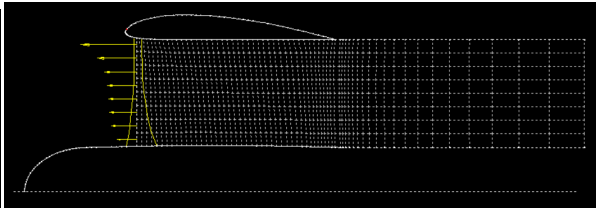
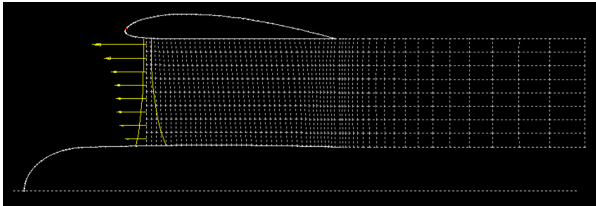
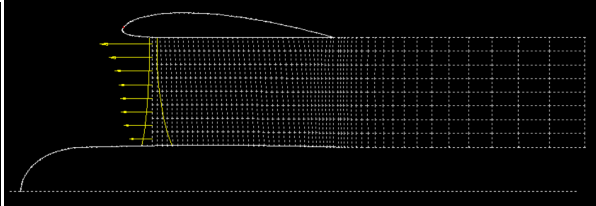
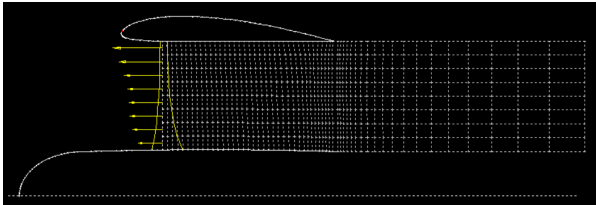
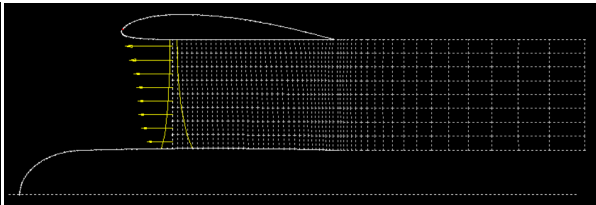
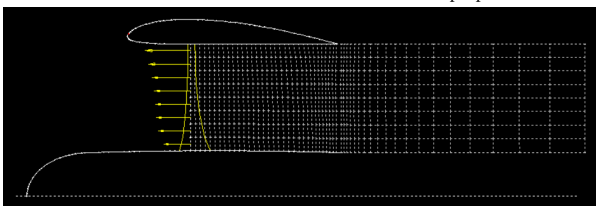
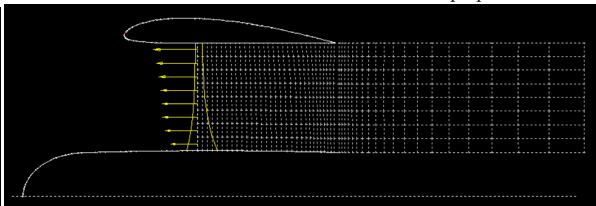
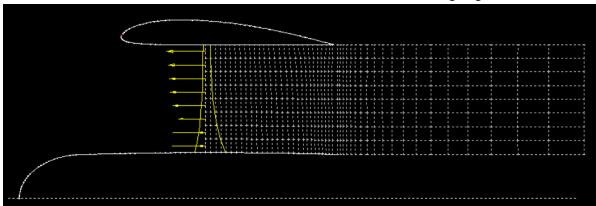
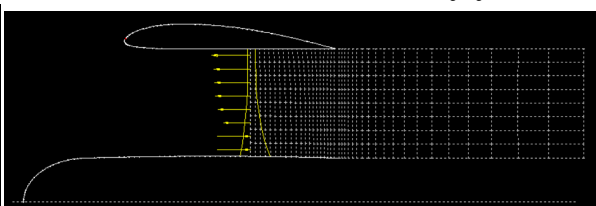
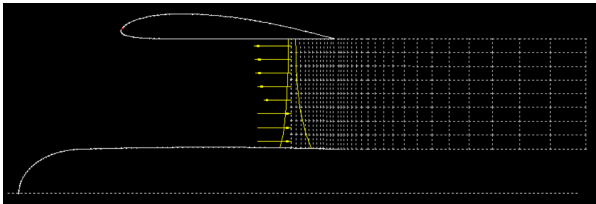
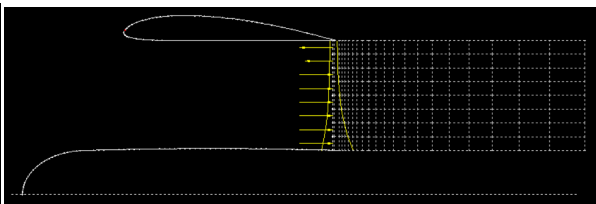


Figure B.54: Pressure vectors of the propeller, $tc = 5\%$

B.4. PROPELLER LONGITUDINAL POSITION

Figure B.55: Pressure vectors around the duct, $(x/c)_{\text{prop}} = 0$ Figure B.56: Pressure vectors around the duct, $(x/c)_{\text{prop}} = 0.05$ Figure B.57: Pressure vectors around the duct, $(x/c)_{\text{prop}} = 0.1$ Figure B.58: Pressure vectors around the duct, $(x/c)_{\text{prop}} = 0.14$ Figure B.59: Pressure vectors around the duct, $(x/c)_{\text{prop}} = 0.2$ Figure B.60: Pressure vectors around the duct, $(x/c)_{\text{prop}} = 0.24$ Figure B.61: Pressure vectors around the duct, $(x/c)_{\text{prop}} = 0.3$ Figure B.62: Pressure vectors around the duct, $(x/c)_{\text{prop}} = 0.35$ Figure B.63: Pressure vectors around the duct, $(x/c)_{\text{prop}} = 0.4$ Figure B.64: Pressure vectors around the duct, $(x/c)_{\text{prop}} = 0.6$ Figure B.65: Pressure vectors around the duct, $(x/c)_{\text{prop}} = 0.8$ Figure B.66: Pressure vectors around the duct, $(x/c)_{\text{prop}} = 1.0$

Figure B.67: Pressure vectors around the centerbody, $(x/c)_{\text{prop}} = 0$ Figure B.68: Pressure vectors around the centerbody, $(x/c)_{\text{prop}} = 0.05$ Figure B.69: Pressure vectors around the centerbody, $(x/c)_{\text{prop}} = 0.1$ Figure B.70: Pressure vectors around the centerbody, $(x/c)_{\text{prop}} = 0.14$ Figure B.71: Pressure vectors around the centerbody, $(x/c)_{\text{prop}} = 0.2$ Figure B.72: Pressure vectors around the centerbody, $(x/c)_{\text{prop}} = 0.24$ Figure B.73: Pressure vectors around the centerbody, $(x/c)_{\text{prop}} = 0.3$ Figure B.74: Pressure vectors around the centerbody, $(x/c)_{\text{prop}} = 0.35$ Figure B.75: Pressure vectors around the centerbody, $(x/c)_{\text{prop}} = 0.4$ Figure B.76: Pressure vectors around the centerbody, $(x/c)_{\text{prop}} = 0.6$ Figure B.77: Pressure vectors around the centerbody, $(x/c)_{\text{prop}} = 0.8$ Figure B.78: Pressure vectors around the centerbody, $(x/c)_{\text{prop}} = 1.0$

Figure B.79: Pressure vectors of the propeller, $(x/c)_{\text{prop}} = 0$ Figure B.80: Pressure vectors of the propeller, $(x/c)_{\text{prop}} = 0.05$ Figure B.81: Pressure vectors of the propeller, $(x/c)_{\text{prop}} = 0.1$ Figure B.82: Pressure vectors of the propeller, $(x/c)_{\text{prop}} = 0.14$ Figure B.83: Pressure vectors of the propeller, $(x/c)_{\text{prop}} = 0.2$ Figure B.84: Pressure vectors of the propeller, $(x/c)_{\text{prop}} = 0.24$ Figure B.85: Pressure vectors of the propeller, $(x/c)_{\text{prop}} = 0.3$ Figure B.86: Pressure vectors of the propeller, $(x/c)_{\text{prop}} = 0.35$ Figure B.87: Pressure vectors of the propeller, $(x/c)_{\text{prop}} = 0.4$ Figure B.88: Pressure vectors of the propeller, $(x/c)_{\text{prop}} = 0.6$ Figure B.89: Pressure vectors of the propeller, $(x/c)_{\text{prop}} = 0.8$ Figure B.90: Pressure vectors of the propeller, $(x/c)_{\text{prop}} = 1$

B.4.1. ASPECT RATIO

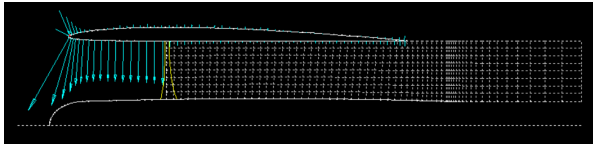


Figure B.91: Pressure vectors around the duct, $AR_{\text{duct}} = 0.5$

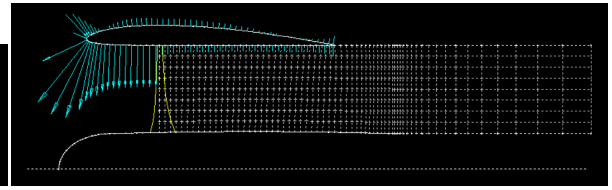


Figure B.92: Pressure vectors around the duct, $AR_{\text{duct}} = 1$

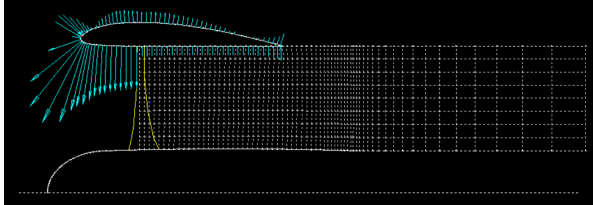


Figure B.93: Pressure vectors around the duct, $AR_{\text{duct}} = 1.45$

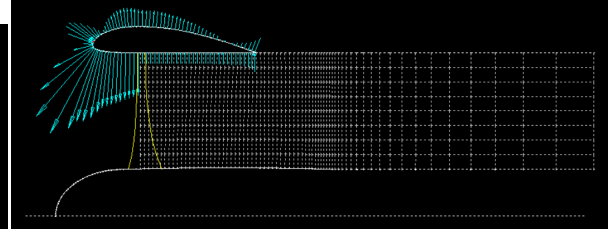


Figure B.94: Pressure vectors around the duct, $AR_{\text{duct}} = 2$

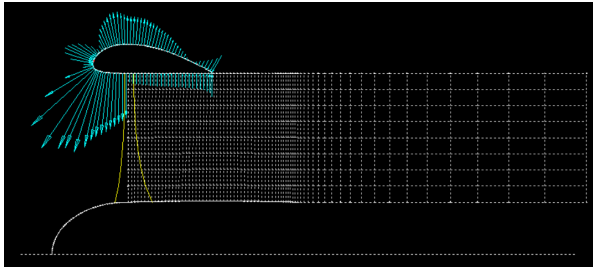


Figure B.95: Pressure vectors around the duct, $AR_{\text{duct}} = 3$

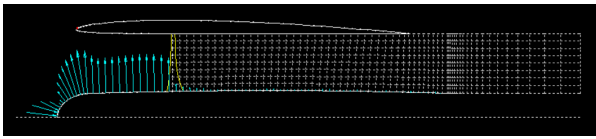


Figure B.96: Pressure vectors around the centerbody, $AR_{duct} = 0.5$

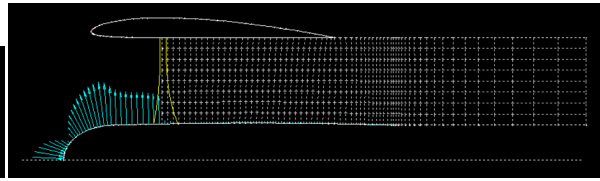


Figure B.97: Pressure vectors around the centerbody, $AR_{duct} = 1$

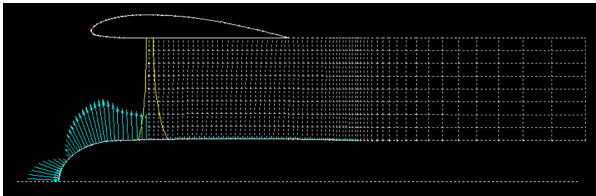


Figure B.98: Pressure vectors around the centerbody, $AR_{duct} = 1.45$

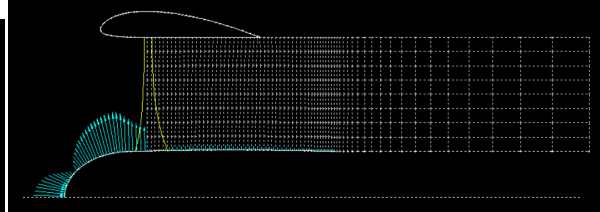


Figure B.99: Pressure vectors around the centerbody, $AR_{duct} = 2$

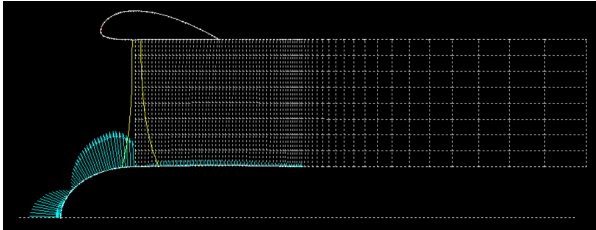


Figure B.100: Pressure vectors around the centerbody, $AR_{duct} = 3$

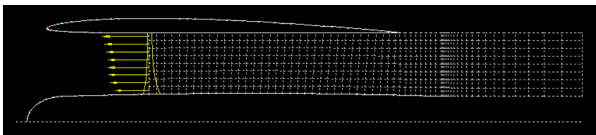


Figure B.101: Pressure vectors of the propeller, $AR_{duct} = 0.5$

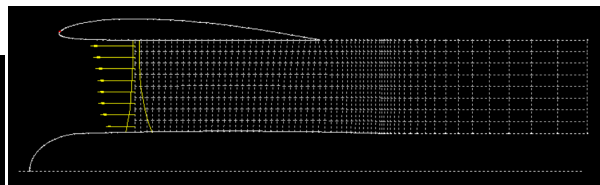


Figure B.102: Pressure vectors of the propeller, $AR_{duct} = 1$

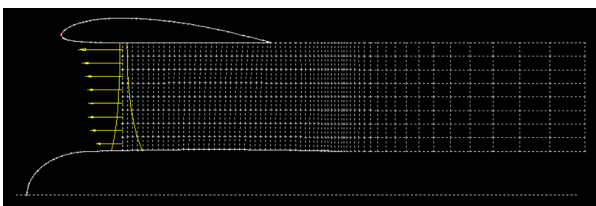


Figure B.103: Pressure vectors of the propeller, $AR_{duct} = 1.45$

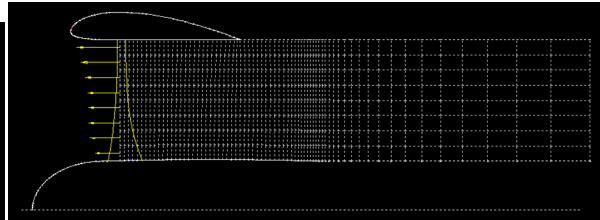


Figure B.104: Pressure vectors of the propeller, $AR_{duct} = 2$

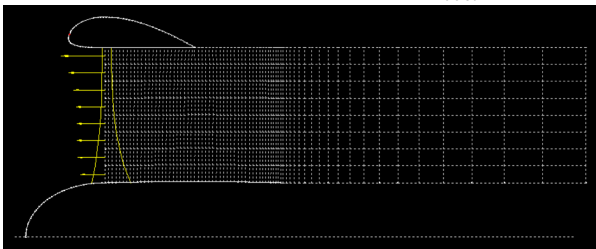


Figure B.105: Pressure vectors of the propeller, $AR_{duct} = 3$

B.5. CAMBER

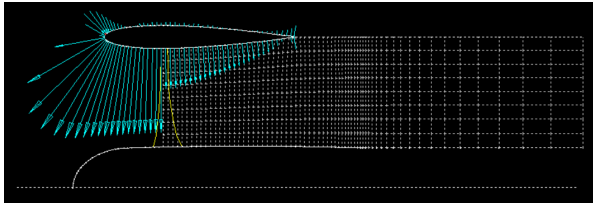


Figure B.106: Pressure vectors around the duct for NACA0012

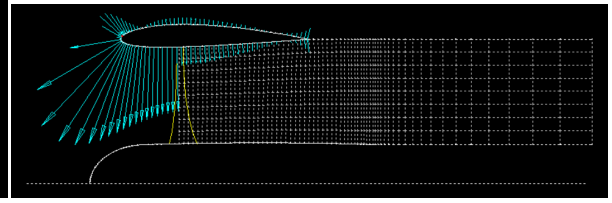


Figure B.107: Pressure vectors around the duct for NACA2412

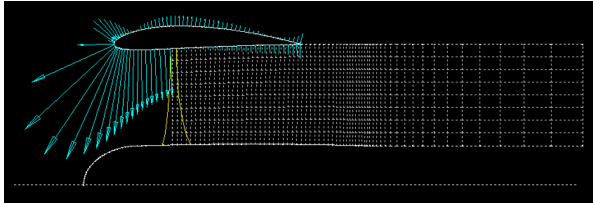


Figure B.108: Pressure vectors around the duct for NACA4412

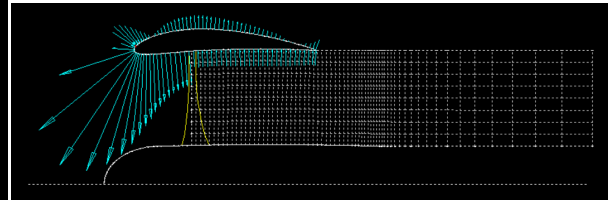


Figure B.109: Pressure vectors around the duct for NACA6412

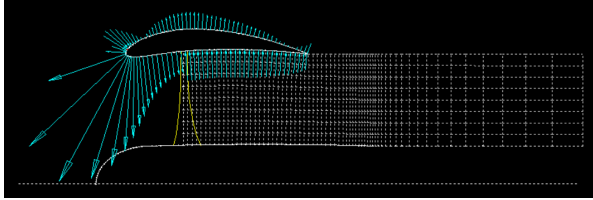


Figure B.110: Pressure vectors around the duct for NACA6412

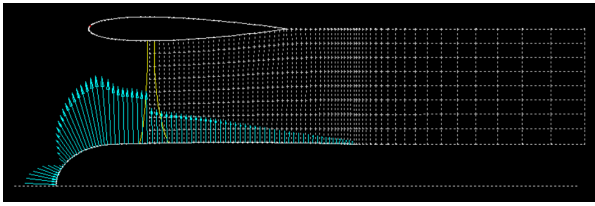


Figure B.111: Pressure vectors around the centerbody for NACA0012

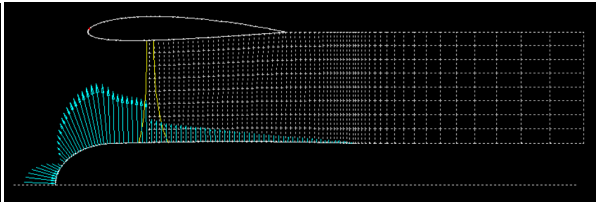


Figure B.112: Pressure vectors around the centerbody for NACA2412

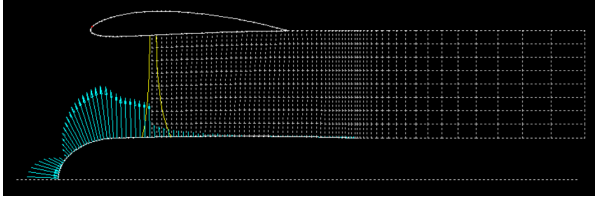


Figure B.113: Pressure vectors around the centerbody for NACA4412

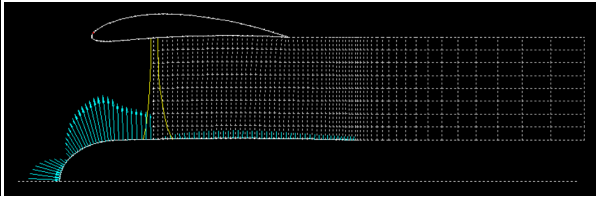


Figure B.114: Pressure vectors around the centerbody for NACA6412

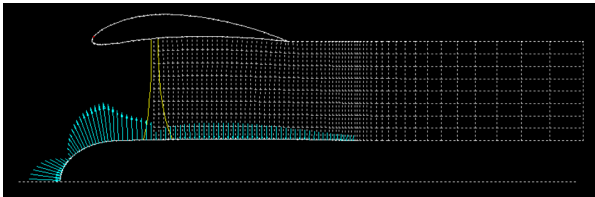


Figure B.115: Pressure vectors around the centerbody for NACA8412

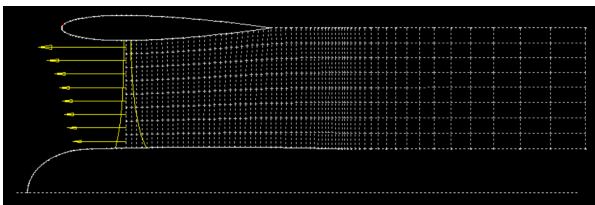


Figure B.116: Pressure vectors of the propeller for NACA0012

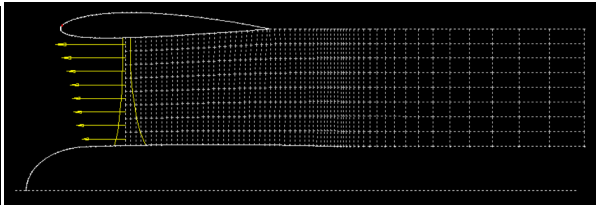


Figure B.117: Pressure vectors of the propeller for NACA2412

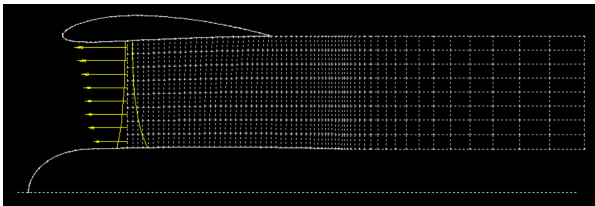


Figure B.118: Pressure vectors of the propeller for NACA4412

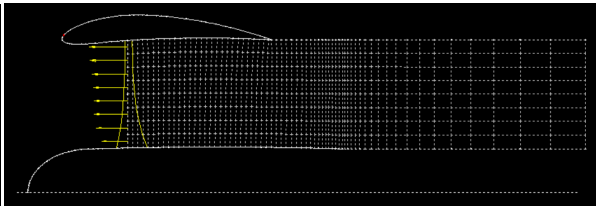


Figure B.119: Pressure vectors of the propeller for NACA6412

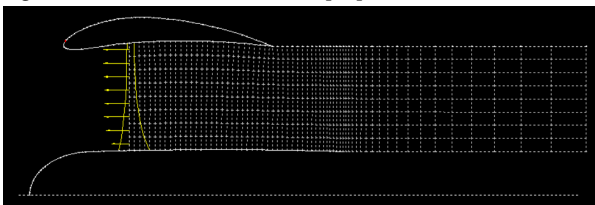


Figure B.120: Pressure vectors of the propeller for NACA8412

B.6. THICKNESS TO CHORD RATIO

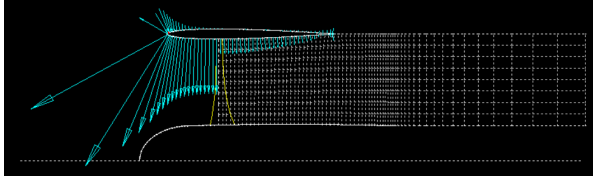


Figure B.121: Pressure vectors around the duct for NACA006

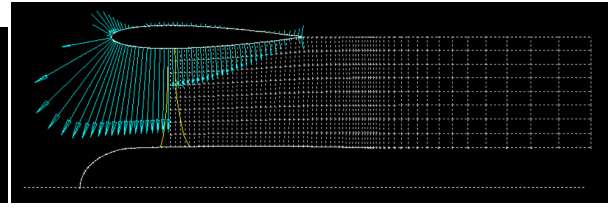


Figure B.122: Pressure vectors around the duct for NACA0012

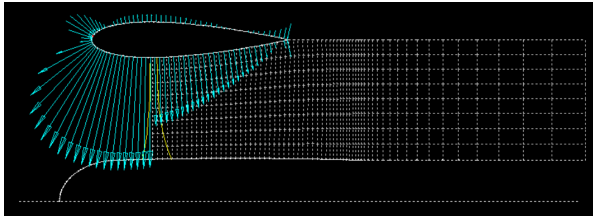


Figure B.123: Pressure vectors around the duct for NACA0018

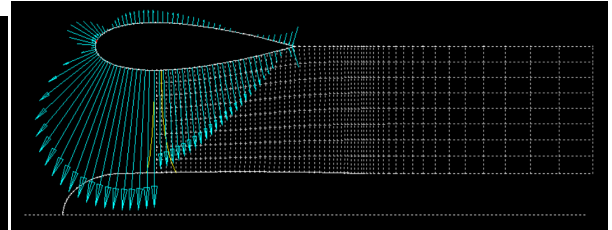


Figure B.124: Pressure vectors around the duct for NACA0024

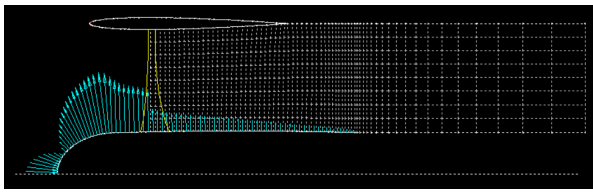


Figure B.125: Pressure vectors around the centerbody for NACA006

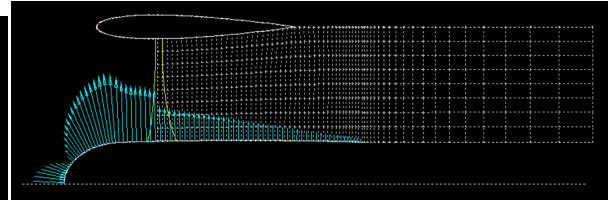


Figure B.126: Pressure vectors around the centerbody for NACA0012

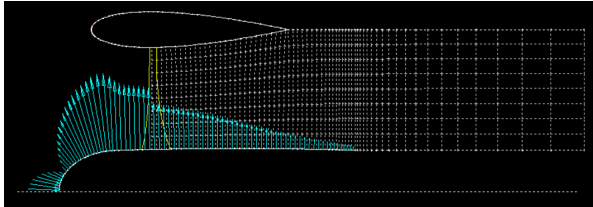


Figure B.127: Pressure vectors around the centerbody for NACA0018

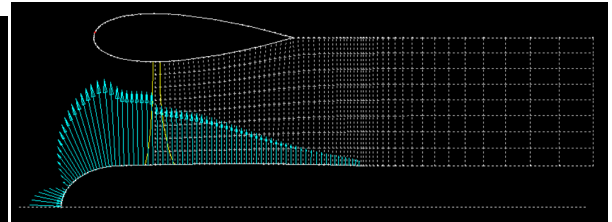


Figure B.128: Pressure vectors around the centerbody for NACA0024

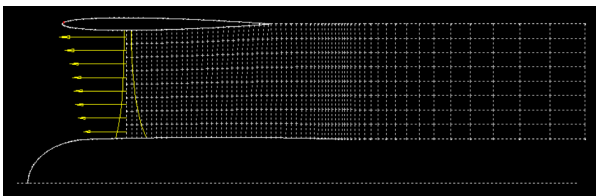


Figure B.129: Pressure vectors of the propeller for NACA006

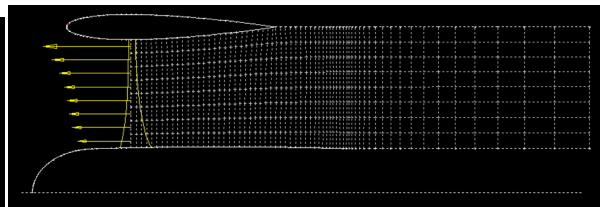


Figure B.130: Pressure vectors of the propeller for NACA0012

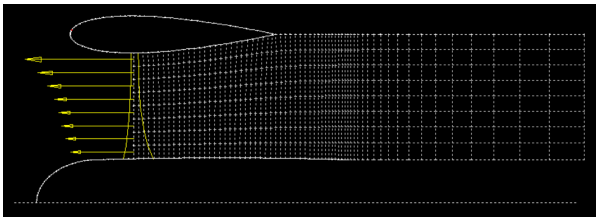


Figure B.131: Pressure vectors of the propeller for NACA0018

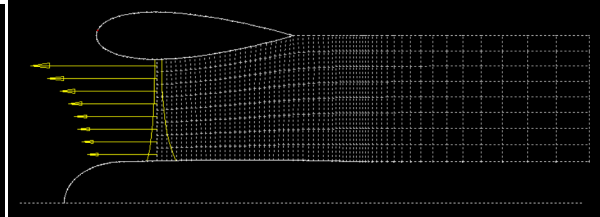


Figure B.132: Pressure vectors of the propeller for NACA0024

BIBLIOGRAPHY

- [1] K. W. Morth and B. Gamse, *A Wind Tunnel Investigation of a 7 Foot Diameter Ducted Propeller*, Journal of Aircraft (1967).
- [2] K. J. Grunwald and K. W. Goodson, *Aerodynamic Loads on an Isolated Shrouded-Propeller Configuration for Angles of Attack from -10° to 110°* , Tech. Rep. (Langley Research Center, 1962).
- [3] A. Kriebel, *Theoretical Stability Derivatives for a Ducted Propeller*, Journal of Aircraft **1**, 203 (1964).
- [4] D. M. Black and H. Wainauski, *Shrouded Propellers - a Comprehensive Performance Study*, AIAA **68-994** (1968).
- [5] S. Yilmaz and D. Erdem, *Effects of Duct Shape on a Ducted Propeller Performance*, AIAA (2013).
- [6] J. Ahn and K. Lee, *Performance Prediction and Design of a Ducted Fan System*, AIAA (2004).
- [7] A. Abrego and R. Bulaga, *Performance Study of a Ducted Fan System*, Proceedings of AHS Aeromechanics Specialists Mtg. (2002).
- [8] K. R. K. N. P. Bi and D. Haas, *Performance Investigation of Ducted Aerodynamic Propulsors*, First International Symposium on Marine Propulsors (2009).
- [9] M. Anderson, K. Lehmkuehler, D. Ho, K. Wong, and P. Hendrick, *Propeller Location Optimisation for Annular Wing Design*, Tech. Rep. (University of Sidney and Universite Libre de Bruxelles, 2013).
- [10] J. F. W. Graf and W. Ng, *Improving ducted fan UAV aerodynamics in forward flight*, AIAA (2008).
- [11] K. N. H. Otsuka and K. Yoshida, *Evaluation of hovering thrust performance of shrouded rotors for multi-rotor UAVs to reduce weight*, Tech. Rep. (Tohoku University, 2015).
- [12] M. M. R. Bontempo, M. Cardone and G. Vorraro, *Ducted propeller flow analysis by means of a generalized actuator disk model*, Elsevier (2013).
- [13] G. T. S Gaggero, C M Rizzo and M. Viviani, *Efd and Cfd Design and Analysis of a Propeller in Decelerating Duct*, International Journal of Rotating Machinery (2012).
- [14] F. M. de Piolenc and G. E. W. Jr., *Ducted Fan Design*, 2nd ed. (Mass Flow, 2001).
- [15] H. S. Fletcher, *Experimental Investigation of Lift, Drag, and Pitching Moment of Five Annular Airfoils*, Tech. Rep. (National Advisory Committee for Aeronautics, Langly Field, Va., 1957).
- [16] H. S. Ribner, *The Ring Airfoil in Nonaxial Flow*, Journal of the Aeronautical Sciences (1947).
- [17] J. Weissinger, *On the aerodynamics of ring wings, 1. The pressure distribution on a thin, almost axially symmetric wing in subsonic flow*, Tech. Rep. (David Taylor Model Basin, 1957).
- [18] L. W. Traub, *Experimental Investigation of Annular Wing Aerodynamics*, Journal of Aircraft (2009).
- [19] A. Maqsood and T. H. Go, *Aerodynamic Estimation of Annular Wings Based on Leading-Edge Suction Analogy*, AIAA Journal (2013).
- [20] M. L. Mason and B. L. Berrier, *Static performance of nonaxisymmetric nozzles with yaw thrust-vectoring vanes*, Tech. Rep. (Langley Research Center, 1988).
- [21] P. G. I. Guerrero, K. Londenber and A. Myklebust, *A powered lift aerodynamic analysis for the design of ducted fan UAVs*, AIAA Journal (2003).

-
- [22] H. Sung and Y. Hwang, *Thrust-vector characteristics of jet vanes arranged in x-formation within a shroud*, AIAA Journal (2003).
- [23] W. F. Durand, *Aerodynamic Theory*, 1st ed. (Springer-Verlag Berlin Heidelberg, 1935).
- [24] J. de Young, *Propeller at High Incidence*, Journal of Aircraft (1965).
- [25] M. H. Sadraey, *Aircraft Design: A Systems Engineering Approach*, 1st ed. (Wiley, 2012).
- [26] R. Roskam, *Airplane flight dynamics and automatic flight controls*, 1st ed. (Roskam Aviation and Engineering Corporation, 1979).
- [27] S. F. Hoerner, *Fluid Dynamic Drag*, 1st ed. (Hoerner, 1965).
- [28] A. K. Geim and H. A. M. S. ter Tisha, *Detection of earth rotation with a diamagnetically levitating gyroscope*, [Physica B: Condensed Matter](#) **294–295**, 736 (2001).